POLITECNICO DI MILANO
DEPARTMENT OF ENERGY
DOCTORAL PROGRAM IN ENERGY AND NUCLEAR SCIENCE AND TECHNOLOGY

AN INNOVATIVE MULTIPHYSICS MODELLING APPROACH FOR THE ANALYSIS AND THE DEVELOPMENT OF THE GENERATION IV MOLTEN SALT FAST REACTOR

Doctoral Dissertation of:
Eric Cervi

Supervisors:
Prof. Antonio Cammi
Prof. Lelio Luzzi

Tutor:
Prof. Lelio Luzzi

The Chair of the Doctoral Program:
Prof. Vincenzo Dossena

XXXII Cycle

July 2020 – Milano, Italy

Acknowledgements

The thesis has been carried out in the framework of a collaboration among Politecnico di Milano, Politecnico di Torino, the Laboratoire de Physique Subatomique et de Cosmologie (LPSC) CNRS-Grenoble (France), the Paul Scherrer Institute (Switzerland), the Technische Universiteit Delft (Netherlands), the Karlsruhe Institute of Technology (Germany) and other institutions participating to the Euratom H2020 Samofar Project.

Summary

MOLTEN Salt Reactors (MSRs) are one of the six next-generation nuclear reactor concepts identified for further research and development in the frame of the Generation IV International Forum. The most distinguishing characteristic of MSRs is the presence of a molten salt mixture acting simultaneously as fuel and as coolant. This feature may lead to significant improvements in the reactor safety and sustainability and to a strong plant simplification. At the same time, the liquid fuel raises important challenges in the analysis, development and operation of MSRs, requiring the development of new simulation tools tailored to the peculiarities of these innovative systems. In this context, the purpose of this thesis is to improve the multiphysics modelling of MSRs, addressing specific issues that cannot be investigated neither with computational tools developed for solid-fuelled reactors nor with state-of-the-art models developed for molten salt systems. The Molten Salt Fast Reactor (MSFR), developed in the frame of the EVOL (Brovchenko et al., 2013), H2020 SAMOFAR (http://samofar.eu/) and SAMOSAFER (https://samosafer.eu/) Projects, is adopted as the reference system for the developments and analyses carried out in this work.

In the first part of the thesis, a new multiphysics model for the MSFR is developed and implemented into an OpenFOAM solver. This solver features a two-phase, compressible thermal-hydraulics model, able to handle the presence of gas bubbles inside the reactor and to take into account the fuel mixture compressibility. The fluid-dynamics model is coupled with a multi-group neutron diffusion model, a multi-group SP_3 neutron transport model and with transport equations for the delayed neutron and decay heat precursors, which are dragged by the liquid fuel (unlike in traditional solid-fuelled reactors, in which they are fixed).

The second part of the thesis is devoted to the analysis of the MSFR helium bubbling system (i.e., the injection of helium bubbles into the fuel mixture), envisaged for a more efficient removal of gaseous fission products and as a possible option for reactivity control, exploiting the negative reactivity feedback of the bubbles. The impact of the helium bubbles on the system reactivity is investigated, accounting for the non-uniform bubble distribution inside the reactor and highlighting the differences with single-phase, state-of-the-art approaches that can only model the void fraction as a uniform density effect.

Finally, the third part of the thesis investigates the impact of the fuel mixture compressibility on the system dynamics. Indeed, compressibility is expected to introduce delays in the thermal expansion reactivity feedbacks, especially in fast, super-prompt-critical transients, in which the characteristic times of neutronics and of pressure/density wave propagation are comparable. Moreover, the fuel compressibility is modified - both locally and globally - by the presence of bubbles in the reactor. Consequently, the analysis cannot leave the modelling of the helium bubbling system out of consideration, due to the complex interplay between compressibility and the bubbly flow.

The present work constitutes a substantial step forward, as compared to state-of-the-art models developed for MSRs, allowing to describe phenomena that cannot be investigated with standard approaches. In the light of this, the results of the thesis can represent an important starting point to assess the safety and the feasibility of the MSFR in a more accurate way, as well as to optimize its main design features, such as the reactivity control systems, the fuel composition and the operating temperatures.

Contents

Nomenclature

NOMENCLATURE[1]

Latin symbols

A	Cross section temperature coefficient, m
C_p	Constant pressure specific heat, W/kg K
c	Delayed neutron precursor density, kg^{-1}
D	Neutron diffusion coefficient, m
d	Decay heat precursor density, W kg^{-1}
d_0	Reference bubble diameter, m
d_b	Bubble diameter, m
E_f	Fission energy, J
Eo	Eötvös number, -
$\boldsymbol{g}$	Gravitational acceleration, m s^{-2}
h	Specific enthalpy, J kg^{-1}
K	Modified thermal diffusivity, J m^{-1} s^{-1} K^{-1}
k	Specific kinetic energy, J kg^{-1}
k_{eff}	Effective multiplication factor, –
K_D	Doppler constant, pcm
K_{fuel}	Pure salt bulk modulus, Pa
L	Inter-phase heat transfer coefficient, W m^{-3} K
M	Inter-phase momentum transfer, kg m^{-2} s^{-2}
Ma	Mach number, -
p	Pressure, Pa
p_0	Reference pressure, Pa
pcm	per cent mille (=10^{5})
Pr	Prandtl number, -
Q	Power source density, W m^{-3}
R	Gas constant, J mol^{-1} K^{-1}
Re	Reynolds number, -
S	Mass source, kg m^{-3} s^{-1}
Sc	Schmidt number, -
T	Temperature, K
t	Time, s

[1] Appendix A has a dedicated nomenclature table.

$\boldsymbol{u}$	Velocity, m s^{-1}
$\boldsymbol{u}_r$	Relative velocity, m s^{-1}
V	Volume, m^3
v	Neutron velocity, m s^{-1}
We	Weber number, -
We_{cr}	Critical Weber number, -

Greek symbols

α	Phase fraction, -
$\bar{\alpha}_b$	Core-average void fraction, -
α_i	Albedo coefficient for the *i*-th neutron energy group, -
α_{void}	Void coefficient, pcm/%
β	Delayed neutron precursor fraction, –
β_{heat}	Decay heat energy fraction, –
β_{th}	Thermal expansion coefficient, kg m^{-3} K^{-1}
ΔT	Inter-phase temperature difference, K
κ	Thermal conductivity, J s^{-1} m^{-1} K^{-1}
λ	Delayed neutron precursor decay constant, s^{-1}
λ_h	Decay heat precursor decay constant, s^{-1}
μ	Dynamic viscosity, Pa s
ν	Kinematic viscosity, m^2 s^{-1}
$\bar{\nu}$	Mean neutrons per fission, –
ρ	Density, kg m^{-3}
$\tilde{\rho}$	Reactivity, pcm
$\sum$	Macroscopic cross section, m^{-2}
Φ	Neutron flux as defined by Eq. (2.24), m^{-2} s^{-1}
φ	Neutron flux (diffusion equation), m^{-2} s^{-1}
φ_o	Neutron flux (SP_3 equation), m^{-2} s^{-1}
φ_2	Neutron flux second moment (SP_3 equation), m^{-2} s^{-1}
χ	Neutron yield, –
ψ	Isothermal compressibility coefficient, m^{-2} s^{-2}

Subscripts-superscripts

b	Bubble
d	Delayed
f	Fission
g	Gas
h	Decay heat
i	Neutron energy group
j	Phase
k	Delayed neutron precursor group
l	Liquid
m	Decay heat precursor group
p	Prompt
r	Removal
s	Scattering
$s2$	Second order inelastic scattering
$s3$	Third order inelastic scattering
T	Turbulent
t	Total
tr	Transport

List of acronyms

CFD	Computational Fluid Dynamics
FVM	Finite Volume Method
GFR	Gas Fast Reactor
LFR	Lead Fast Reactor
LMFR	Liquid Metal Fast Reactor
LWR	Light Water Reactor
MSBR	Molten Salt Breeder Reactor
MSFR	Molten Salt Fast Reactor
MSR	Molten Salt Reactor
MSRE	Molten Salt Reactor Experiment
ORNL	Oak Ridge National Laboratory
POLIMI	Politecnico di Milano
SCWR	Supercritical Water Reactor
SFR	Sodium Fast Reactor
TRU	Transuranic element
TUDelft	Technische Universiteit Delft
VHTR	Very High Temperature Reactor
VOF	Volume of Fluid

Chapter 1

Introduction

MOLTEN Salt Reactors (MSRs) are circulating-fuel nuclear systems in which a mixture of thorium, uranium (and eventually transuranic elements) salts acts simultaneously as fuel and as coolant. The fuel mixture transfers the heat produced by fission to external heat exchangers via convection.

MSRs were firstly conceived in the Fifties for military purposes in the United States and subsequently, for two decades, developed as graphite-moderated ^{232}Th-^{233}U reactors for power production. Back then, studies on MSR technology were mostly carried out at Oak Ridge National Laboratory (ORNL), where the research efforts for energy production culminated in the operation of the Molten Salt Reactor Experiment (MSRE, Figure 1.1), which achieved criticality in 1965, and in the design of the Molten Salt Breeder Reactor (MSBR) (MacPherson, 1985). Despite the positive experience, the interest in MSRs started to fade during the Seventies in favour of Liquid Metal Fast Reactors (LMFR), considered a more promising option for breeding purposes. Consequently, the MSBR was never built and the MSRE remained the last molten salt reactor ever operated.

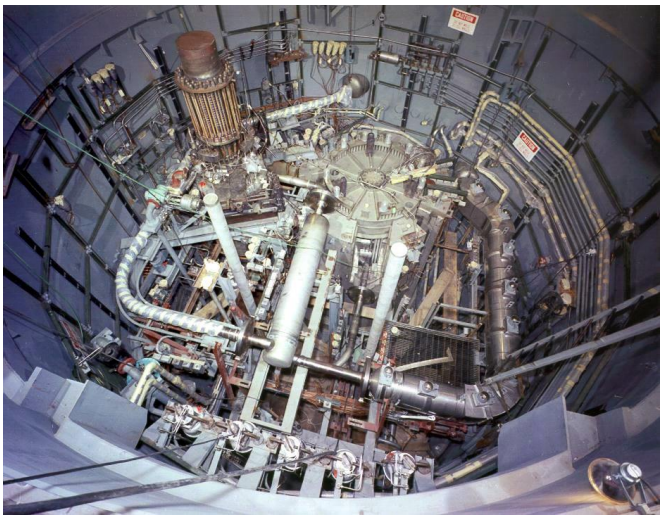

Figure 1.1. Molten Salt Reactor Experiment (Oak Ridge National Laboratory, USA).

Nevertheless, in the last few years, MSR technology is gathering renovated interest in the nuclear reactor community, due to the following features:

- High power density, since fission energy is directly released into the coolant;
- Intrinsic safety characteristics, such as the possibility of operation at atmospheric pressure, due to the high boiling point of the fuel mixture;
- Intrinsic sustainability, as the adoption of a closed thorium fuel cycle leads to an actinide inventory with lower radiotoxicity;
- Significant plant simplification allowed by the adoption of a liquid fuel.

Research efforts are focusing both on thermal and fast spectrum systems and on the development of breeder, converter and incinerator reactors. In this frame, the MSR concept has been identified by the Generation IV International Forum (Serp et al., 2014; Pioro, 2016; GIF, 2017; Dolan, 2017) as a promising option for a sustainable, safe and proliferation-resistant power production.

1.1 The Molten Salt Fast Reactor

The Molten Salt Fast Reactor (MSFR) (Gerardin et al., 2017; Tano et al., 2017) has been selected as the reference molten salt reactor in the GIF-IV framework (GIF, 2017). The MSFR has been studied since 2004 at the Centre Nationale de la Recherche Scientifique (CNRS, Grenoble, France) and it has mainly been developed in the frame of the Euratom Projects EVOL (Brovchenko et al., 2013), SAMOFAR (http://samofar.eu/) and, starting from 2019, SAMOSAFER ((https://samosafer.eu/) (Allibert et al., 2016a; 2016b; Lorenzi et al., 2016).

Differently from the MSRE and the MSBR, the MSFR is characterized by an intermediate-to-fast neutron spectrum and by the absence of in-core moderator and structural materials. It is designed to operate at a nominal power of 3 GW_{th}, at an average in-core temperature of 700°C and at atmospheric pressure, thanks to the high boiling point of the liquid fuel. The selected salt consists in a mixture of ^{7}LiF and $^{232}ThF_4$ at eutectic composition (77.5 – 22.5 mol%), with other fissile fluorides substituting a fraction of ThF_4. In this regard, two compositions are presently under investigation, one containing only ^{233}U as fissile, and the other including enriched $^{235}U/^{238}U$ and transuranics (TRUs). The ^{233}U enriched composition is adopted as reference in this thesis, even if the analyses carried out in this work can be easily extended to other fuel compositions. The main design features of the MSFR are listed in Table 1.1. The reactor features an online chemical reprocessing system to remove fission products from the fuel (see Figure 1.2). Chemical processing consists in removing about 40 liters of fuel every day for a special reprocessing involving several steps, based on the redox and acido-basic properties of the elements in the salt (Allibert et al., 2016a).

The original shape was conceived as a cylinder with height equal to the diameter, from considerations of neutron economy optimization. However, Computational Fluid-

Dynamics (CFD) analyses pointed out that the cylindrical configuration led to significant recirculation and, consequently, to fuel temperatures above 1000°C near the radial wall. To address this issue, a toroidal, recirculation-free shape was subsequently adopted as the reference geometry. The fuel is extracted from the top of the reactor, circulated across sixteen external heat exchangers in order to remove the power produced by fission, and finally pumped back to the bottom of the reactor. A schematic layout of the system is shown in Figure 1.2.

Table 1.1. The main design features of the MSFR.

Nominal Power	3000 MW_{th}
Inlet / average / outlet temperatures	650°C / 700°C / 750°C
Total primary volume	18 m^3 (50% in-core, 50% out-of-core)
Nominal flow rate	4.5 m^3/s
Fuel composition 1: ^{232}Th - ^{233}U (adopted in the thesis)	
LiF	77.5 mol%
ThF_4	20.0 mol%
$^{233}UF_4$	2.5 mol%
Fuel composition 2: ^{232}Th - ^{235}U - ^{238}U – TRU	
LiF	77.5 mol%
ThF_4	6.6 mol%
$^{235}UF_4$ / $^{238}UF_4$	12.3 mol % (13% ^{235}U enrichment)
PuF_3	3.15 mol%
NpF_3	0.23 mol%
AmF_3	0.19 mol%
CmF_3	0.03 mol%

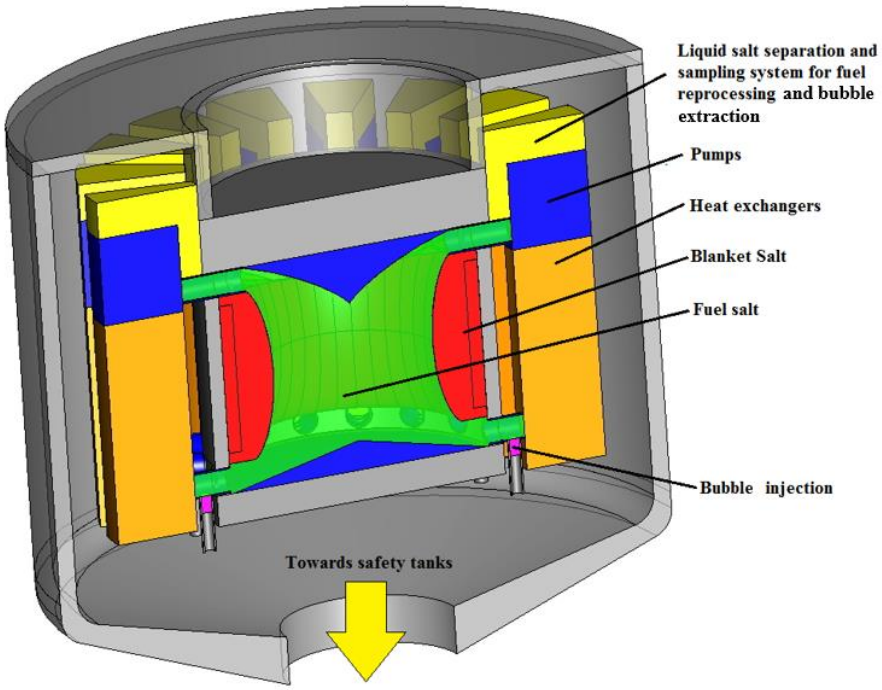

Figure 1.2. Schematic layout of the MSFR (Allibert et al., 2016).

Since the delayed neutron precursors are dragged by the fuel outside of the reactor, concerns are raised for two main reasons:

1. The in-core delayed neutron fraction is lower, as compared to a static fuel system with the same fuel composition. Consequently, chances that a super-prompt-critical reactivity injection occurs increase.

2. In case of loss of flow accidental scenarios, the precursor redistribution (i.e., the increase of the in-core precursor density) leads to a positive reactivity insertion.

To address these issues, studies has been conducted (Laureau, 2015) pointing out that the reactor behaves safely if at least half of the delayed neutrons are produced inside the core. For this reason, the fraction of fuel salt in the core is approximately 50%. This design choice also improves general safety (e.g., in case of a fuel leakage from a heat exchanger circuit) and is based on economic considerations as well (Laureau, 2015).

Nickel-based alloy reflectors are placed on top and at the bottom of the reactor to limit neutron leakages and improve neutron economy. Considering that the fuel temperature near the extraction area is around 750°C, the upper reflector is subject to strong thermal stress which, together with high radiation levels, constitutes the main challenge for the envisaged alloy. On the other hand, the lower reflector is under lower thermal stress and has the specificity of being coupled with the draining systems (Allibert et al., 2016a).

Radially, the core is surrounded by a fertile blanket composed of LiF-ThF_4 in order to improve the breeding capabilities of the reactor. The blanket walls are made of a corrosion-resistant nickel-based alloy and are layered with B_4C on the outer wall to further improve neutron shielding (Allibert et al., 2016a).

The draining systems are placed below the active core and two draining modes are foreseen (Fig 1.3):

1. *Emergency draining:* in case of anomalous scenarios during operation, the fuel salt can be drained to a criticality-safe tank, either by active or passive devices. This draining must be rapid to limit the fuel salt heating in case of a loss of cooling accident;

2. *Controlled routine draining:* the fuel salt is transferred to actively cooled storage tanks in view of short-duration maintenance procedures. In case of accidental scenarios, the storage tanks can be emptied into the emergency tank. These tanks also have the function of heating the salt before core filling.

Another important feature, that will be object of the present thesis, is that a helium bubbling system (i.e., the injection of helium bubbles into the fuel mixture) is foreseen for two reasons:

1. To remove the gaseous fission products via dilution in the carrying gas;

2. To remove the solid precipitates dragged by the fuel salt, via capillarity sticking to the bubbles.

In addition, this option is being considered for reactivity control purposes, exploiting the negative void feedback of the bubbles, in replacements of the traditional control rods. As shown in Figure 1.2, the helium bubbles are injected at the bottom and removed at the top of the reactor.

For more detailed information on the MSFR design, the reader is referred to (Allibert et al., 2016a; Lorenzi et al., 2016; Gerardin et al., 2017; Tano et al., 2017).

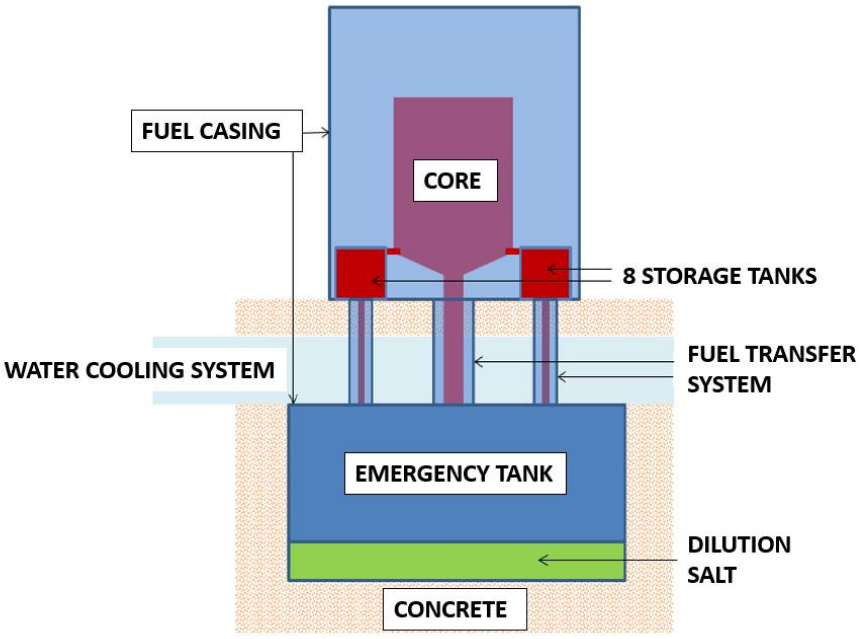

Figure 1.3. MSFR draining systems (Allibert et al., 2016).

The MSFR and liquid-fuelled systems in general benefit from different potential advantages, as compared to other Generation IV reactors (Fiorina, 2013; Allibert et al., 2016b), namely: the Sodium Fast Reactor (SFR), the Lead Fast Reactor (LFR), the Gas Fast Reactor (GFR), the Very High Temperature Reactor (VHTR) and the Supercritical Water Reactor (SCWR), all of which are solid-fuelled systems (GIF, 2017). In more details, thanks to the online reprocessing, remote fabrication of solid fuel with large amount of thorium or TRUs under thick shielding, as well as handling and transportation, can be avoided. In fact, due to the continuous adjustment of the fuel composition, a large initial reactivity inventory is not required (which is also an advantage in terms of safety). This is one of the most promising features of the MSFR, making it a competitive candidate for operation with thorium or TRU based fuels. In addition, online reprocessing allows for better resource utilization by achieving higher burnups, as TRUs remain in the fuel undergoing fission or transmutation into a fissile element. In addition, the heat production into the fuel (which is also the coolant) avoids heat transfer delays and the fuel homogeneity does not require loading plans, constituting further advantages as compared to solid-fuelled Generation IV and LWR systems. Finally, due to the presence of thorium and to the relatively softer neutron spectrum, the Doppler coefficient is expected to be higher than traditional SFRs and LFRs (Fiorina, 2013), improving reactor safety and stability in case of strong power excursions.

1.2 Objectives, motivation and outline of the thesis

The purpose of this thesis is the improvement of the multiphysics modelling of the MSFR, to increase the accuracy and the level of detail as compared to current simulation tools. This research work is motivated by the strong interest of nuclear reactor communities in the analysis and the development of innovative systems, such as the liquid-fuelled MSFR, due to the aforementioned safety and sustainability characteristics. However, the peculiarities of liquid-fuelled reactors and the lack of knowledge of their dynamics require the development of new simulation tools, tailored to the specificities of these innovative systems. In particular, as compared to traditional solid-fuelled reactors, the MSFR has some specific issues:

1. The coupling between neutronics and thermal-hydraulics is stronger, as compared to conventional systems. Partly, this is due to the fact that fission energy is directly released into the coolant (while in solid-fuelled reactors fission power is generated in the fuel pins and then removed by the coolant). Another reason is that the delayed neutron precursors are dragged by the molten salts, unlike in conventional systems in which precursors are fixed. Consequently, the precursor distribution is directly influenced by the velocity field of the fuel. Therefore, new simulation tools, suitable to solve the coupling non-linearities arising in the MSFR, are needed;

2. A helium bubbling system is foreseen in the MSFR for a more efficient removal of the gaseous fission products. This system is also envisaged as a possible option for reactivity control, exploiting the void reactivity feedback of the bubbles (Figure 1.4). In this case, helium bubbling would replace the control rods, traditionally employed for reactivity control of conventional solid-fuelled

reactors. Up to now, no detailed analysis of the helium bubbling system is available in literature. Again, this leads to the necessity to develop new computational tools, able to simulate this new design option;

3. In addition, the liquid fuel compressibility may have an important impact on the system dynamics, introducing delays in the thermal expansion reactivity feedbacks. These effects are expected to be particularly important in very rapid, super-prompt-critical transients, whose characteristic times are comparable to the propagation times of pressure/density waves through the reactor (Aufiero et al., 2017). Furthermore, the presence of bubbles inside the fuel mixture modifies the fuel compressibility both globally and locally, potentially leading to further effects that cannot be studied by means of standard approaches. For this reason, the problems of compressibility and of the helium bubbling systems are strongly related and cannot be studied independently.

Most of the simulation tools currently adopted in the nuclear community are not suitable to the analysis of these problems, as they were developed to satisfy the specific needs of second and third generation Light Water Reactors (LWRs). Often, the large operational and modelling experience on LWRs opened the way to the development and justification of many strong assumptions that have been adopted in the computational codes. In addition, most of the models specifically developed in the Sixties for molten salt reactors were tailored to the features of thermal systems such as the MSRE (Bauman et al., 1971; Krepel et al., 2007). From them on, the development of new methods and techniques was mainly limited by their expensive computational requirements.

Today, most of these computational constraints have been overcome, paving the way to the development of new and innovative modelling approaches, such as the direct coupling between neutron transport or diffusion and CFD. Coupled neutronics and thermal-hydraulics models for the analysis of the MSFR were successfully developed, among the others, by Aufiero et al. (2014a; 2014b) and Fiorina et al. (2014). Despite constituting a huge step forward in the analysis of non-moderated molten salt reactors, these models are still limited by some simplifying assumptions:

1. On one hand, they adopt single-phase fluid-dynamics solvers. Consequently, they are not capable of handling the presence of bubbles inside the reactor;

2. On the other hand, treating the molten salts as an incompressible liquid, they cannot take into account the fuel compressibility impact on reactor dynamics.

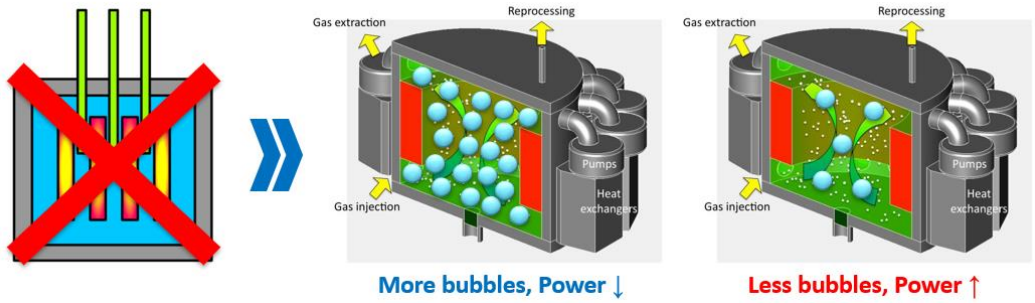

Figure 1.4. The MSFR helium bubbling system (http://samofar.eu/concept/).

Consequently, the problems of the helium bubbling system and of fuel compressibility effects, that are fundamental to understand the MSFR dynamics, have never been studied in detail and still represent an open research field. The aim of the thesis is to shed the light on these problems. To this purpose, innovative modelling approaches are developed, to overcome the limitations of current simulation tools for the MSFR. This is an extremely challenging task, as different physics come into play (namely, neutronics, two-phase thermal-hydraulics, precursor dragging by the liquid fuel, and pressure wave propagation as well). This requires the development of different models, tailored to the specificities of each physics both from a theoretical and numerical point of view. Moreover, a coupling strategy is needed to describe the interplay among these physics.

The remainder of this thesis is organized as follows. In Chapter 2, details on state-of-the-art solvers for the MSFR are provided and a new model is developed, coupling neutronics, two-phase, compressible fluid dynamics and transport equation for the moving precursors. Thanks to these features, the proposed model is suitable to the analysis of the helium bubbling system and to investigate the fuel compressibility impact on the system dynamics. This model is implemented using OpenFOAM (OpenFOAM, 2013), a CFD and multiphysics toolkit based on the finite volume method (FVM) for the spatial discretization of partial differential equations.

Then, in Chapters 3 and 4, the new multiphysics model is applied to the analysis of the helium bubbling system and of its impact on reactivity. Firstly, the problem is studied on a simplified 2D geometry, and a sensitivity analysis is carried out to assess the assumptions and the correlations adopted in the two-phase thermal-hydraulics model. Subsequently, the analysis is extended to the 3D, reference toroidal geometry of the MSFR, comparing different neutronics approaches (multi-group neutron diffusion, multi-group SP_3 neutron transport, and continuous energy Monte Carlo).

Chapter 5 is devoted to the analysis of fuel compressibility effects on the system dynamics. This problem is firstly investigated without considering the helium bubbling system, in order to point out the role of the pure liquid salt compressibility. Subsequently, the presence of bubbles inside the reactor is taken into account, highlighting the additional effect that they have on compressibility and on the system dynamics in turn.

In addition, Appendix A briefly reports a preliminary investigation on the development of a discrete-ordinate neutron transport model, while Appendix B presents the main models and closure relations adopted in the proposed two-phase thermal-hydraulics solver. Finally, Appendix C provides information on delayed neutron and decay heat precursor properties.

1.3 The OpenFOAM library

The Open-source Field Operation And Manipulation (OpenFOAM, Weller et al., 1998; Jasak et al., 2007) is a C++ library based on the finite volume method (FVM) (Moukalled et al., 2016) for the spatial discretization and solution of partial differential equations, employing user-selected discretization and interpolation schemes. Upwind, linear and high-resolution schemes (Moukalled et al., 2016) are available to flux physical quantities between different mesh cells, making this tool extremely versatile

for a wide range of parabolic and hyperbolic problems. Krilov-type and multigrid solvers (Moukalled et al., 2016) can be used for the solution of the linear systems resulting from the spatial discretization of the governing equations.

OpenFOAM has been extensively used for CFD simulations, solving complex fluid flows involving turbulence, chemical reactions, and heat transfer. However, thanks to the flexibility of object-oriented programming, as well as to the open-source nature of the OpenFOAM code, this toolkit is ideal for modelling and solving any complex continuum-mechanics problem, from neutron diffusion, to deterministic neutron transport and to thermal-mechanics. Consequently, it is particularly suitable for multiphysics applications and for the analysis of strongly coupled systems such as nuclear reactors. In OpenFOAM solvers, the governing equations are solved in a segregated fashion (i.e., once at a time) and Picard iterations are performed to achieve the implicit convergence of the coupled solution.

Another interesting feature of the OpenFOAM toolkit is the high-level C++ representation of operators, thanks to which the implementation of continuum-mechanics equations closely matches their mathematical form. For example, the single-velocity neutron diffusion equation can be implemented as follows:

```
solve
(
    fvm::ddt(1.0/v, phi)
   ==
    fvm::laplacian(D,phi)
  + fvm::Sp(nu_sigma_fission, phi)
  - fvm::Sp(sigma_absorption, phi)
);
```

in analogy with its “pen-and-paper” formulation:

$$\frac{1}{v}\frac{d\varphi}{dt} = \nabla \cdot (D\nabla\varphi) + \nu\Sigma_f - \Sigma_a \tag{1.1}$$

1.4 Conclusive remarks

The MSFR offers interesting characteristics of safety and sustainability and has a strong potential for plant simplification. At the same time, the presence of a liquid fuel mixture leads to specific issues that cannot be studied with simulation codes developed for solid-fuelled reactors, requiring the development of new and more advanced computational tools. In the present thesis, a particular focus is devoted to the following issues:

1. The motion of the delayed neutron and decay heat precursors, which are dragged by the liquid fuel;

2. The analysis of the helium bubbling system and of its effect on reactivity;

3. The impact of fuel compressibility on the system dynamics (especially in fast, reactivity-driven transients).

While state-of-the-art models developed for MSRs (see, e.g., Aufiero et al., 2014a; 2014b; Fiorina et al., 2014) can deal with the first problem, they are not suitable to the analysis of the helium bubbling system and of fuel compressibility effects, since they are based on single-phase, incompressible fluid dynamics solvers. To address these issues, a new multiphysics OpenFOAM model is developed in this thesis, coupling neutronics with two-phase, compressible thermal-hydraulics in the same simulation environment. The proposed model is, then, applied to the aforementioned problems, highlighting its advantages as compared to state-of-the-art approaches.

Chapter 2

The multiphysics modelling approach

Abstract

The purpose of this chapter is to present a new multiphysics tool for the analysis of the MSFR. As compared to available literature, the distinguishing characteristic of the proposed model is the direct coupling, in the same simulation environment, between neutron transport/diffusion and two-phase, compressible thermal-hydraulics. Thanks to this feature, this model has the capability to investigate aspects that cannot be studied with state-of-the-art approaches previously developed for MSRs analysis, namely: (i) the MSFR helium bubbling system and its impact on reactivity; and (ii) fuel compressibility effects in fast, reactivity-driven transients. After a review of the different modelling approaches for nuclear reactor analysis and of state-of-the-art solvers for molten salt reactors, the new multiphysics tool is described, focusing on each modelled physics and on the coupling strategy among them.

2.1 Introduction

Molten Salt Reactors (MSRs) have a distinguishing feature, namely the presence of a liquid fuel, which acts simultaneously as coolant. This peculiarity may lead to intrinsic improvements in the fuel cycle closure, reactor safety enhancement and plant simplification. Among its interesting features, the adoption of a closed thorium fuel cycle leads to an actinide inventory with lower radiotoxicity. In addition, fast reactors are also of interest for the purpose of breeding fissile isotopes from fertile nuclides, significantly extending the availability of fuel resources (Fiorina et al., 2013). Moreover, the high boiling temperature of molten salts allows operation at atmospheric pressure, reducing the mechanical load on structural materials and, as a consequence, greatly improving the safety of the system.

At the same time, the presence of a liquid fuel, introduces specific design challenges, safety issues and technological constraints that are different from both conventional water-cooled reactors (e.g., Light Water Reactors, LWRs) and other fast systems (e.g., Liquid Metal Fast Reactors, LMFRs). Notably, the delayed neutron precursors do not decay in the place they are produced, as in traditional nuclear systems, but they are dragged by the circulating fuel mixture through the reactor and the external circuits. As a consequence, the coupling between neutronics and thermo-fluid-dynamics is stronger than in traditional systems, since the fuel mixture velocity field directly influences the precursor distribution.

Moreover, as explained in Chapter 1, the adoption of a helium bubbling system is envisaged for the removal of gaseous fission products and as a possible option for reactivity control, replacing the traditional control rods. The void reactivity feedback of the bubbles introduces a further interaction between neutronics and fluid-dynamics, as the gaseous phase is dragged through the reactor by the liquid fuel. This issue is strongly specific of the MSFR, as the helium bubbling system is a completely new option that has never been adopted in conventional reactors.

In addition, fuel compressibility may play an important role on the system dynamics, introducing delays in thermal expansion feedbacks. This is expected to be particularly relevant in rapid, reactivity-driven transients (Aufiero et al., 2017), in which the characteristic times of neutronics and the propagation times of pressure waves across the reactor are comparable (being both in the order of a few milliseconds). Again, this problem is specific of liquid-fuelled reactors, in which the fission energy is directly released into the coolant. On the other hand, in solid-fuelled reactors, compressibility has a negligible impact with respect to more important feedback mechanisms such as the Doppler effect. This issue is further complicated by the presence of the bubbles, that modify the fuel compressibility both globally and locally.

This leads to an extremely non-linear problem (Figure 2.1), characterized by a strong interplay among many different physics (neutronics, two-phase fluid-dynamics, non-linear wave propagation and precursor dragging by the fuel). For these reasons, classic approaches retrieved from LWR and LMFR analysis are no longer suitable for the numerical simulation of MSR systems. Consequently, the development of the MSFR must be supported by new simulation tools, able to catch all the main physics occurring in the reactor and the coupling among them.

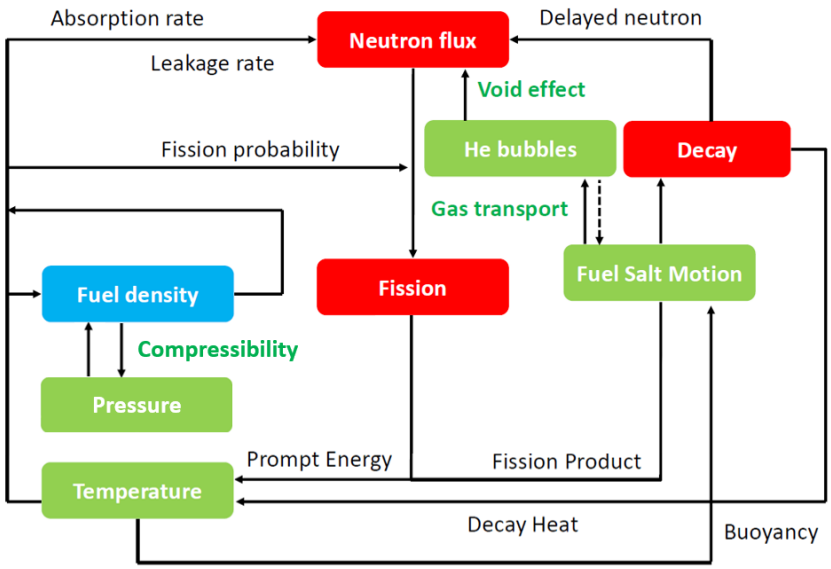

Figure 2.1. MSFR dynamics with the helium bubbling system and fuel compressibility.

2.2 State of the art

Traditionally, nuclear reactor analysis has been carried out by means of "coupled-code" techniques, i.e., by external coupling of a neutron kinetics and a thermal-hydraulics code (Avramova et al., 1997). In an "operator-splitting" fashion, these approaches use the output of a code (e.g., the neutronics code) as the input for the other code (e.g., the thermal-hydraulics code), for each time step. As pointed out by Ragusa and Mahadevan (2009) and Mahadevan et al. (2012), coupled-code techniques are generally inefficient in solving the coupling non-linearities in a time step, potentially resulting in inaccurate solutions. In addition, these approaches require the development of interfaces among different codes, which is potentially time consuming and prone to coding errors.

In molten salt reactors, the stronger coupling between neutronics and fluid-dynamics (as compared to conventional solid-fuelled systems such as LWRs and LMFRs) requires the development of new computational tools (Luzzi et al., 2012). In particular, the implementation of all the physics in the same simulation environment can provide an intrinsic way to catch the interplay among the different phenomena occurring in both operational and accidental conditions, without requiring the knowledge of different dedicated codes nor the capability to handle the connections among different tools.

The effect of circulating fuel on precursor motion (and on reactivity in turn) can be studied by coupling point-kinetics equations (Lamarsh, 2002) with simple zero-dimensional thermal-hydraulics models. In this sense, analyses have been carried out by Cammi et al. (2011a), Guerrieri et al., (2012) and by Cervi et al. (2018a). However, lumped-parameters approaches, based on time-dependent ordinary differential equations, cannot provide spatial information neither for neutronics nor fluid-dynamics quantities. In this context, coupled models for the MSFR were developed using the finite element multiphysics code COMSOL (COMSOL Multiphysics®

www.comsol.com) at Politecnico di Milano (POLIMI) and an in-house code at Delft University of Technology (TUDelft) (Fiorina et al., 2014). Both the models adopted multi-group diffusion for neutronics and a single-phase, incompressible thermal-hydraulics solver, and simulations were carried out on simplified 2D axial symmetric geometries. However, while 2D models are suitable for preliminary studies, they are inadequate for the description of many situations (e.g., single pump failures and asymmetric transients in general) that require the development of 3D models. In addition, it is well known that in 2D flows the vorticity and energy cascade dynamics are different as compared to 3D flows, due to the lack of vortex stretching (Pope, 2000), potentially leading to inaccurate predictions of the flow structures. This issue was pointed out for the specific case of molten salt reactors by Brovchenko et al. (2013). To address these issues, a 3D model of the MSFR was developed by Aufiero et al. (2014a; 2014b) with the OpenFOAM toolkit, implementing multi-group neutron diffusion, a single-phase, incompressible thermal-hydraulics model and transport equations for the delayed neutron and decay heat precursors, which are dragged by the liquid salt.

However, despite the improvements, state-of-the-art models for the MSFR still have some limitations:

- They cannot handle the presence of a gaseous phase inside the reactor;
- They approximate the fuel mixture as an incompressible liquid.

Therefore, they are not suitable for the analysis of (i) the helium bubbling system and (ii) fuel compressibility effects, whose investigation is still an open research problem. The aim of this thesis is to fill this gap, developing a new multiphysics solver that incorporates a two-phase, compressible thermal-hydraulics solver. In addition, available state-of-the-art models usually adopt multi-group diffusion to evaluate reactivity and the neutron flux. However, the adoption of more accurate neutronics models, based on transport theory, may benefit the description of the MSFR, allowing for catching phenomena that cannot be described by means of diffusion approaches. It is well known that diffusion theory has some limits, especially when it comes to predicting the neutron behaviour in heterogeneous systems (Stacey, 2007). Even though the MSFR is closer to an homogeneous reactor than traditional solid-fuelled systems, heterogeneities still exist at the blanket and reflector interfaces, or due to the presence on non-homogeneous bubble distributions in the fuel mixture. Therefore, a transport solver may be beneficial to the analysis of the MSFR helium bubbling system, especially when non-uniform bubble distributions are involved. In any case, a comparison to more accurate neutronics models can also be useful to assess the predictive capabilities and the conservativeness of neutron diffusion approaches, currently employed in the analysis of the MSFR, providing useful guidelines for future simulations. Due to the lack of specific literature on the subject, this is particularly important for the analysis of the helium bubbling system. The comparison of different modelling approaches, characterized by different levels of detail, is fundamental not only for the system design (as well as for the assessment of its safety and feasibility) but also to verify the suitability of the available simulation tools to handle this complex problem. In this perspective, a multi-group SP_3 transport model (Brantley and Larsen, 2000) is proposed in this chapter, while a more advanced discrete-ordinate model

(Stacey, 2007) is introduced and verified in Appendix A. As compared to available literature, this work presents the only CFD model coupling neutron transport and two-phase, compressible thermal-hydraulics in the same simulation environment.

2.3 The multiphysics model

In this section, the structure of the multiphysics solver adopted in this work is described. At each time step, the system thermal-hydraulics and neutronics are solved in two different cycles, as indicated in Figure 2.2. The thermal-hydraulics sub-solver is based on the standard OpenFOAM solver "*twoPhaseEulerFoam*" for the compressible fluid and the bubble modelling. As for neutronics, a multi-group diffusion model has been developed in (Cervi et al., 2017; 2018b; 2019a), while a transport model, based on the multi-group SP_3 approximation of the neutron transport equation (Brantley and Larsen, 2000) has been developed in (Cervi et al., 2018c; 2019b; 2019c).

At the beginning of the time step, the thermal-hydraulics cycle solves for the phase fractions, for the velocity of both phases, for pressure and for temperature. Picard iterations are performed until convergence is reached for the solution of the thermal-hydraulic part of the problem. Then, the neutronics cycle begins, solving for the flux, for the delayed neutron precursors and for the decay heat. After the flux (and the fission power in turn) and the decay heat have been determined, the volumetric power source field is updated and the energy equation is solved again. Once the new temperature and density fields of the fuel are calculated, the cross sections are updated and the cycle is repeated with Picard iterations until convergence is reached. In addition, a certain number of external iterations between the thermal-hydraulics and the neutronics sub-solvers is performed. The external iterations are particularly important in fast transients, in which the large thermal expansions due to steep power excursions have a strong impact on the fuel velocity field.

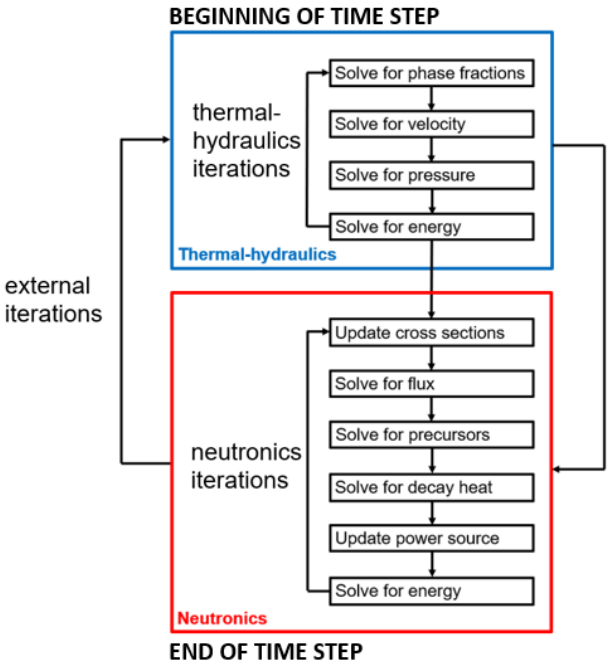

Figure 2.2. The solver structure and coupling strategy.

Summarizing, the following information is exchanged between the two sub-solvers. The void fraction, fuel temperature and density are passed from thermal-hydraulics to neutronics, in order to evaluate the cross sections. On the other hand, the power density distribution is passed from the neutronics to the thermal-hydraulics solver, in order to update temperature and density. Then, once convergence is reached in the external iterations between neutronics and thermal-hydraulics, the governing equations are integrated in time, moving to the following time step.

2.3.1 The thermal-hydraulics model

The need for a solver for a two-phase compressible fluid is due to the role that the salt compressibility plays in fast transients, and to the presence of the online bubbling system foreseen for fission product removal and reactivity control. In the following sub-section, a review of the main numerical methodologies available in literature for the simulation of two-phase flows is presented. Afterwards, the two-fluid (or Euler-Euler) approach, selected in this thesis work, is introduced.

2.3.1.1 A review of numerical methods for two-phase flow modelling

Several methods of different complexity are available for the analysis of two-phase flows. Free-surface methods are numerical techniques in which the topology of the liquid-gas interface is an explicit outcome of the solution (Rusche, 2002). These techniques can be classified in three groups (McHyman, 1984), as shown in Fig 2.3:

- *Surface tracking methods:* a sharp interface is tracked my means of marker particles or segments (Figure 2.3a).

- *Moving mesh methods:* the interface is associated with vertices of the computational mesh, which are displaced in order to preserve its sharpness (see Figure 2.3b).

- *Volume tracking methods:* the interface between two different fluids is tracked by means of indicator functions, such as volume fractions (see Figure 2.3c), set levels or phase-fields.

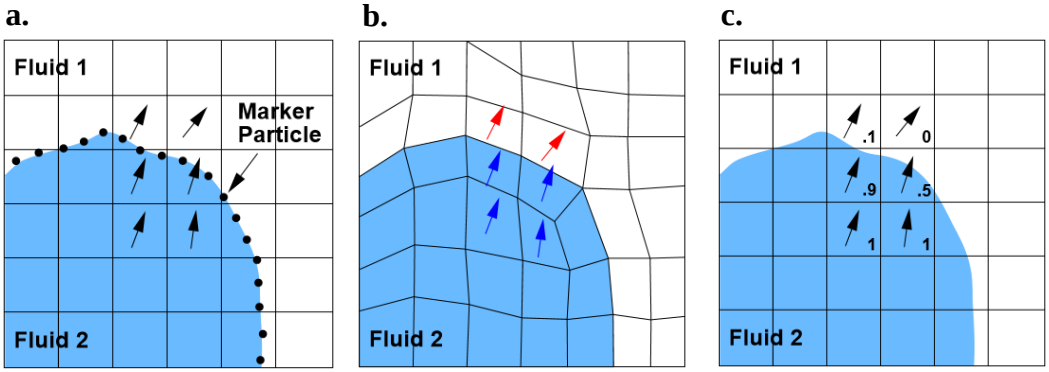

Figure 2.3. Free-surface techniques (from Rusche, 2002). (a) Surface tracking method: the interface is tracked with marker points. (b) Moving mesh method: the interface is tracked by mesh vertices. (c) Volume tracking method: the interface is tracked by a volume-fraction function.

Surface tracking and moving mesh methods are able to mark the exact position of the interface, preserving its sharpness throughout the simulation. However, marker points/segments or mesh vertices must be relocated, adding complexity when the interface undergoes large deformations. Additional difficulties arise when the interface topology changes (e.g., in case of merging of two or more interfaces). Volume tracking methods can reduce this complexity by introducing indicator functions, but interfaces can be diffused or dispersed as they are advected (Rusche, 2002). Among volume tracking techniques, the volume-of-fluid (VOF) method is based on the reconstruction of a sharp interface from the volume fraction distribution and on its subsequent advection. The VOF method is widely used in the CFD community, since the direct solution of volume fraction balance equations can potentially guarantee mass conservation exactly (Baraldi et al., 2014).

Many multiphase problems encountered in engineering applications, such as in the case of dispersed or mixed phases, are characterized by extremely complex and deformable interfaces. In this context, interface tracking often exceeds present computational capabilities. This is especially true when liquid-gas interfaces are characterized by small scales as compared to the system dimensions and a high level of detail is needed to solve the local instances of the flow, resulting into an unaffordable computational burden. Fortunately, knowledge of the exact location of the interface is not always of interest in industrial engineering applications, and the macroscopic aspects of the flow are often more important to the design and operation of a multiphase system (Faghri and Zhang, 2006). In this perspective, the macroscopic properties of the flow can be evaluated by means of appropriate averaging techniques, without requiring the explicit tracking of interfaces. Averaging methods can be classified into three main groups:

- *Eulerian averaging:* it is the most commonly used method since it is consistent with the control volume analysis used to derive continuum-mechanics governing equations. In the Eulerian description, the flow properties are expressed as functions of time and space coordinates, which are the independent variables of the problem. In this context, a general property $\varphi = \varphi(x, y, z, t)$ can be averaged by integrating over time and space, smoothing out instant or local variations within the domain of integration. In more details, the Eulerian time average can be obtained by integrating a given property over a finite time interval ΔT, for a fixed spatial position (x, y, z):

$$\bar{\varphi} = \frac{1}{\Delta T} \int_{\Delta T} \varphi(x, y, z, t)\, dt \tag{2.1}$$

  where ΔT is larger as compared to the time scales of local variations but smaller as compared to the macroscopic time scale of the process. In an analogous way, volume averaging is performed by integrating over a control volume ΔV centred around a spatial position (x, y, z) for a fixed time instant t. In multiphase systems, each *j*-th phase is characterized by a phase fraction α_j defined as:

$$\alpha_j = \frac{\Delta V_j}{\Delta V} \tag{2.2}$$

where ΔV_j is the portion of the control volume occupied by the *j*-th phase. In the light of this, the Eulerian volume average can be defined as follows:

$$\langle \varphi \rangle = \frac{1}{\Delta V} \sum_j \int_{\Delta V_j} \varphi(x, y, z, t)\, dV_j \tag{2.3}$$

Again, ΔV must be larger as compared to the spatial scales of local variations but much smaller than the system dimensions. For any property φ_j that is associated with the *j*-th phase, volume average can be evaluated in two different ways:

$$\langle \varphi_j \rangle_j = \frac{1}{\Delta V_j} \int_{\Delta V_j} \varphi_j(x, y, z, t)\, dV_j \quad (intrinsic\ phase\ average) \tag{2.4}$$

$$\langle \varphi_j \rangle = \frac{1}{\Delta V} \int_{\Delta V_j} \varphi_j(x, y, z, t)\, dV_j \quad (extrinsic\ phase\ average) \tag{2.5}$$

which are linked by the following relation:

$$\langle \varphi_j \rangle = \alpha_j \langle \varphi_j \rangle_j \tag{2.6}$$

- *Lagrangian averaging:* this averaging technique is directly related to the Lagrangian description of a system and requires tracking of each individual fluid particle. A general property can be expressed as $\varphi = \varphi(X, Y, Z, t)$, where X, Y and Z are the changing coordinates of a specific fluid particle and are functions of time and space independent variables, $X = X(x, y, z, t)$, $Y = Y(x, y, z, t)$ and $Z = Z(x, y, z, t)$. The Lagrangian time average can be obtained as:

$$\bar{\varphi} = \frac{1}{\Delta T} \int_{\Delta T} \varphi(X, Y, Z, t)\, dt \tag{2.7}$$

  Eq. (2.7) is applied to each distinct fluid particle moving in the domain.

- *Molecular averaging:* this technique relies on the concept of a *particle number density* $f(r, c, t)$, which is the particle density in the spatial position $r(x, y, z)$ and with velocity $c(c_x, c_y, c_z)$. This function obeys to the Boltzmann equation.

The analysis of the MSFR helium bubbling system is a typical multiphase problem in which a dispersed phase (the helium bubbles) are moving in a continuous phase (the

liquid fuel mixture). For this class of problems, Euler-Lagrange and Euler-Euler (or two-fluids) approaches are commonly used.

In the Euler-Lagrange approach, the governing equation of the continuous phase are expressed in the Eulerian frame, while Lagrangian coordinates are adopted for the dispersed phase (Fig 2.4a). This approach is useful when the motion of the single dispersed particles is of interest but can only be applied when the particle number is limited (i.e., in small-scale systems or in case of low dispersed phase fractions). Consequently, this approach becomes computationally expensive when the system dimensions are large, or the dispersed phase fraction is high.

On the other hand, in the Euler-Euler approach, both the phases are described using Eulerian conservation equations (Fig 2.4b). As compared to Euler-Lagrangian methods, this approach is characterized by lower computational requirements, since tracking of each dispersed particle is no longer required. Therefore, the Euler-Euler approach is suitable to the simulation of high-Reynolds and large-scale systems, which is the case for the MSFR. In fact, considering an average fuel density of 4125 kg/m^3, an average fuel velocity of about 1.2 m/s, a diameter of about 2 m and a dynamic viscosity of 10^{-2} Pa s (Gerardin et al., 2017), the Reynolds number is in the order of 10^6, implying a fully turbulent flow regime. For these reasons, the Euler-Euler approach is the preferred method for many practical applications, and is adopted in this work as well.

Due to the loss of information related to the Eulerian averaging process, several closure relations appear in the macroscopic balance equations. Therefore, the predictive capabilities of the two-fluids method crucially rely on the accuracy of these constitutive equations, representing a possible modelling limit for Euler-Euler approaches. This aspect is investigated in detail in Chapter 3. In addition, particular care is required to create a good quality mesh, in order to keep the phase fractions bounded between 0 and 1 and to preserve the simulation stability.

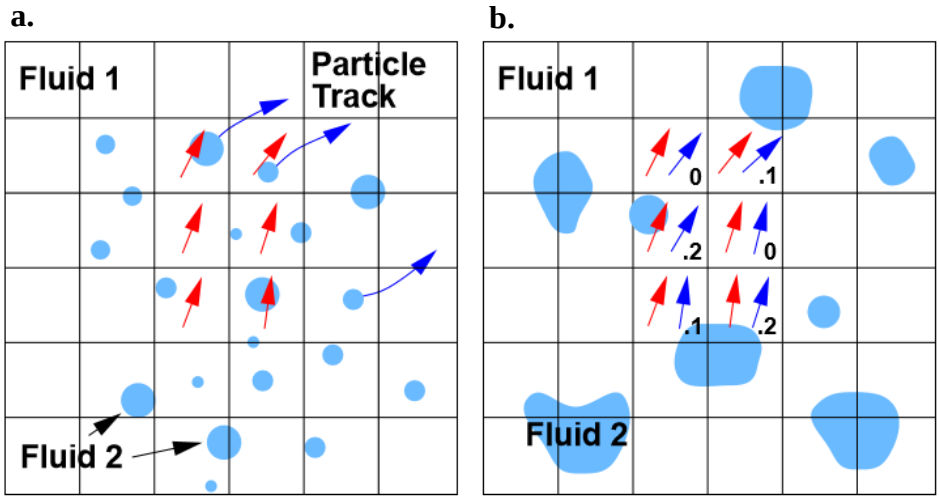

Figure 2.4. Euler-Lagrange (a) vs. Euler-Euler (b) approach (Rusche, 2002).

2.3.1.2 The Euler-Euler approach and the "twoPhaseEulerFoam" solver

In the Euler-Euler approach, both the liquid and the gaseous phases are treated as continuous, inter-penetrating fluids, each obeying to averaged conservation equations. Due to the Eulerian averaging process described by Eqs. (2.1) to (2.6), each phase is characterized by a phase fraction α_j, defined by Eq. (2.2). In the framework of an FVM discretization of the governing equations, α_j represents the portion of volume occupied by the *j*-th phase, for each cell of the computational mesh.

The averaged mass and momentum conservation for the two phases reads:

$$\frac{\partial(\rho_j \alpha_j)}{\partial t} + \nabla \cdot (\rho_j \alpha_j \boldsymbol{u}_j) + S_j = 0 \tag{2.8}$$

$$\frac{\partial \rho_j \alpha_j \boldsymbol{u}_j}{\partial t} + \nabla \cdot (\rho_j \alpha_j \boldsymbol{u}_j \boldsymbol{u}_j) = \tag{2.9}$$

$$= \nabla \cdot \alpha_j \left[-p\boldsymbol{I} + (\mu + \mu_t)\left(\nabla \boldsymbol{u}_j + (\nabla \boldsymbol{u}_j)^T\right) - \frac{2}{3}\mu \boldsymbol{I}\, div\, \boldsymbol{u}_j \right] + M_j$$

It's worth noting that the same pressure is used for both the phases. This modelling choice is justified by the fact that the dimensions of the dispersed particles are small as compared to the characteristic dimensions of the system.

A mass source term S_j is considered in the continuity equation of the gas phase to model the bubble injection/extraction. The term M_j appears in the averaged momentum equations of each phase due to non-linearity, which requires closure equations. This term takes into account the momentum transfer between the two phases, due to the forces acting at the liquid-gas interface, namely (Lathouwers, 1999):

- *Drag:* due to viscosity effects between the continuous and the dispersed phases;
- *Virtual mass forces:* due to the inertia of the carrier fluid and originating from the relative acceleration of the two phases;
- *Lift:* resulting from the rotational part of the fluid motion;
- *Turbulent dispersion:* an additional drag component due to turbulent fluctuations in the dispersed phase.

The interphase momentum transfer terms are determined with empirical models and correlations. For a review of the main closure relations available in literature, the reader is referred to (Gidaspow, 1994) and to Appendix B. As mentioned above, the predictive capabilities of the Euler-Euler approach strongly rely on the accurate evaluation of these interphase terms. Accurate modelling of the bubble diameter is also required, as it appears in different closure relations. In Chapter 3, a sensitivity analysis is carried out, to verify that the results of this thesis are not significantly dependent on the choice of different correlations.

Finally, the averaged energy balance equation reads as follows:

$$\frac{\partial \rho_j \alpha_j h_j}{\partial t} + \nabla \cdot \left(\rho_j \alpha_j \boldsymbol{u}_j h_j\right) + \frac{\partial \rho_j \alpha_j k_j}{\partial t} + \nabla \cdot \left(\rho_j \alpha_j \boldsymbol{u}_j k_j\right) = \tag{2.10}$$

$$= \alpha_j \frac{\partial p}{\partial t} + \frac{\alpha_j}{\rho_j C_{p,j}} \nabla \cdot \left((K + K_t) \nabla h_j\right) + L\,\Delta T + \rho_j \alpha_j \boldsymbol{g} \cdot \boldsymbol{u}_j + Q_f + Q_d$$

where L is an inter-phase heat transfer coefficient resulting from the averaging process while ΔT is the temperature difference between the two phases. Again, correlations are needed to evaluate L, (e.g., Ranz and Marshall, 1952). Moreover, Q_f and Q_d are the volumetric power sources due to fission and decay heat, respectively, which are provided by the neutronics model.

It is underlined that the averaged governing equations Eqs. (2.8), (2.9) and (2.10) can be applied not only to dispersed flows but also to separated and intermediate flow regimes, as no specific flow topology is specified. However, proper formulations for the interphase terms are needed, as they are strongly dependent on the nature of the flow.

The OpenFOAM toolkit is provided with a pre-implemented solver based on the Euler-Euler approach, named *"twoPhaseEulerFoam"*. This solver implements several correlations to determine the interphase terms and eddy viscosity models that incorporate the effect of the dispersed phase on turbulence (e.g., Lahey, 2005). The *twoPhaseEulerFoam* solver is widely employed and validated in many scientific and industrial fields. This solver has been employed for the CFD simulation of bubble columns by Bhusare et al. (2017), of gas-solid fluidized beds by Kia and Aminian (2017) and Gosavi et al. (2018), of particle and droplet-laden flows by Reinhardt et al. (2013) and of liquid-liquid flows in gravity settlers by Panda et al. (2017), showing in all cases a good agreement with experimental data. In the field of bioreactors, *twoPhaseEulerFoam* has been successfully validated against existing systems and then employed to optimize the performance of new designs (Bannari et al., 2011). In the pharmaceutical field, it has been used to study the inhalation of dry-powder drugs, obtaining satisfactory agreement with measurements (Kopsch et al., 2018). In addition, the *twoPhaseEulerFoam* solver is widely employed for chemical engineering applications. For example, accordance with experiments has been observed by Helmi et al. (2018) in the study of polarization concentration in fluidized-bed membrane reactors and by Demol et al. (2019) in the analysis of mass transfer in bubble columns. Other successful applications of *twoPhaseEulerFoam* can be found in (Tripathi and Buwa, 2015) for the analysis of boiling flows and in (Marti et al., 2015) for the investigation of gas-particle suspensions as heat transfer media for high-temperature concentrated solar power. Finally, excellent results have been obtained in comparisons with other codes by Passalacqua and Fox (2011).

Thus, in the light of (i) the well-proven behaviour of *twoPhaseEulerFoam*, as testified by many publications in different fields and (ii) the advantages of the Euler-Euler approach (as compared to free-surface and Euler-Lagrange ones) in the simulation of large-scale systems and high-Reynolds flows, this solver is adopted in the present work.

2.3.1.3 The treatment of compressibility in twoPhaseEulerFoam

In addition to its capability of simulating two-phase flows and, consequently, to handle the presence of helium bubbles in the MSFR, *twoPhaseEulerFoam* is also able to treat both the continuous and the dispersed phases as compressible fluids. This feature is fundamental for one of the main goals of this thesis, i.e., the analysis of fuel compressibility effects in fast, reactivity-driven transients (see Chapter 5). It is worth noting that many of the references provided in the previous section deal with compressible gases. In addition, *twoPhaseEulerFoam* has been adopted by (Nykteri et al., 2020) to study shock phenomena in high-velocity droplet impacts.

In *twoPhaseEulerFoam,* the continuity and the momentum equations are solved by means of a pressure correction algorithm – for details, see (Patankar, 1980). This method involves the solution of the momentum equation using an initial guessed pressure field. The obtained velocity field is a solution of the momentum equation but it is not granted that it satisfies the continuity equation. Thus, mass conservation is enforced by solving a correction equation for pressure, obtained by a combination of continuity and momentum equations (Moukalled et al., 2016). Then, using the corrected pressure, an updated velocity field is calculated from the momentum equation, and the procedure is iterated until the solution converges.

The continuity equation, Eq. (2.8), can be rewritten as follows:

$$\frac{\partial \alpha_j}{\partial t} + \nabla \cdot \left(\alpha_j \boldsymbol{u}_j\right) = -\frac{\alpha_j}{\rho_j}\frac{D\rho_j}{Dt} \tag{2.11}$$

Combining together Eq. (2.11) and the momentum equation, Eq. (2.9), the pressure correction equation can be written in the following compact form:

$$F(\boldsymbol{u}_1, \boldsymbol{u}_2, \nabla p) = -\sum_{j=1,2} \frac{\alpha_j}{\rho_j}\frac{D\rho_j}{Dt} \tag{2.12}$$

Expressing the density ρ_j as a function of T and p, its differential is given by:

$$d\rho_j(T,p) = \frac{\partial \rho_j}{\partial T} dT + \frac{\partial \rho_j}{\partial p} dp \tag{2.13}$$

Replacing Eq. (2.13) in Eq. (2.12):

$$F(\boldsymbol{u}_1, \boldsymbol{u}_2, \nabla p) = -\sum_{j=1,2} \frac{\alpha_j}{\rho_j}\frac{\partial \rho_j}{\partial T}\frac{DT}{Dt} - \sum_{j=1,2} \frac{\alpha_j}{\rho_j}\frac{\partial \rho_j}{\partial p}\frac{Dp}{Dt} \tag{2.14}$$

The first summation in Eq. (2.14) is simply a source term and can be obtained by solving the energy equation, given the equation of state. However, the second summation depends on pressure, introducing an implicit term into the equation. Expanding the material derivative of pressure, Eq. (2.14) can be rewritten as:

$$F(\boldsymbol{u}_j, \nabla p) = -\sum_j \frac{\alpha_j}{\rho_j}\frac{\partial \rho_j}{\partial T}\frac{DT}{Dt} - \sum_j \frac{\alpha_j}{\rho_j}\psi_j\left(\frac{\partial p}{\partial t} + \boldsymbol{u}_j \cdot \nabla p\right) \tag{2.15}$$

where $\psi_j = \partial\rho_j/\partial p$ is the isothermal compressibility of the j-th phase. For incompressible fluids, ψ_j=0 and the pressure term disappears from Eq. (2.15). On the other hand, for compressible fluids, $\psi_j \neq 0$ and the pressure term must be taken into account.

In "*twoPhaseEulerFoam*", a distinction is made upon the flow regime of each phase. In particular, in subsonic motion ($0.3 < Ma < 0.75$), the convective terms $\boldsymbol{u}_j \cdot \nabla p$ are small (Thompson, 1972) and therefore are neglected in Eq. (2.15), only considering the partial time derivative of pressure. On the other side, in transonic ($Ma \approx 1$) or supersonic ($Ma > 1$) motion, the velocity magnitude is comparable to the speed of sound (or even larger, for supersonic flows) and the convective terms are included into the pressure equation.

In the case studies considered in the present work, the velocity of molten salt and of helium bubbles is far below the sound barrier. However, large density gradients can develop when pressure waves travel into high-bubble-concentration regions, becoming steeper due to the sudden decrease of the speed of sound. This phenomenon is particularly relevant in super-prompt-critical transients, where the rapid thermal expansion of the fuel mixture generates strong pressure waves (see Chapter 5, Section 5.3.2). In these scenarios, the products $\psi_j \nabla p$ are large near liquid-gas interfaces, and the convective terms become important even if the velocity is lower than the speed of sound. For this reason, the complete form of Eq. (2.15) is employed in the analysis of fuel compressibility effects, in order to properly describe the propagation of pressure waves in case of strongly heterogeneous bubble distributions.

2.3.2 The neutronics models

Neutronics models of different complexity are developed and implemented in the framework of this thesis. In this section, a multi-group neutron diffusion solver (Cervi et al., 2017; 2018b; 2019a; 2019b; 2019c) and a multi-group SP_3 neutron transport solver (Cervi et al., 2018c; 2019b; 2019c) are presented. A more advanced discrete-ordinate transport model is introduced and verified in Appendix A.

2.3.2.1 The multi-group neutron diffusion model

The multi-group diffusion equation is one of the adopted models for the estimation of the neutron flux. Despite some limitations of this modelling choice, it is well employed in the transient analysis of nuclear reactors (Lamarsh, 2002) due to the easiness in the implementation and the relatively low computational time. For each energy group, the neutron diffusion equation reads:

$$\frac{1}{v_i}\frac{\partial \varphi_i}{\partial t} = \nabla \cdot D_i \nabla \varphi_i - \Sigma_{r,i}\varphi_i + \bar{\nu}\Sigma_{f,i}(1-\beta)\chi_{p,i}\varphi_i + S_{n,i}(1-\beta)\chi_{p,i} + S_d\chi_{d,i} + S_{s,i} \tag{2.16}$$

In the previous equation, $S_{n,i}$, S_d, $S_{s,i}$ are explicit terms which represent the neutrons released in fissions induced by neutrons from other energy groups, the delayed neutrons and the neutrons scattered from the other groups, respectively:

$$S_{n,i} = \sum_{j \neq i} \bar{\nu} \Sigma_{f,j} \varphi_j \tag{2.17}$$

$$S_d = \sum_k \lambda_k c_k \tag{2.18}$$

$$S_{s,i} = \sum_{j \neq i} \Sigma_{s,j \to i} \varphi_j \tag{2.19}$$

Due to these explicit terms, an iterative procedure among the several groups is required to achieve convergence for the neutronics description. The value of k_{eff} can be suitably changed to simulate a desired reactivity insertion. Albedo boundary conditions are adopted at the top and bottom walls of the reactor (axial reflectors) and at the radial wall (blanket salt), in order to limit the solution of the neutron diffusion equation to the fuel salt circuit only (Aufiero et al., 2014b; Fiorina et al. 2017). For the diffusion equations, the albedo boundary conditions can be expressed as follows:

$$D_i \nabla \varphi_i = -\frac{1}{2}\left(\frac{1-\alpha_i}{1+\alpha_i}\right)\varphi_i \tag{2.20}$$

where the albedo coefficients α_i are the ratios between the outgoing and the incoming neutron currents.

The precursor balance equations include the diffusion and the transport terms to allow for the fuel motion, neglecting the precursor mass transfer from the liquid to the gas phase (i.e., the precursors remain in the liquid phase and do not migrate into the bubbles):

$$\frac{\partial \rho_{\boldsymbol{l}} \alpha_{\boldsymbol{l}} c_k}{\partial t} + \nabla \cdot (\rho_{\boldsymbol{l}} \alpha_{\boldsymbol{l}} \boldsymbol{u}_l c_k) = \\ = \nabla \cdot \left(\rho_{\boldsymbol{l}} \alpha_{\boldsymbol{l}} \left(\frac{\nu}{Sc} + \frac{\nu_T}{Sc_T}\right) \nabla c_k\right) + \beta_k \sum_i \bar{\nu} \Sigma_{f,i} \varphi_i - \lambda_k \rho_{\boldsymbol{l}} \alpha_{\boldsymbol{l}} c_k \tag{2.21}$$

where Sc and Sc_t are the Schmidt and the turbulent Schmidt numbers, respectively.

In order to properly consider the decay heat on the steady-state temperature distribution (see Chapters 3 and 4) and during accidental transients, the solver is provided with equations that consider the behaviour of the isotopes responsible for the decay heat, subdivided in “decay heat groups” in a manner similar to the precursor

groups. Actually, the equations implement the balance for the precursor concentration multiplied by the average energy released by that decay group:

$$\frac{\partial \rho_l \alpha_l d_m}{\partial t} + \nabla \cdot (\rho_l \alpha_l \boldsymbol{u}_l d_m) = \\ = \nabla \cdot \left(\rho_l \alpha_l \left(\frac{\nu}{Sc} + \frac{\nu_T}{Sc_T} \right) \nabla d_m \right) + \beta_{h,l} \sum_i E_f \Sigma_{f,i} \varphi_i - \lambda_{h,l} \rho_l \alpha_l d_m \tag{2.22}$$

The unit measure of d_m is J kg^{-1}, as opposed to the delayed neutron precursors c_k, whose unit is simply kg^{-1}. For details on the delayed neutron and decay heat precursor properties as well as on the laminar and turbulent Schmidt numbers adopted throughout this thesis, the reader is referred to Appendix C.

In addition, a power iteration routine is implemented in the neutronics module of the solver for the calculation of the multiplication factor. More details are provided in Section 2.3.2.4. At the beginning of the simulation, the user can choose between the time-dependent mode or the steady-state eigenvalue mode.

2.3.2.2 The multi-group SP$_3$ neutron transport model

In the spherical harmonics (or P_N) approximation, the angular dependence of the neutron flux is expanded into the first N spherical harmonics (Bell and Glasstone, 1970). The spherical harmonics expansion results in a complex system of $(N+1)^2$ differential equations, due to the dependence on both the components μ and φ of the angular variable Ω and to complicate cross-derivative terms (Gelbard, 1962). For this reason, a simplified version of the P_N approximation – the so called SP_N equations – was proposed to overcome the model complexity while improving the accuracy with respect to the diffusion approach. The SP_N equations were first derived by Gelbard (1962), replacing the 1D second order derivative in a planar formulation of the P_N approximation with the 3D Laplacian operator, obtaining a system of $(N+1)/2$ equations (Fiorina et al., 2017). Therefore, in the specific case of the SP_3 approximation, two equations must be solved for the first two even-order flux momenta, φ_0 and φ_2. Thanks to their simplicity and to their theoretically sound derivation (Brandtley and Larsen, 2000), the SP_3 equations can be regarded as compromise between accuracy and computational cost. Being obtained from a planar formulation of the P_3 approximation, the SP_3 equations are particularly suitable for systems in which the flux variation near interfaces is mainly one directional, which is often the case for nuclear reactors (Fiorina et al., 2017). This is expected to be even more true for the specific case of the MSFR, which, as compared to traditional reactors, is more homogeneous (thus avoiding the need for higher-order SP_N models). Details on the derivation of the SP_3 equations with full anisotropic scattering terms can be found in (Duerigen, 2013). A further simplification can be obtained by neglecting anisotropic scattering within different energy groups (Fiorina et al., 2017; Duerigen, 2013), i.e., assuming that:

$$\Sigma_{sn,gg'} = 0 \qquad \text{for } g \neq g' \text{ and } n \geq 1 \tag{2.23}$$

With this assumption, the SP_3 equations are merely coupled by the isotropic scattering terms, leading to a set of diffusion-like equations, known as *SP_3 within-group form*. Introducing the variable:

$$\Phi_{0,i} = \varphi_{0,i} + 2\varphi_{2,i} \tag{2.24}$$

the SP_3 equations can be finally written as follows:

$$\frac{1}{v_i}\frac{\partial \Phi_{0,i}}{\partial t} = \nabla \cdot D_{0,i}\nabla\Phi_{0,i} - \Sigma_{r,i}\left(\Phi_{0,i} - 2\varphi_{2,i}\right) + S_{n,i}(1-\beta)\chi_{p,i} + S_d\chi_{d,i} + S_{s,i} + \frac{2}{v_i}\frac{\partial \varphi_{2,i}}{\partial t} \tag{2.25}$$

$$\frac{9}{5}\frac{1}{v_i}\frac{\partial \varphi_{2,i}}{\partial t} = \nabla \cdot D_{2,i}\nabla\varphi_{2,i} - \Sigma_{t2,i}\varphi_{2,i} + \frac{2}{5}\Sigma_{r,i}\left(\Phi_{0,i} - 2\varphi_{2,i}\right) - \frac{2}{5}S_{n,i}(1-\beta)\chi_{p,i} - \frac{2}{5}S_d\chi_{d,i} - \frac{2}{5}S_{s,i} + \frac{2}{5}\frac{1}{v_i}\frac{\partial \Phi_{0,i}}{\partial t} \tag{2.26}$$

where:

$$D_{0,i} = \frac{1}{\Sigma_{tr,i}} \tag{2.27}$$

$$\Sigma_{t2,i} = \Sigma_{t,i} - \Sigma_{s2,ii} \tag{2.28}$$

$$D_{2,i} = \frac{9}{35}\frac{1}{\Sigma_{t,i} - \Sigma_{s3,ii}} \tag{2.29}$$

As for the diffusion model, the explicit source terms $S_{n,i}$, S_d and $S_{s,i}$ are defined by Eqs. (2.17) to (2.19), replacing φ_i with $\varphi_{0,i}$, while the delayed neutron and decay heat precursors are described by Eqs. (2.21) and (2.22). Again, albedo boundary conditions are adopted in correspondence of the solid parts of the system, and for the SP_3 equations they read as follows (Fiorina et al., 2017):

$$D_{0,i}\nabla\Phi_{0,i} = -\frac{1}{2}\left(\frac{1-\alpha_i}{1+\alpha_i}\right)\left(\Phi_{0,i} - \frac{3}{4}\varphi_{2,i}\right) \tag{2.30}$$

$$D_{2,i}\nabla\varphi_{2,i} = \frac{1}{2}\left(\frac{1-\alpha_i}{1+\alpha_i}\right)\left(\frac{3}{20}\Phi_{0,i} - \frac{21}{20}\varphi_{2,i}\right) \tag{2.31}$$

The power iteration routine is also available for the SP_3 neutronics model.

2.3.2.3 Coupling between neutronics and thermal-hydraulics

Neutronics affects thermal hydraulics through the power source term in the energy equation. The source term is formed by the contributions of fission power, Q_f and, decay heat, Q_d, that appear in the energy balance equation Eq. (2.10):

$$Q_f = (1-\beta_h)\sum_i E_f \Sigma_{f,i}\varphi_i \tag{2.32}$$

$$Q_d = \sum_l \lambda_{h,l} d_l \tag{2.33}$$

On the other hand, thermal hydraulics affects neutronics through temperature and density effects, and the void feedback as well. The expression of the macroscopic cross section for a generic reaction *j* and for the energy group *i* can be expressed as follows (Aufiero et al., 2014b):

$$\Sigma_{i,j} = \left[\Sigma_{i,j}^{o} + A_{i,j} log\frac{T_{fuel}}{T_{ref}}\right]\frac{\rho_{fuel}}{\rho_{ref,fuel}}(1-\alpha_b) \tag{2.34}$$

The expression is constituted by a constant term, a logarithmic term (accounting for the temperature effect), the ratio between the actual density and a reference density (accounting for the density effect), and a correction term for the gas fraction (accounting for the presence of bubbles). In the following chapters, the constant term $\Sigma_{i,j}^{o}$ and the coefficient of the logarithmic term $A_{i,j}$ are evaluated by means of the Monte Carlo reactor physics and burnup code SERPENT 2 (Leppänen et al., 2015), using the JEFF-3.1.1 cross section library (Santamarina et al., 2009).

2.3.2.4 The power iteration routine for the evaluation of the multiplication factor

In addition to the time-dependent mode presented in Section 2.3, a power iteration routine is also implemented, in order to evaluate the system multiplication factor. At each iteration, the governing equations of the different physics are solved for steady-state conditions (i.e., setting the time derivatives to zero). According to the *k*-eigenvalue formulation of the problem (Bell and Glasstone, 1970), the mean number of neutrons produced per fission $\bar{\nu}$ in Eqs. (2.16), (2.17) and (2.21) is scaled by the multiplication factor k_{eff}*:*

$$\nabla\cdot D_i\nabla\varphi_i - \Sigma_{r,i}\varphi_i + \frac{1}{k_{eff}}\left[\bar{\nu}\Sigma_{f,i}(1-\beta)\chi_{p,i}\varphi_i + S_{n,i}(1-\beta)\chi_{p,i}\right] + S_d\chi_{d,i} + S_{s,i} = 0 \tag{2.35}$$

$$-(\boldsymbol{u}\cdot\nabla)c_k + \nabla\cdot\left(\left(\frac{\nu}{Sc}+\frac{\nu_t}{Sc_T}\right)\nabla c_k\right) + \beta_k\sum_i\frac{\bar{\nu}}{k_{eff}}\Sigma_{f,i}\varphi_i - \lambda_k c_k = 0 \tag{2.36}$$

where k_{eff} is calculated as the ratio of the neutron fission source in two subsequent power iterations:

$$k_{eff} = \frac{\int \sum_i \bar{\nu}\Sigma_{f,i}\varphi_i dV\big|_n}{\int \sum_i \bar{\nu}\Sigma_{f,i}\varphi_i dV\big|_{n-1}} \tag{2.37}$$

At each iteration, the neutron flux is normalized to the desired power level. The above procedure is iterated until k_{eff} converges to the solution. Although the steady-state neutron diffusion equation Eq. (2.35) is used to illustrate the routine, the same procedure can also be applied to the SP_3 and discrete-ordinate transport models.

2.4 Conclusive remarks

The computational simulation of a nuclear reactor is a complex multiphysics task, needing accurate solution for both neutronics and thermal-hydraulics and considering the coupling between them. This is even more important in circulating fuel nuclear reactors, in which the velocity field of the fuel has a direct impact on the precursor distribution, affecting reactor kinetics. The degree of complexity grows further if the helium bubbling system and fuel compressibility effects are taken into account, due to the strong interaction among all the physics that come into play. This challenging problem cannot be addressed neither with computational tools designed for traditional solid-fuelled reactors, nor with state-of-the-art models developed for MSRs (Aufiero et al., 2014a; 2014b; Fiorina et al., 2014), which are typically based on single-phase, incompressible fluid-dynamics solvers.

Consequently, the problems of the helium bubbling system and of fuel compressibility effects, that are fundamental to fully understand the MSFR dynamics, have never been investigated in detail. To fill this gap, a new multiphysics model has been developed and implemented into an OpenFOAM solver. Thanks to the adoption of a two-phase, compressible thermal-hydraulics solver, based on a Euler-Euler approach, the new model is able to handle the presence of helium bubble inside the reactor and to take into account the fuel mixture compressibility. In addition, as compared to state-of-the-art models that typically rely on neutron diffusion for the estimation of flux and reactivity, the neutronics module has been improved by developing an SP_3 transport model. This thesis work presents the only CFD model coupling neutron transport and two-phase, compressible thermal-hydraulics in the same simulation environment, constituting therefore a substantial step forward as compared to available multiphysics tools for the analysis of molten salt reactors.

In the remainder of the thesis, the proposed model is employed to investigate the helium bubbling system and its effect on reactivity, and the impact of fuel compressibility on the reactor dynamics as well. The analyses presented in this work are of great importance not only to shed the light on new phenomena, leading to a deeper understanding of the MSFR dynamics, but also to assess the conservativeness of state-of-the-art models.

Chapter 3

Analysis of the MSFR helium bubbling system

Abstract

The aim of this chapter is to study the MSFR helium bubbling system. Firstly, the neutron diffusion and the SP_3 neutron transport models described in Chapter 2 are tested against Monte Carlo simulations of the MSFR, in order to verify their correct implementation and to assess their accuracy. Then, a multiphysics analysis of the MSFR is carried out, focusing on the helium bubbling system and the coupling between the two-phase flow and reactivity. The presence of helium bubbles in the reactor is handled by using the two-fluid thermal-hydraulics model introduced in the previous chapter. The void reactivity coefficient is evaluated on the basis of the bubble spatial distribution calculated by the multiphysics solver. Then, results are compared to simpler simulations carried out assuming uniform (instead of calculated) bubble distributions, highlighting significant differences between the two approaches. This points out that the void reactivity feedback is strongly influenced by spatial and neutron importance effects and that an accurate evaluation of the void fraction distribution is fundamental to correctly estimate reactivity and the void coefficient in turn. Afterwards, a sensitivity analysis is carried out to compare the main models and correlations available in literature to determine the bubble diameter and to estimate the momentum and heat transfer between the liquid and gas phases. It is shown that the void reactivity coefficient is not significantly affected by the choice of different correlations, pointing out that the results of this chapter are consistent and reliable. Due to the high number of simulations presented in this analysis, a simplified 2D axial-symmetric geometry is adopted to reduce computational times. For the 3D modelling of the MSFR, the reader is referred to Chapter 4. The outcome of this study sheds the light on the impact of the MSFR helium bubbling system on reactivity, constituting therefore a starting point for the optimization of this innovative design option as well as for the development of appropriate control strategies.

The content of this chapter is based on:

Cervi, E., Lorenzi, S., Cammi, A., Luzzi, L., 2017. An Euler-Euler multi-physics solver for the analysis of the helium bubbling system in the MSFR, NENE 2017 26th International Conference Nuclear Energy for New Europe, Bled, Slovenia, September 11-14, 2017.

Cervi, E., Lorenzi, S., Cammi, A., Luzzi, L., 2019b. Development of an SP_3 neutron transport solver for the analysis of the Molten Salt Fast Reactor, Nuclear Engineering and Design 346, 209-219.

3.1 Introduction

As explained in the previous chapters, a helium bubbling system is foreseen in the MSFR for a more efficient removal of gaseous fission products (Delpech et al., 2009). This system is also envisaged as a possible option for reactivity control, exploiting the void reactivity effect of the gas bubbles. This design choice would replace the use of control rods, traditionally employed in conventional solid-fuelled reactors.

Most of the computational tools currently available for nuclear reactor analysis are not suitable to study this system, as they are tailored to the needs of traditional light water reactors. At the same time, state-of-the-art models specifically developed for molten salt reactors (see, e.g., Aufiero et al., 2014a; 2014b; Fiorina et al., 2014) are not able to handle the presence of bubbles in the reactor, as they implement standard single-phase fluid-dynamics solvers. Consequently, the only way to account for bubbly flow is by assuming a uniformly distributed gaseous phase (i.e., modelling the void fraction as a uniform density effect, independently from the velocity field of the fuel). This is clearly an oversimplifying hypothesis, since bubbles generally have a non-uniform spatial distribution, dependent on the flow conditions in the reactor.

In this perspective, the adoption of a two-phase fluid-dynamics model is required to gain a deeper insight into the problem of the helium bubbling system and of its effect on reactivity. The multiphysics model described in Chapter 2 is suitable to this purpose, being able to evaluate the non-uniform distribution of the gaseous phase in the reactor and to estimate the void reactivity feedback of the bubbles. A detailed analysis of this complex problem is a necessary step for future optimizations of the MSFR design parameters and for the development of appropriate control strategies. In addition, even if alternative options will be preferred for reactivity control, the helium bubbling system will still be employed for the fission gas removal, and understanding its impact on reactivity will still be necessary to assess the safety and the feasibility of this design choice. In this frame, it is underlined that the purpose of the present study is the numerical modelling of the helium bubbling system, while the optimization of the reactor design, its safety assessment and the development of reactivity control strategies are not in the scope of this thesis.

Finally, the adoption of a two-phase thermal-hydraulics model is also of interest to assess the conservativeness of state-of-the-art, single-phase solvers and of the simplifying assumptions they rely on.

The remainder of this chapter is organized as follows. In Section 3.2, the multi-group neutron diffusion and SP_3 neutron transport solvers are tested against a Monte Carlo model of the MSFR, to verify their correct implementation and accuracy. In Section 3.3, the multiphysics coupling between neutronics and two-phase fluid dynamics is investigated on a 2D axial-symmetric geometry of the MSFR, evaluating the void reactivity coefficient on the basis of the bubble spatial distribution calculated by the multiphysics model. In Section 3.4, a sensitivity analysis is carried out to compare the main models and correlations available in literature to evaluate the bubble diameter and the momentum and heat exchange between the liquid and the gaseous phases. Finally, conclusive remarks are provided in Section 3.5.

3.2 Verification of the neutronics models

In this section, the neutron diffusion and the SP_3 neutron transport solvers presented in Chapter 2 are compared to simulations carried out with the Monte Carlo reactor physics code Serpent 2 (Leppänen et al., 2015). To this aim, a simplified cylindrical geometry is adopted (Brovchenko et al., 2013). In the Serpent model, this geometry is reproduced in three dimensions, also including the solid regions of the reflectors, fertile blanket and boron carbide shield (see Figure 3.1). Conversely, in the OpenFOAM model a 2D axial-symmetric geometry is adopted (Figure 3.2), solving the governing equations in cylindrical coordinates. In addition, only the liquid part of the reactor is simulated (in order to avoid the modelling of the solid parts and to reduce the computational effort), taking in account the fertile blanket and the reflectors by imposing albedo boundary conditions.

The purpose of the comparison is (i) to verify the accuracy of the implemented models and (ii) to assess the improvement in the predictive capabilities of the SP_3 approach over the diffusion one, with specific application to the analysis of the MSFR. However, Monte Carlo and deterministic methods are two completely different approaches to study reactor physics, each of them having different advantages and drawbacks, as discussed below. Such differences may complicate a direct comparison between the two approaches, especially when complex multiphysics systems - such as the MSFR - are involved. For this reason, particular care is required to carry out all the simulations - the deterministic and the Monte Carlo ones - under conditions and modelling assumptions that make a comparison possible.

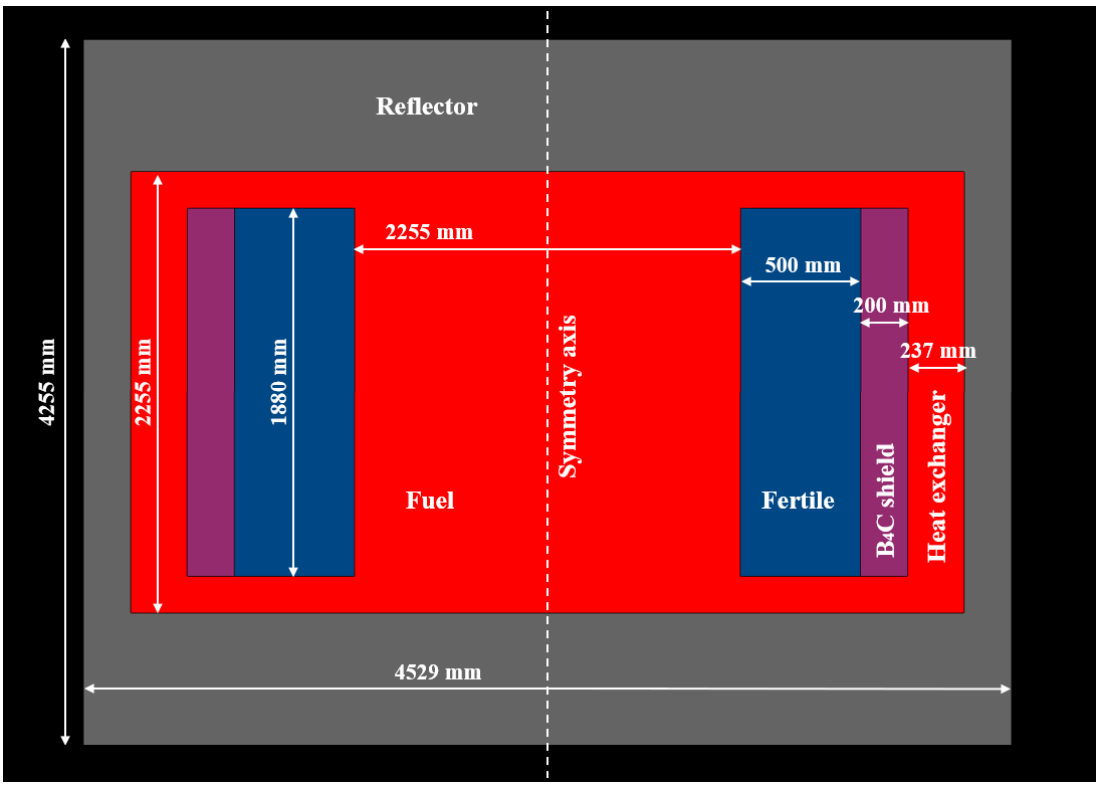

Figure 3.1. Serpent simplified model of the MSFR.

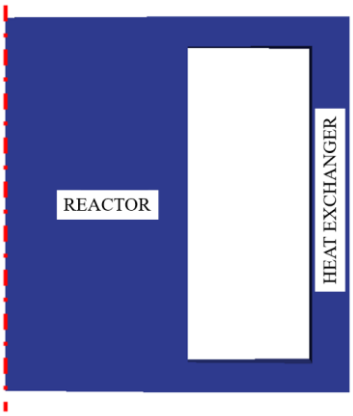

Figure 3.2. OpenFOAM simplified model of the MSFR.

Typically, Monte Carlo simulations are carried out assuming uniform temperatures and densities for each material. In addition, standard Monte Carlo codes cannot handle the precursor motion due to the circulating fuel, since they were originally developed for solid-fuelled reactors (except from a preliminary development presented by Aufiero et al., 2017). On the other hand, the OpenFOAM multiphysics solver calculates space-varying temperature and density fields and implements transport equations for the moving precursors. In addition, the CFD model has the capability to handle the presence of bubbles inside the reactor, calculating their spatial distribution (which is, in general, non-uniform). As discussed above, spatial non-uniformities are usually not considered in Monte Carlo simulations, possibly hindering a direct and significant comparison between the two approaches. To overcome this issue, static fuel is also assumed in the OpenFOAM model, together with the adoption of uniform a temperature, density and bubble distribution.

All the Monte Carlo calculations are carried out using 1.8 billion neutron histories (15000 generations of 120000 particles), obtaining a 1 pcm 1-σ uncertainty on the multiplication factor. The convergence of the fission source has been ensured analysing the Shannon entropy and adopting 1000 inactive cycles. The JEFF-3.1.1 (Santamarina et al., 2009) cross section library is selected for the Monte Carlo simulations. On the other hand, the OpenFOAM calculations are carried out adopting six energy groups, using homogenized cross sections generated by the Serpent model. The relative uncertainty of the generated multi-group cross sections is in the order of 10^{-2} %. Six-group albedo coefficients are also evaluated with Serpent 2 by means of surface current detectors, placed at the liquid region boundary. The coefficient values depend on each specific material interface.

The energy group subdivision adopted in this work is shown in Table 3.1. This energy structure has been tested in previous works (Fiorina, 2013; Fiorina et al., 2013) against ERANOS (using 33 and 1968 energy groups) and Serpent, showing that it is capable of reproducing the overall shape of the neutron spectrum, and obtaining a good agreement in the prediction of different neutronics parameters. For details on delayed neutron and decay heat precursor properties adopted in this analysis, the reader is referred to Appendix C.

Two sets of cross sections are generated for T_{fuel} equal to 900 K and 1200 K, assuming a uniform fuel density of 4125 kg/m^3. Recalling Eq. (2.34), cross sections depend on fuel temperature, fuel density and void fraction. In particular, the term $\Sigma_{i,j}^{o}$ corresponds to cross section value at 900 K, while $A_{i,j}$ is evaluated by interpolating the cross sections between 900 and 1200 K.

Firstly, the multiplication factor is evaluated by means of the Serpent and of the OpenFOAM models, using both the SP_3 and the diffusion solvers. Results for different temperatures and void fractions are compared in Table 3.2.

In addition, the Doppler constant is calculated as:

$$K_D = \frac{\tilde{\rho}\left(T_{fuel,2}\right) - \tilde{\rho}(T_{fuel,1})}{log\left(\frac{T_{fuel,2}}{T_{fuel,1}}\right)} \tag{3.1}$$

The values of the Doppler constants evaluated at different fuel temperature ranges using Serpent, the SP_3 and the diffusion solvers are listed in Table 3.3. The aim of this comparison is to assess the agreement between the OpenFOAM and the Monte Carlo results not only at the interpolation temperatures (i.e., 900 K and 1200 K), but also at intermediate values.

Then, the void reactivity coefficient is evaluated using the following relation:

$$\alpha_{void} = \frac{\tilde{\rho}(\bar{\alpha}_b) - \tilde{\rho}(0)}{\bar{\alpha}_b} \tag{3.2}$$

where $\bar{\alpha}_b$ is the core-average percent void fraction, assumed, for the present calculation, equal to 1%. As explained above, a uniform void fraction is adopted in this analysis. A comparison of the void coefficients obtained with Serpent, the SP_3 and the diffusion models can be found in Table 3.4. Note that a uniform variation of the void fraction is equivalent to a uniform density effect. Therefore, the void coefficients can be easily expressed in terms of pcm per unit density, and the results of Table 3.4 are also representative as a comparison of the density reactivity coefficients.

Finally, a comparison of the axial and radial total flux profiles at reactor mid-planes is presented in Figs. 3.3 and 3.4, respectively, while the peak values of the flux are compared in Table 3.5. In all the simulations, the total fission power is normalized to 3000 MW to evaluate the flux distribution.

Table 3.1. Energy group division adopted in the present work.

Energy group	Energy ranges (MeV)
1	$2.23 \div 20.00$
2	$4.98 \cdot 10^{-1} \div 2.23$
3	$2.48 \cdot 10^{-2} \div 4.98 \cdot 10^{-1}$
4	$5.53 \cdot 10^{-3} \div 2.48 \cdot 10^{-2}$
5	$7.49 \cdot 10^{-4} \div 5.53 \cdot 10^{-3}$
6	$0 \div 7.49 \cdot 10^{-4}$

Table 3.2. Multiplication factor from the Monte Carlo, SP_3 and diffusion models.

T_{fuel} **(K)**	$\bar{\alpha}_b$ **(%)**	$k_{SERPENT}$ **± 2-σ uncertainty**	k_{SP3} (difference with respect to Serpent in pcm)	$k_{diffusion}$ (difference with respect to Serpent in pcm)
900	0	0.991320 ± 0.000020	0.985082 (-623.8)	0.983806 (-751.4)
900	1	0.989860 ± 0.000020	0.983585 (-626.7)	0.982269 (-759.1)
900	2	0.988310 ± 0.000020	0.982048 (-626.2)	0.980691 (-761.9)
900	3	0.986780 ± 0.000020	0.980474 (-630.6)	0.979075 (-770.5)
1000	0	0.987400 ± 0.000020	0.981158 (-624.2)	0.979892 (-750.8)
1100	0	0.983900 ± 0.000020	0.977676 (-622.4)	0.976419 (-748.1)
1200	0	0.980720 ± 0.000020	0.974551 (-616.9)	0.973302 (-741.8)

Table 3.3. Doppler coefficient from the Monte Carlo, SP_3 and diffusion models.

T_{fuel} **(K)**	$K_{D,SERPENT}$ **± 2-σ uncertainty (pcm)**	$K_{D,SP3}$ **(pcm)** (difference with respect to Serpent in pcm)	$K_{D,diffusion}$ **(pcm)** (difference with respect to Serpent in pcm)
$900 \div 1000\ K$	-3801.0 ± 38.8	-3853.4 (-52.4)	-3853.4 (-52.4)
$1000 \div 1100\ K$	-3779.9 ± 43.2	-3808.5 (-28.9)	-3808.5 (-28.4)
$1100 \div 1200\ K$	-3787.5 ± 47.6	-3769.4 (-18.1)	-3769.4 (-18.1)

Table 3.4. Void reactivity coefficient from the Monte Carlo, SP_3 and diffusion models.

$\bar{\alpha}_b$ **(%)**	$\alpha_{void,SERPENT}$ **± 2-σ uncertainty (pcm/%)**	$\alpha_{void,SP3}$ **(pcm/%)** (% relative difference with respect to Serpent)	$\alpha_{void,diffusion}$ **(pcm/%)** (% relative difference with respect to Serpent)
1	-148.8 ± 4.0	-154.7 (-4.0)	-159.1 (-6.9)
2	-153.6 ± 2.0	-156.8 (-2.1)	-161.4 (-5.1)
3	-154.7 ± 1.4	-159.0 (-2.8)	-163.7 (-5.8)

Table 3.5. Peak total fluxes from the Monte Carlo, SP_3 and diffusion models.

Serpent peak flux ± 2-σ uncertainty (neutrons/cm^{2}s)	**SP_3 peak flux (neutrons/cm^{2}s)** (% relative difference with respect to Serpent)	**Diffusion peak flux (neutrons/cm^{2}s)** (% relative difference with respect to Serpent)
$(9.24 \pm 0.04) \cdot 10^{13}$	$9.79 \cdot 10^{13}$ (6.0)	$9.89 \cdot 10^{13}$ (7.0)

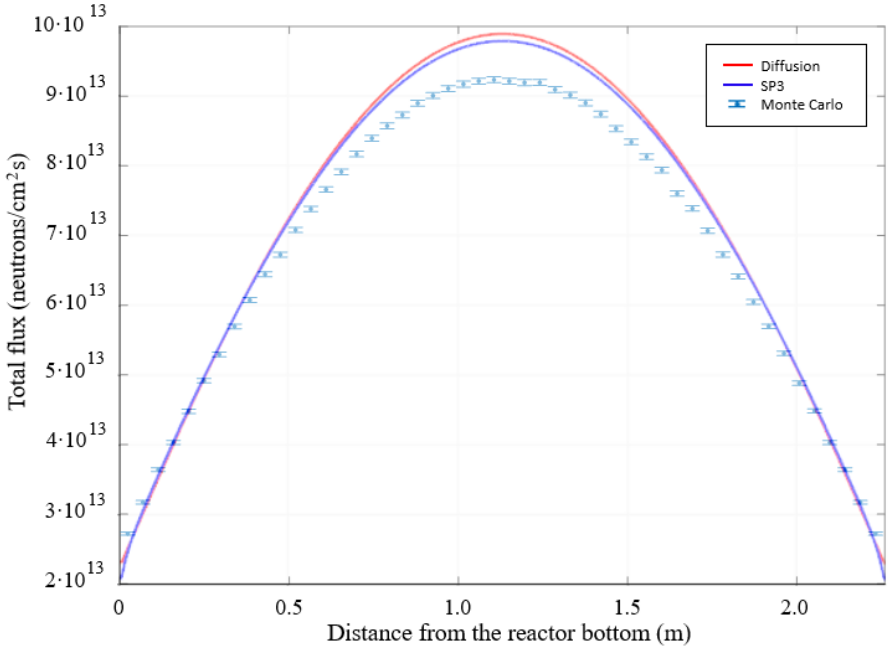

Figure 3.3. Total flux axial profiles (along the reactor symmetry axis) from the Monte Carlo, SP_3 and diffusion models.

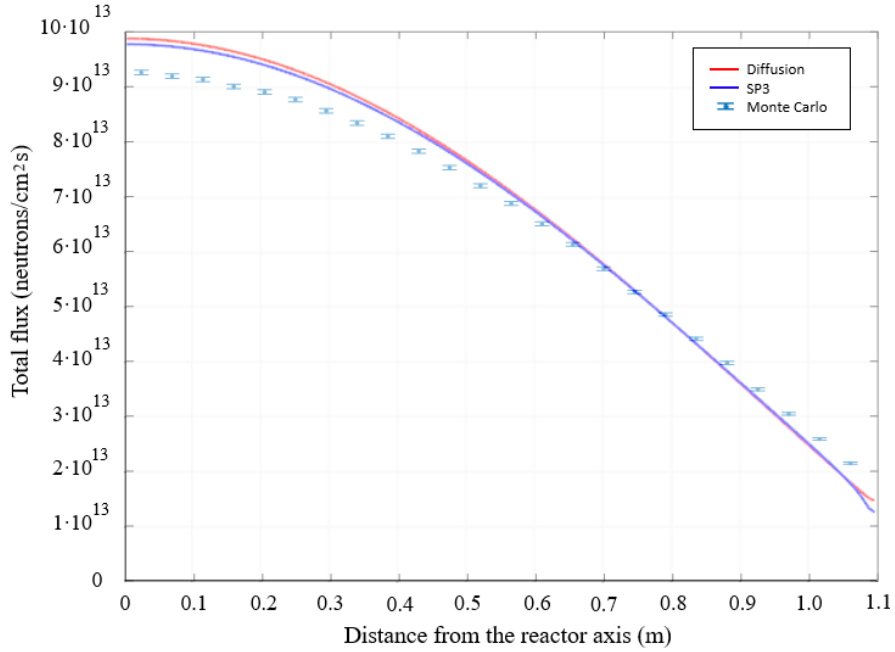

Figure 3.4. Total flux radial profiles (at reactor half-height) from the Monte Carlo, SP_3 and diffusion models.

3.2.1 Discussion of results

The SP_3 solver shows a better agreement with Monte Carlo simulation, as compared to the diffusion one, in the prediction of the multiplication factor (Table 3.2). In particular, the error with respect to the Serpent model is reduced from ~750-770 pcm with the diffusion solver to ~620-630 pcm with the SP_3 solver. As for the Doppler

constant, the outcomes of the SP_3 and of the diffusion solvers are coincident up to the first decimal digit and are in excellent agreement with Monte Carlo results in all the investigated temperature ranges (Table 3.3). Finally, with the SP_3 solver, the error in the void reactivity coefficient is reduced from ~5-7% to ~2-4% (Table 3.4). General better agreement is also shown by the SP_3 total flux profiles (Figures 3.3 and 3.4), especially in the centre of the reactor, where the peak value of the total flux is predicted with a smaller error (6% vs. 7%) – see Table 3.5.

In general, both the SP_3 and the diffusion results are in good agreement with the Monte Carlo solutions, suggesting that both those solvers are correctly implemented. The 600-700 pcm errors in the multiplication factor calculations are mainly due to the adoption of a different geometry between the Monte Carlo and the OpenFOAM model, being the latter without the blanket and the reflectors zones. This lack is partially balanced with the albedo boundary conditions, that are relevant in order to reduce the complexity of the coupled neutronics and thermal-hydraulics simulations. In this regard, it is worth mentioning that the purpose of the present work is not the accurate estimation of absolute reactivity, but rather the evaluation of reactivity variations (i.e., the reactivity coefficients) which are well predicted using albedo boundary conditions. In particular, the aim of this work is the correct evaluation of the void reactivity coefficient, which is of interest for the analysis of the helium bubbling system. Therefore, the k_{eff} errors obtained with the albedo boundary conditions are acceptable for the purposes of this study. In addition, these errors are compatible with other works carried out with the same approach (e.g., Aufiero et al., 2014b). In order to prove the main source of discrepancy in the multiplication factor estimation between the Monte Carlo and OpenFoam model, a simplified version of the latter has been developed, including the reflectors and the blanket in the OpenFOAM model (Figure 3.5). In this case, the errors are reduced to about -230 pcm with the SP_3 module and to about -260 with the diffusion module (Table 3.6). Flux differences among the three models are also strongly reduced (Table 3.7).

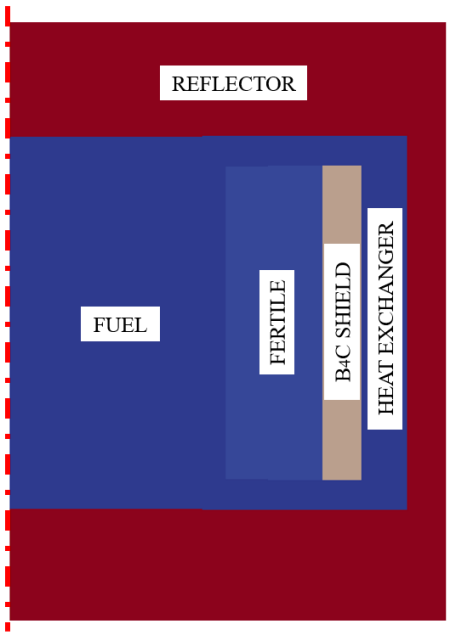

Figure 3.5. OpenFOAM simplified model of the MSFR including the solid blanket and reflectors.

Table 3.6. Multiplication factor from the Monte Carlo, SP_3 and diffusive neutronics models (for $T_{fuel} = 900\ K$ and $\bar{\alpha}_b = 0$).

$k_{SERPENT}$ ± 2-σ uncertainty	k_{SP3} (difference with respect to Serpent in pcm)	$k_{diffusion}$ (difference with respect to Serpent in pcm)
0.991320 ± 0.000020	0.989035 (-228.5)	0.988753 (-256.7)

Table 3.7. Peak total fluxes from the Monte Carlo, SP_3 and diffusion models.

Serpent peak flux ± 2-σ uncertainty (neutrons/cm^{2}s)	SP_3 peak flux (neutrons/cm^{2}s) (% relative difference with respect to Serpent)	Diffusion peak flux (neutrons/cm^{2}s) (% relative difference with respect to Serpent)
$(9.24 \pm 0.04)\cdot10^{13}$	$9.37\cdot10^{13}$ (1.4)	$9.70\cdot10^{13}$ (5.0)

3.3 Calculation of the void reactivity coefficient

The purpose of this section is the analysis of the MSFR helium bubbling system and of its effect on reactivity, evaluating the void reactivity coefficient of the bubbles. As opposed to Section 3.2, where isothermal and static fuel was assumed, the temperature, density, void fraction and velocity fields of the fuel are evaluated by the multiphysics solver, according to the coupling scheme described in Chapter 2. The helium bubbles are injected at the bottom of the reactor (Allibert et al., 2016) and are extracted at the top, before the heat exchanger region (see Figure 3.6), even if no detailed design information is currently available on the helium bubbling system. In particular, the injection and extraction systems have been modelled as a mass source and sink, respectively, since no detailed information is currently available on the design of these systems. No-slip boundary conditions are imposed for the fuel and gas velocity at the reactor walls, while atmospheric pressure is imposed at the expansion tank. The pump and the heat exchanger are modelled as a momentum source and heat sink, respectively, while he Lahey k-ε turbulence model (Lahey, 2005) has been adopted to account for the contribution of the dispersed gaseous phase on eddy viscosity.

To estimate the momentum transfer between the liquid and the gaseous phases, the Schiller-Naumann correlation (Schiller and Naumann, 1933; Rusche, 2002) is selected for the evaluation of the drag coefficient (see Appendix B for details):

$$C_D = \begin{cases} \dfrac{24(1 + 0.15Re_b^{0.687})}{Re_b} & for\ Re_b < 1000 \\ 44 & for\ Re_b \geq 1000 \end{cases} \tag{3.3}$$

The bubble Reynolds number Re_b is defined as:

$$Re_b = \left|\boldsymbol{u}_{gas} - \boldsymbol{u}_{liq}\right| d_b/\nu \tag{3.4}$$

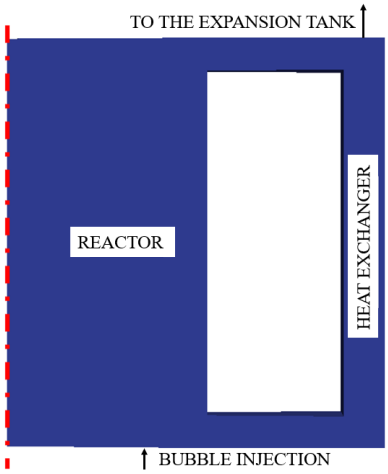

Figure 3.6. OpenFOAM model of the MSFR with the helium bubbling system.

The average bubble diameter d_b is estimated by means of the following isothermal power law:

$$d_b = d_0 \left(\frac{p_0}{p}\right)^{1/3} \tag{3.5}$$

in which the reference diameter d_0 and pressure p_0 are required as input parameters. In typical industrial applications, the bubble diameter ranges from 1 to 5 mm (Lance et al., 1996). In this work, it is assumed that $d_0 = 3$ mm (based on the assumption that this is the injector diameter) and $p_0 = 1$ atm (which is the operating pressure of the reactor). A constant coefficient correlation is adopted for virtual mass forces, with $C_{VM} = 0.5$ (Rusche, 2002). Lift is not considered in the present work, assuming that the bubble size is sufficiently small to neglect the effect of vorticity on the momentum exchange between phases. Moreover, turbulent dispersion is also neglected. Finally, the Ranz-Marshall correlation (Ranz and Marshall, 1952) is adopted to evaluate the heat transfer between the fuel and the bubbles:

$$Nu = \frac{L d_b^2}{6 \kappa_l \alpha_g} = 2 + 0.6\, Re_b^{1/2} Pr^{1/3} \tag{3.6}$$

Aiming at justifying these assumptions, a sensitivity analysis is presented in Section 3.4, to compare the main closure relations available for the estimation of these terms. The set of boundary conditions and modelling choices described above will be used throughout the remainder of the manuscript.

A preliminary evaluation of the bubbly flow contribution to the system reactivity can be made by assuming a uniform bubble distribution. This can be achieved by Monte Carlo simulation or with a standard single-phase thermal-hydraulic model, simply correcting the fuel density by a uniform void fraction. On the other hand, the real distribution of the bubbly flow inside the reactor is not uniform, since the bubbles are dragged by the fuel mixture. For this reason, the void coefficient (Eq. 3.2) needs to be evaluated accounting for the spatial and neutron importance dependence of the

bubble reactivity effect. The multiphysics solver, thanks to the coupling between neutronics and two-phase thermal-hydraulics, has the capability to deal with this aspect of the void reactivity effect. In the light of this, the void coefficient is evaluated with two different approaches:

- Case 1: the bubble spatial distribution calculated by the multiphysics solver is considered.

- Case 2: a uniform bubble distribution is assumed, with the same core-average value of Case 1.

In both cases, the void coefficient is calculated with Eq. (3.2), using the energy-group subdivision of Table 3.1. The multiplication factor and the void reactivity coefficient evaluated at different void fractions with the diffusion and the SP_3 models are listed in Tables 3.8 and 3.9, respectively. Figure 3.7 shows the void fraction distributions (i.e., the volume fraction occupied by the helium) and the power density fields evaluated by means of the SP_3 module for $\bar{\alpha}_b$ equal to 0.635% and 1.468% (these are the steady-state average void fractions for two different helium injection flow rates, 0.1 and 0.2 g/s, respectively). As in the remainder of the manuscript, convergence of the power iteration cycles is considered achieved when the residuals of neutron flux equations fall below 10^{-7}.

Table 3.8. Multiplication factor and void faction evaluated with the diffusion solver.

Core-average void fraction (%)	Multiplication factor		Void coefficient (pcm/%)	
	Case 1 (calculated bubble distribution)	*Case 2 (uniform bubble distribution)*	*Case 1 (calculated bubble distribution)*	*Case 2 (uniform bubble distribution)*
0	0.976288	0.976288	-	-
0.288	0.975304	0.975844	-358.8	-161.8
0.635	0.974301	0.975304	-329.0	-162.7
1.030	0.973271	0.974684	-308.3	-163.7
1.468	0.972216	0.973990	-292.2	-164.6

Table 3.9. Multiplication factor and void faction evaluated with the SP_3 solver.

Core-average void fraction (%)	Multiplication factor		Void coefficient (pcm/%)	
	Case 1 (calculated bubble distribution)	*Case 2 (uniform bubble distribution)*	*Case 1 (calculated bubble distribution)*	*Case 2 (uniform bubble distribution)*
0	0.977592	0.977592	-	-
0.288	0.976652	0.977157	-341.9	-158.1
0.635	0.975674	0.976632	-316.7	-158.3
1.030	0.974669	0.976028	-297.8	-159.1
1.468	0.973642	0.975352	-282.7	-160.0

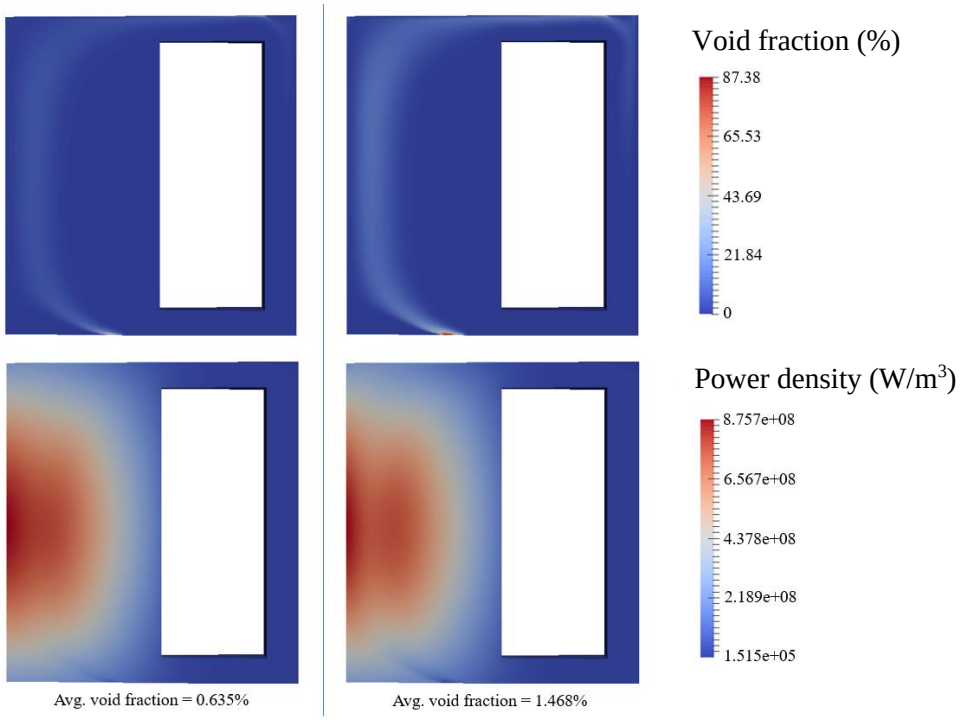

Figure 3.7. Void fraction and power density distributions at 0.635% (left) and 1.468% (right) core average void fraction. The SP_3 module is used in these calculations.

Runtimes are 40 and 47 minutes for the diffusion and SP_3 solvers, respectively, carrying out the simulations with eight MPI (Gropp et al., 2014) parallel threads and using an Intel Core i7-6700HQ CPU with a clock speed of 2.60 GHz. The 2D mesh has 43484 cells, ensuring that results are independent from further refinements (in particular, doubling the number of cells does not affect the results of the analysis).

3.3.1 Discussion of results

Both with the diffusion and the SP_3 models, a noticeable difference is observed between the void coefficients obtained in Case 1 (calculated bubble distribution) and in Case 2 (uniform bubble distribution). In particular, when a uniform distribution is assumed, the void reactivity coefficient has a value of about -160 pcm/%. This value is still comparable with the results of Section 3.2 for the static and isothermal fuel, even if some differences arise due to the different temperature and precursor distribution. On the other hand, when the bubble distribution calculated by the multiphysics solver is considered, the void coefficient strongly increases (i.e., it becomes more negative), reaching values between -360 and -280 pcm/%. This outcome highlights a strong dependence of the void reactivity effect on spatial and neutron importance effects. In particular, in Case 1 (calculated bubble distribution), most of the bubbles are concentrated in the central region of the reactor, where the neutron importance is higher. For this reason, the void reactivity effect is stronger than in Case 2 (uniform bubble distribution), in which a significant part of the bubbles is located in the peripheral regions of the reactor, where the neutron importance is lower. In addition, the presence of bubbles in the centre of the system shifts the power production towards the outer regions of the core. This can lead in turn to an increase of neutron leakages, possibly contributing to the higher void coefficient observed in Case 1 (calculated

bubble distribution). Moreover, when the calculated bubble distribution is considered (Case 1), it can be observed that the void coefficient decreases as the average void fraction increases. In fact, the bubbly flow removes fissile from the centre of the reactor (see Figure 3.7), reducing the neutron importance in this region. As a consequence, the marginal reactivity effect due to further helium addition decreases for higher void fractions. These results highlight that single-phase approaches assuming a uniform bubble distribution are strongly non-conservative, as they would lead to a significant underestimation of the void coefficient. Consequently, in case of an accidental decrease of the void fraction (e.g., a failure of the helium bubbling system), the resulting positive reactivity insertion would also be underestimated. It's also worth noting that results may be strongly influenced by the position of the bubble injection system.

As in Section 3.2, the diffusive neutronics model overestimates the void coefficient, as compared to the SP_3 model, both in Cases 1 and 2. For comparison, the absolute and relative percent differences between the void coefficients obtained with the diffusion and the SP_3 modules are reported in Table 3.10 for Case 1 (calculated bubble distribution) and in Table 3.11 for Case 2 (uniform bubble distribution). Even if general good agreement is obtained, the error between the two approaches is not negligible. This is particularly true for Case 1, in which the non-uniformity of the bubble distribution increases the difference between the two methods. In fact, for the considered fuel composition, the effective delayed neutron fraction of the system is as low as 120-150 pcm (Aufiero et al., 2014a). Therefore, even ~12-17 pcm/% differences in the void reactivity coefficient - which are observed in Case 1 at lower void fractions - can have a relevant impact on the system dynamics and, as a consequence, on the reactor operation and control. Concerning computational requirements, the bottleneck in runtime is represented by the solution of the thermal-hydraulics part of the problem. Therefore, the addition of a further equation for the second flux moment (i.e., the adoption of the SP_3 approach) increases the computational time by only 17%. In view of this, and of the improved agreement with Monte Carlo simulations (see Section 3.2), the adoption of an SP_3 transport approximation model can constitute a valuable addition to the multiphysics analysis of the MSFR.

Table 3.10. Absolute and relative difference between the void reactivity coefficient evaluated with the diffusion and SP_3 solvers in Case 1 (calculated bubble distribution).

Avg. void fraction (%)	Absolute difference (pcm/%)	Relative difference (%)
0.288	-16.9	-4.9
0.635	-12.3	-3.9
1.030	-10.5	-3.5
1.468	-9.5	-3.4

Table 3.11. Absolute and relative difference between the void reactivity coefficient evaluated with the diffusion and SP_3 solvers in Case 2 (uniform bubble distribution).

Avg. void fraction (%)	Absolute difference (pcm/%)	Relative difference (%)
0.288	-3.7	-2.3
0.635	-4.4	-2.8
1.030	-4.6	-2.9
1.468	-4.6	-2.9

3.4 Sensitivity analysis to bubbly flow models

Two-fluids thermal-hydraulics models require different closure relations to estimate the momentum and heat exchange between the liquid and the gaseous phases. For a review of these correlations, the reader is referred to (Gidaspow, 1994) and to Appendix B. Additional models are needed to evaluate the bubble diameter, that constitutes an input parameter for many momentum and heat transfer correlations; see, e.g., Eqs. (3.3) and (3.6), in which the bubble Reynolds number Re_b depends on the bubble diameter d_b according to Eq. (3.4). This can be a major limit for Euler-Euler approaches, as an improper modelling of the bubble diameter and of the interphase terms may lead to potentially incorrect results.

In Section 3.3, it is highlighted that the void reactivity feedback of the helium bubbles is strongly dependent on spatial and neutron importance effects and that an accurate evaluation of the bubble spatial distribution is required for a correct estimation of the void coefficient. In this context, a sensitivity analysis to momentum and heat transfer correlations and bubble diameter models is fundamental to assess their impact on reactivity and on the void coefficient in turn. In more detail, the purpose of this section is to verify that (i) the impact of the bubble distribution on the void reactivity feedback is a physical effect, independent from the specific choice of closure relations and (ii) that the multiphysics model is able to correctly evaluate the void coefficient (Tables 3.8 and 3.9). As already discussed in Section 3.3, the following correlations are adopted to model the bubbly flow inside the reactor:

- *Bubble diameter:* isothermal power law described by Eq. (3.5), with $d_0 = 3$ mm at $p_0 = 1$ atm;
- *Drag:* Schiller-Naumann correlation, described by Eq. (3.3);
- *Virtual mass force:* constant coefficient correlation with $C_{VM} = 0.5$;
- *Lift:* neglected;
- *Turbulent dispersion:* neglected;
- *Heat transfer:* Ranz-Marshall correlation, described by Eq. (3.6).

This configuration has been adopted to calculate the multiplication factors and the void coefficients listed in Tables 3.8 and 3.9 (Section 3.3), and is selected as reference case for the present sensitivity analysis. In the remainder of this section, other models and correlations are selected to assess their impact on results. It is underlined that one model at a time is tested, keeping the correlations for all the other terms unchanged.

3.4.1 Sensitivity to the bubble diameter

The choice of the bubble diameter d_b is crucial in Euler-Euler approaches, since it determines the bubble Reynolds number Re_b, which in turn appears in many correlations describing interphase momentum and heat transfer. In the light of this, a

sensitivity analysis is carried out on the bubble diameter, to evaluate its effect on reactivity and on the void coefficient. To this aim, two different models are considered:

- An isothermal power law, in which the bubble diameter d_b only depends on pressure p via Eq. (3.5). The results shown in Tables 3.8 and 3.9 have been obtained by choosing $d_0 = 3\,mm$ (based on the assumption that this is the diameter of the bubble injector, even if the design of the helium bubbling system is yet to be defined) and $p_0 = 1\,atm$ (which is the operating pressure of the MSFR).

- An interface area transport equation (IATE) that, given the size (i.e., the diameter) of the bubble injector as a boundary condition, evaluates the liquid-gas interface area and the bubble diameter in turn (Ishii et al., 2005). The main advantage of this approach is that the injector diameter is a design feature of the system and not an arbitrarily guessed parameter such as d_0. Therefore, if the design of the injector system is known, the bubble diameter can be calculated all over the domain via a partial differential equation. Details on this model are provided in Appendix B.

To perform the sensitivity analysis, the void reactivity coefficient is evaluated in four different cases, changing every time the bubble diameter model:

- Isothermal power law with $d_0 = 1\,mm$ and $p_0 = 1\,atm$;

- *Reference case:* Isothermal power law with $d_0 = 3\,mm$ and $p_0 = 1\,atm$;

- Isothermal power law with $d_0 = 5\,mm$ and $p_0 = 1\,atm$;

- IATE model (Ishii et al., 2005) with a 3 mm diameter injector.

For the sake of simplicity, the multi-group neutron diffusion model is selected to carry out these calculations. Results are plotted in Figure 3.8, also reporting the "uniform bubble distribution" case of Table 3.8 for comparison.

The void coefficient shows the same behaviour in all the four considered cases. A particularly good agreement is observed over the whole investigated void fraction range between the isothermal model with $d_0 = 3\,mm$ and the IATE model with a 3 mm diameter injector. This points out that choosing d_0 according to the injector size (as done to obtain the results of Tables 3.8 and 3.9) is a good assumption to evaluate the bubble diameter. In more detail, even at high void fractions, the void coefficient difference between the two cases is always below 5 pcm/%. This discrepancy is lower than (i) the differences between the "calculated" and "uniform" distribution approaches (Table 3.8) and (ii) the differences pointed out between the diffusion and the SP_3 neutronics models, when the calculated bubble distribution is taken into account (Table 3.10). In particular, the 5 pcm/% discrepancy is between 3% and 5% of the effective delayed neutron fraction (120-150 pcm) and is not expected to have a significant impact on the system dynamics.

All the curves are almost coincident at lower void fractions while a slight discrepancy is observed at higher void fractions. Choosing as reference the isothermal model with $d_0 = 3\ mm$ (used to obtain the results of Tables 3.8 and 3.9 and later on in this work), the relative differences with the other cases are always below 5.1% at a core-average void fraction of 1.4% (see Table 3.12). These results suggest that the proposed multiphysics model is solid and consistent as far as the bubble diameter is concerned, since its predictions are not significantly modified by the choice of this parameter.

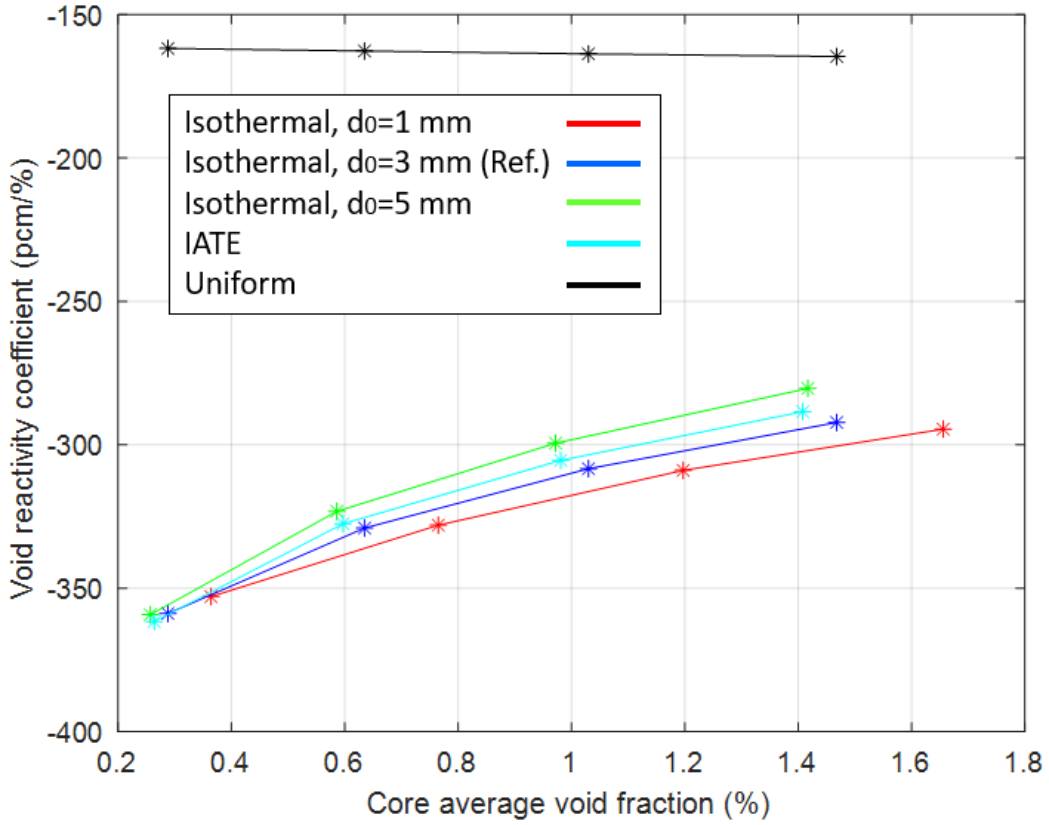

Figure 3.8. Void coefficient vs. core-average void fraction for different bubble diameter models. The "uniform bubble distribution" case is reported for comparison.

Table 3.12. Relative difference among the void fraction coefficients evaluated with different bubble diameter models for a core-average void fraction of 1.4%.

Bubble diameter model	Relative difference
Isothermal, $d_0 = 3\ mm$ and $p_0 = 1\ atm$ *(Reference)*	-
Isothermal, $d_0 = 1\ mm$ and $p_0 = 1\ atm$	2.4%
Isothermal, $d_0 = 5\ mm$ and $p_0 = 1\ atm$	-5.1%
IATE, 3 mm diameter injector	-2.4%
Uniform case	-44.1%

3.4.2 Sensitivity to momentum transfer models

In this subsection, different correlations for drag, virtual mass forces, lift and turbulent dispersion are compared, highlighting their impact on the void coefficient.

3.4.2.1 Sensitivity to drag models

Drag forces are due to viscosity effects between the continuous and the dispersed phases. In this work, the following correlations are compared to evaluate the drag contribution to the interphase momentum transfer:

- *Reference case:* Schiller-Naumann (Schiller and Naumann, 1933; Rusche, 2002);
- Gidaspow-Schiller-Naumann (Enwald et al., 1996);
- Gidaspow-Ergun-Wen-Yu (Gidaspow, 1994);
- Ishii-Zuber (Ishii and Zuber, 1979).

The impact of these correlations on the void reactivity coefficient is illustrated in Figure 3.9.

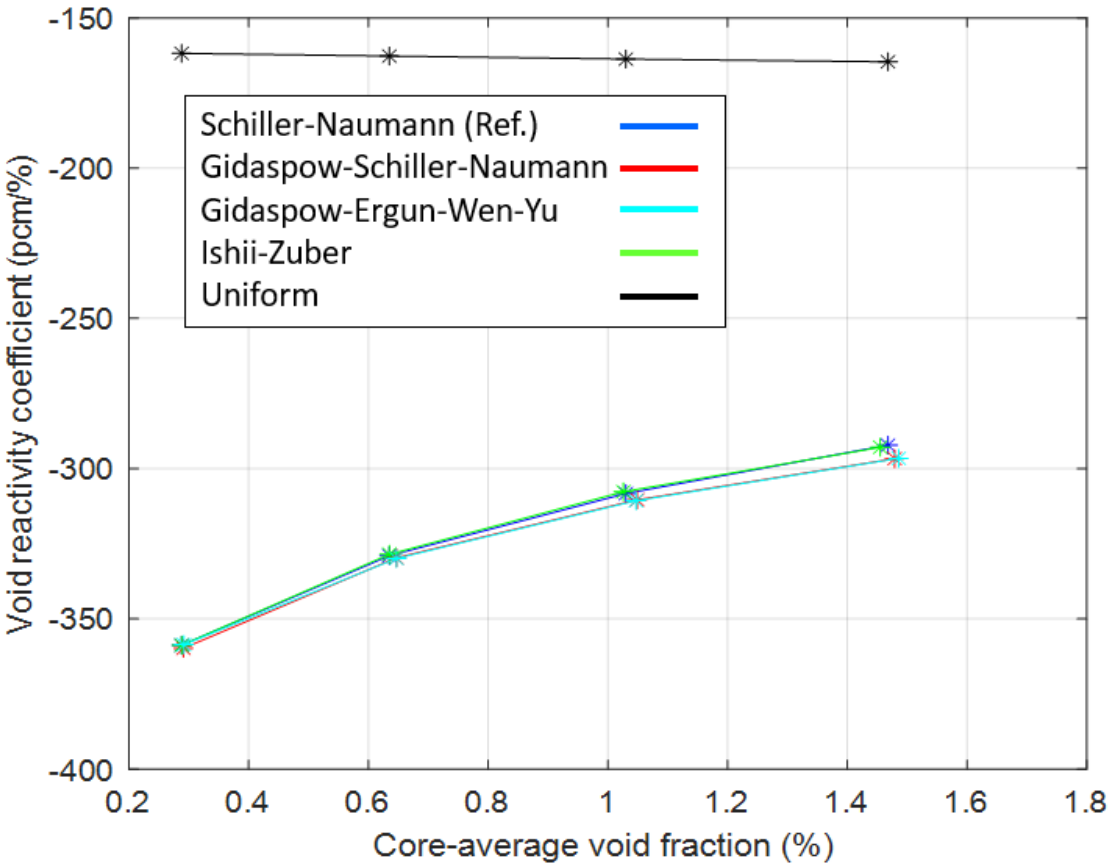

Figure 3.9. Void coefficient vs. core-average void fraction for different drag models. The "uniform bubble distribution" case is reported for comparison.

3.4.2.2 Sensitivity to virtual mass force models

Virtual mass forces are due to the inertia of the carrier fluid and originate from the relative acceleration of the two phases. In this work, the following models are compared to evaluate the virtual mass contribution to the interphase momentum transfer:

- *Reference case:* constant coefficient correlation with $C_{vm} = 0.5$ (Rusche, 2002), which is the limit for high Reynolds numbers (Kendoush et al., 2007);
- Lamb (Lamb, 1895);
- No virtual mass forces.

The impact of these correlations on the void reactivity coefficient is illustrated in Figure 3.10.

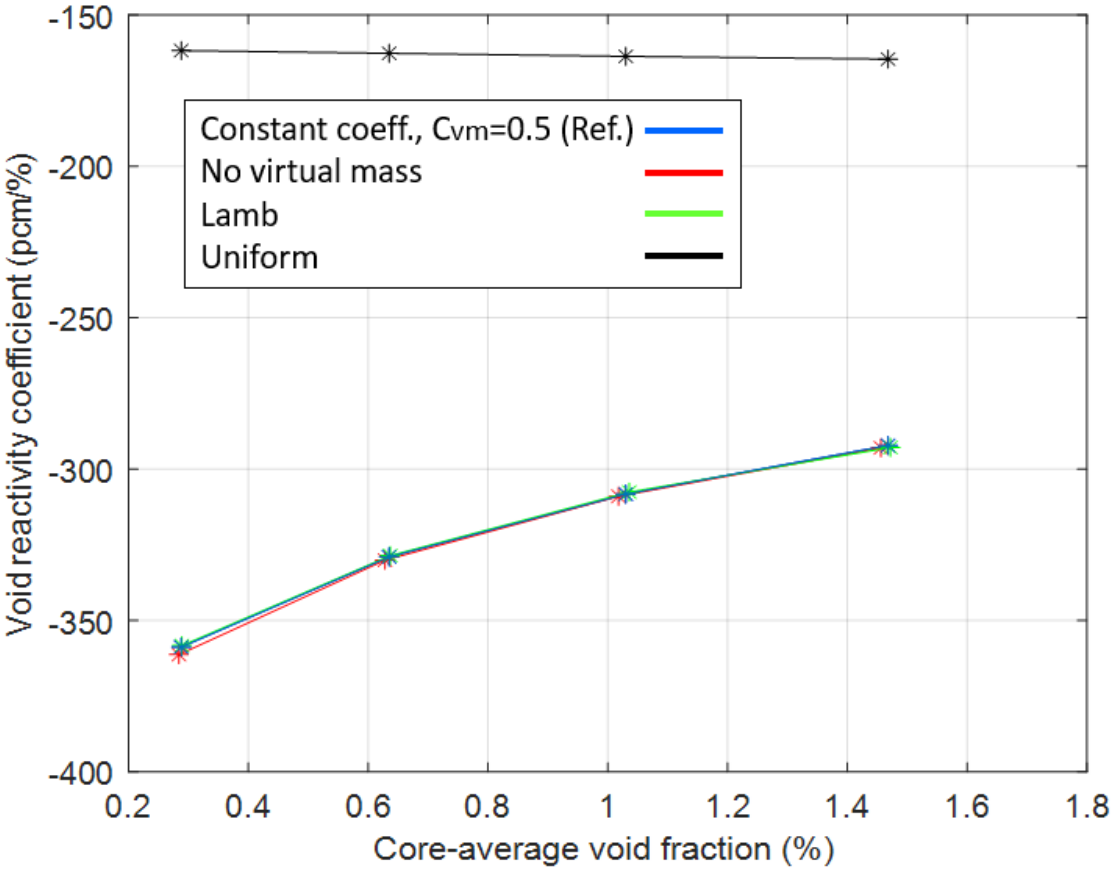

Figure 3.10. Void coefficient vs. core-average void fraction for different virtual mass force models. The "uniform bubble distribution" case is reported for comparison.

3.4.2.3 Sensitivity to lift models

Lift results from the rotational part of the fluid motion (i.e., from vorticity). In this work, the following models are compared to evaluate the lift contribution to interphase momentum transfer:

- *Reference case:* no lift;
- Constant coefficient correlation with $C_l = 0.5$, which is the limit for high Reynolds numbers (VDI Heat Atlas, 2010);
- Tomiyama (Tomiyama et al., 2002);
- Legendre-Magnaudet (Legendre and Magnaudet, 1998).

The impact of these correlations on the void reactivity coefficient is illustrated in Figure 3.11.

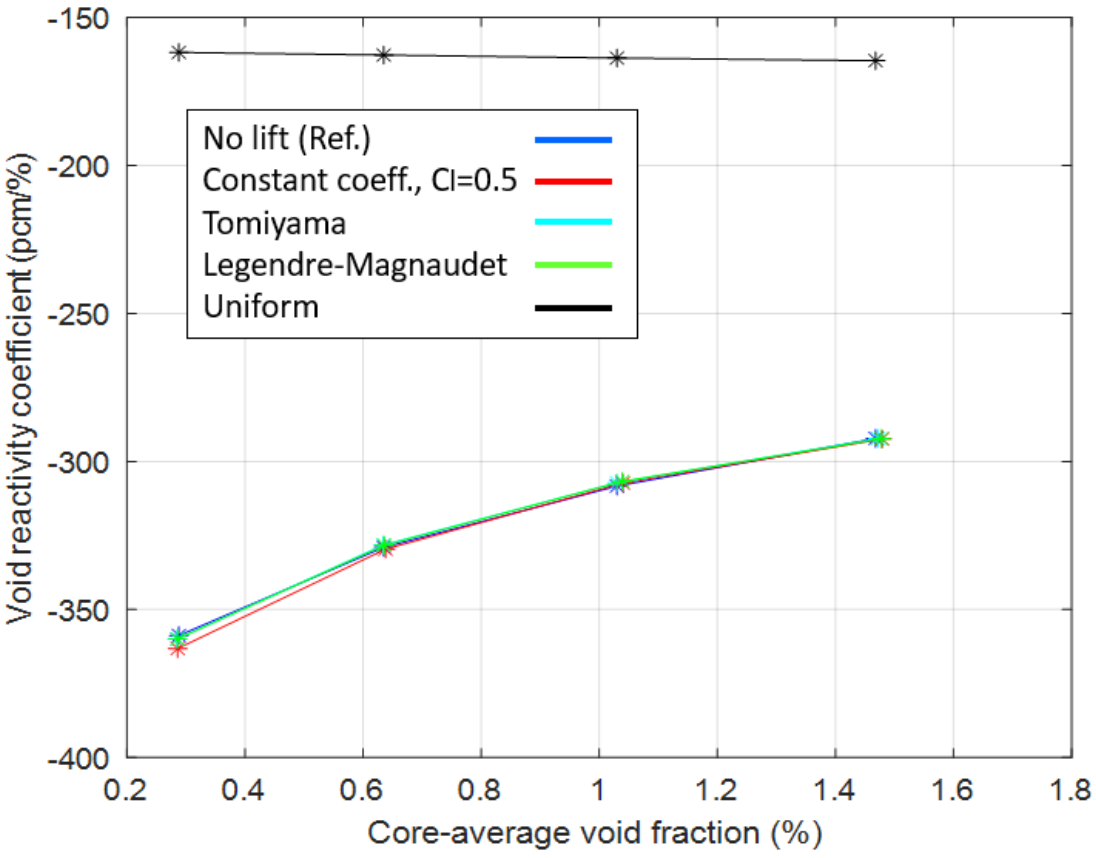

Figure 3.11. Void coefficient vs. core-average void fraction for different lift models. The "uniform bubble distribution" case is reported for comparison.

3.4.2.4 Sensitivity to turbulent dispersion models

Turbulent dispersion is an additional drag component due to turbulent fluctuations in the dispersed phase. In this work, the following models are compared to evaluate the turbulent dispersion contribution to interphase momentum transfer:

- *Reference case:* no turbulent dispersion;
- Burns (Burns et al., 2004);
- Gosman (Gosman et al., 1992).

The impact of these correlations on the void reactivity coefficient is illustrated in Figure 3.12.

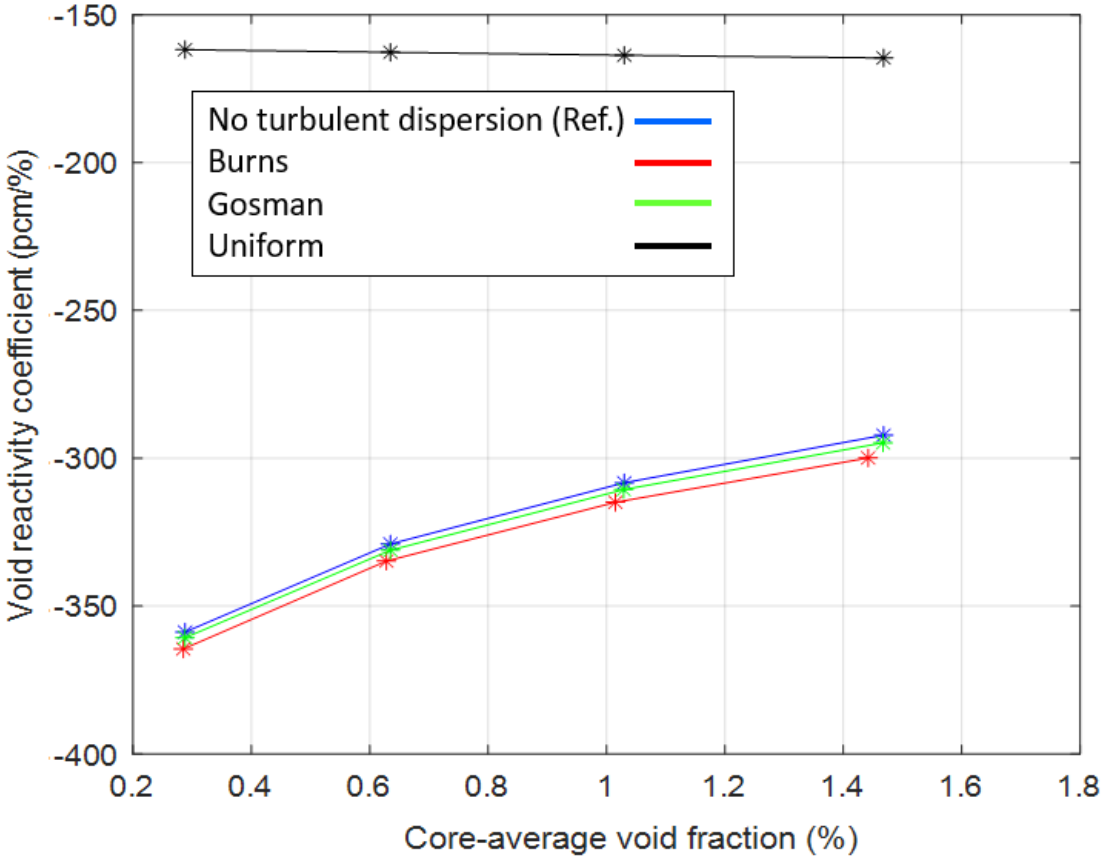

Figure 3.12. Void coefficient vs. core-average void fraction for different turbulent dispersion models. The "uniform bubble distribution" case is reported for comparison.

3.4.2.5 Discussion of results

Void coefficient discrepancies among different momentum transfer correlations are even lower to those observed in the bubble diameter sensitivity analysis. The maximum relative discrepancy (2.7 %) is observed when the Burns model is adopted instead of neglecting turbulent dispersion (only at higher void fractions). In all the other cases, relative differences are always below 1.4 %. This points out that the choice of different momentum transfer correlations has a negligible impact on the void reactivity coefficient. In addition, it can be observed that the void fraction is weakly affected by different closure relations, with the largest effect being exerted by the bubble diameter model (similar results have been observed on the bubble distribution as well). Other important quantities (e.g., fuel temperature, flow rate and precursor distributions) are virtually unaffected by the choice of these correlations.

3.4.3 Sensitivity to heat transfer models

To evaluate the impact of the inter-phase heat transfer correlations, the two models implemented in the *twoPhaseEulerFoam* solver are compared:

- *Reference case:* Ranz-Marshall (Ranz and Marshall, 1952);
- Analytical solution for a spherical bubble.

As shown in Figure 3.13, the two correlations yield virtually identical results, as the corresponding curves are perfectly coincident.

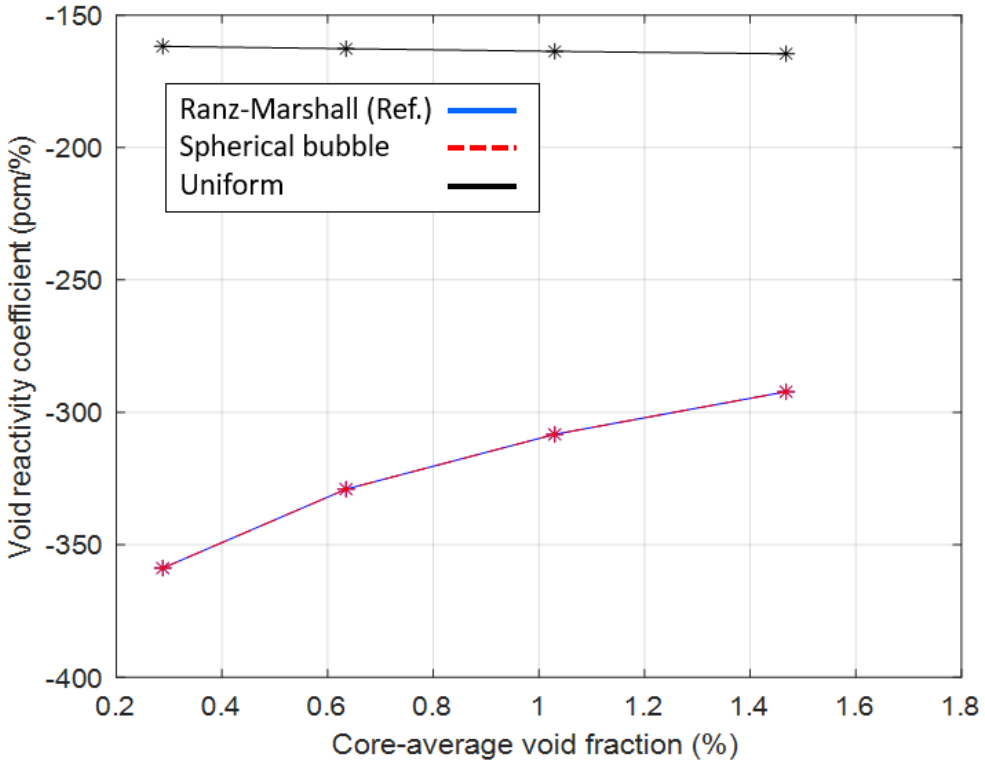

Figure 3.13. Void coefficient vs. core-average void fraction for different heat transfer models. The "uniform bubble distribution" case is reported for comparison.

3.4.4 Sensitivity to turbulence models

A detailed comparison of turbulence models in not in the scope of the present work. In fact, bubble diameter, momentum and heat transfer closure relations are a typical feature of two-fluids approaches. Consequently, a sensitivity analysis to these correlations is necessary to assess the reliability of the Euler-Euler method and its suitability to the analysis of the MSFR helium bubbling system. On the other hand, turbulence modelling is a general problem of CFD, not specific to the Euler-Euler simulation of bubbly flows. Nevertheless, for completeness, the following turbulence models are compared:

- *Reference case:* Lahey k-ε model (Lahey, 2005);
- Wilcox k-ω model (Wilcox, 2008).

As shown in Figure 3.14, changing turbulence model does not affect the behaviour of the void reactivity coefficient. In more detail, the maximum relative difference among the predicted void coefficients is 2.4 %, which is not expected to significantly affect the system dynamics and controllability.

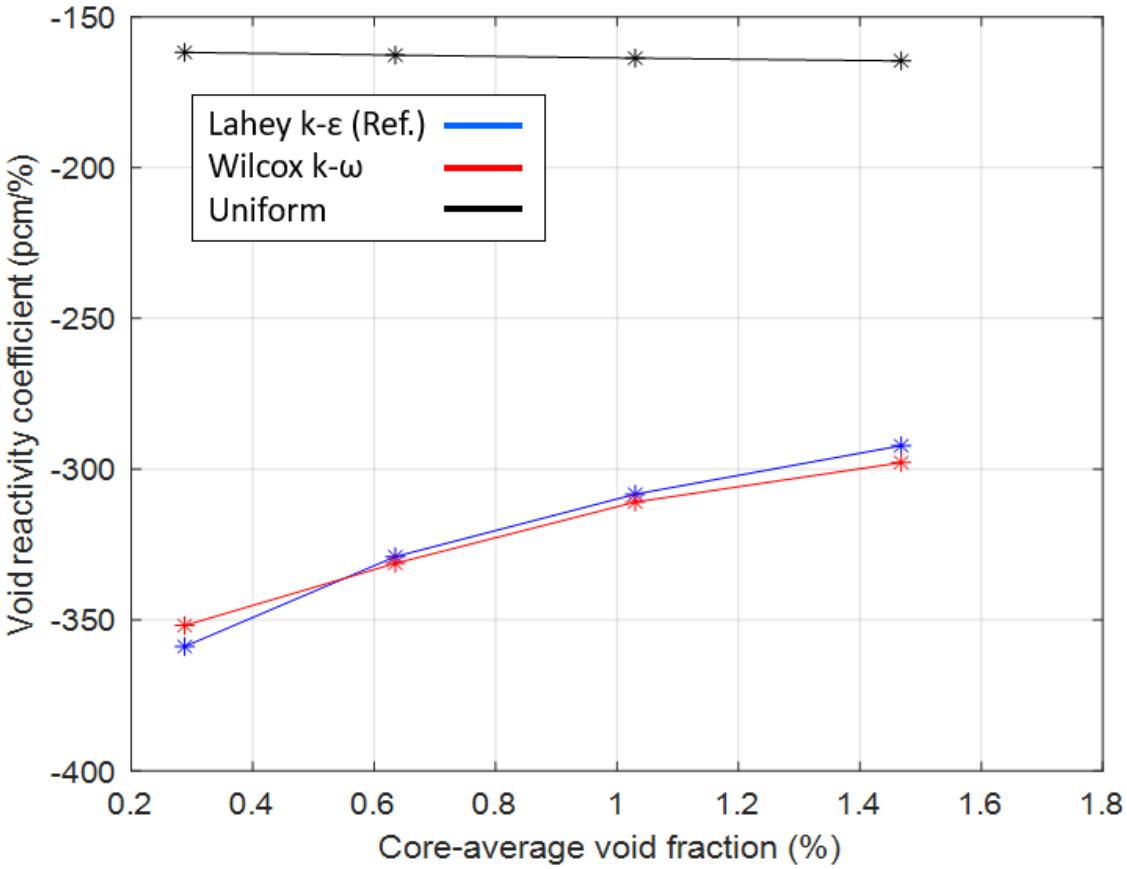

Figure 3.14. Void coefficient vs. core-average void fraction for different turbulence models. The "uniform bubble distribution" case is reported for comparison.

3.5 Concluding remarks

The content of this chapter can be summarized as follows:

1. The diffusion and the SP_3 neutronics models are verified against a Monte Carlo model of the MSFR. Typically, Monte Carlo simulations are carried out using a uniform temperature and density for each material. In addition, standard Monte Carlo codes cannot handle the precursor motion in the circulating fuel, since they were originally developed for solid-fuelled reactors. On the other hand, the OpenFOAM model calculates non-uniform temperature, density and void fraction fields and is able to simulate the precursor dragging by the liquid fuel mixture. These differences may complicate a direct comparison between the two methods. To overcome this issue, static fuel and uniform temperature, density and void fraction distributions are also assumed in the OpenFOAM model. As compared to multi-group diffusion, the SP_3 model yields visible improvements in the prediction of the multiplication factor and of the void reactivity coefficient, even if both the models show in general a good agreement with the Monte Carlo results.

2. The multiphysics model is applied to a simplified 2D geometry of the MSFR. The void reactivity coefficient is estimated on the basis of the bubble spatial distribution calculated by the two-phase solver. Important differences are highlighted with respect to simulations carried out with uniform bubble distributions (which is the typical approach adopted by state-of-the-art single-phase models). These results point out that the void reactivity effect is strongly dependent on spatial as well as neutron importance effects. In more detail, when the calculated bubble distribution is taken into account, the void coefficient is significantly higher as compared to "uniform distribution" approaches. In this regard, standard single-phase models are strongly non-conservative. Indeed, if the bubble concentration inside the reactor decreases (such as in the case of a failure of the bubble injectors), these models would underestimate the resulting positive reactivity insertion. This limitation is particularly relevant in the light of the high value of the void coefficient (280-360 pcm/%, as compared to an effective delayed neutron fraction of 120-150 pcm), raising concerns about super-prompt-critical reactivity insertions and on the employment of helium bubbling for reactivity control purposes. This issue could be mitigated by adopting more injection systems (leading to a more uniform bubble distribution) instead of only one per external circuit, at the expense of having more perforations in the reactor vessel.

3. Differences are also highlighted between the diffusion and the SP_3 approaches (especially at low void fractions and when the calculated bubble distribution is considered), which may have a non-negligible impact on the system dynamics and controllability. In this regard, the adoption of a more detailed neutronics model is particularly important when non-uniform bubble distributions are involved, which is the case in the MSFR.

4. A sensitivity analysis is carried out to compare different bubble diameter models, interphase momentum and heat transfer correlations, and turbulence models as well. Results point out that the void reactivity coefficient is not strongly dependent on the choice of these correlations. In more detail, the pressure gradient and the drag force are the only important force terms in the momentum equation, while virtual mass forces, lift and turbulent dispersion may be neglected without leading to significant changes in the simulations. Therefore, the proposed multiphysics model is consistent and reliable as far as the prediction of reactivity and of the void coefficient is concerned.

As compared to available literature, this is the only analysis of the MSFR helium bubbling system carried out by coupling neutron diffusion and transport models with a two-phase fluid-dynamics model, capable of handling the non-uniform bubble distribution inside the reactor. Allowing for a more detailed description of the bubble motion through the reactor, the proposed multiphysics tool can be an important starting point for future optimizations of the helium bubbling system and to develop appropriate control strategies. Moreover, even if alternative reactivity control systems will be preferred to helium bubbling, accurate two-phase fluid-dynamics models would still be required to evaluate the impact on reactivity of gaseous fission products and to optimize their removal from the fuel mixture.

Chapter 4

Three-dimensional analysis of the MSFR

Abstract

In this chapter, the reactivity effect induced by the helium bubbles is studied taking into account the actual three-dimensional geometry of the MSFR. This analysis is carried out by comparing a neutron diffusion, an SP_3 neutron transport and a Monte Carlo model. Since the distribution of the bubbles is not uniform in the reactor but strongly depends on the location of their injection and extraction, as well as on the velocity field of the liquid fuel, a coupling scheme between OpenFOAM and the Monte Carlo code Serpent 2 is adopted for the Monte Carlo analysis. In this way, Serpent 2 is provided with the non-uniform bubble distribution calculated by the OpenFOAM two-phase thermal-hydraulics solver. The aim of this analysis is to highlight the difference arising when a uniform and a calculated bubble distribution are considered in the Monte Carlo model as well as the difference among the three approaches herein adopted. The present study is also a verification test for the ability of the multiphysics solver to handle a large, three-dimensional unstructured mesh, pointing out eventual differences with respect to the 2D analysis carried out in Chapter 3. The outcome of this analysis confirms that the void reactivity feedback is strongly influenced by the bubble distribution. Good agreement is also obtained among the neutron diffusion, the SP_3 neutron transport and the Monte Carlo solutions.

The content of this chapter is based on:

Cervi, E., Lorenzi, S., Luzzi, L., Cammi, A., 2018b. Analysis of the void reactivity effect in the Molten Salt Fast Reactor: impact of the helium bubbling system, PHYTRA4 Fourth International Conference on Physics and Technology of Reactors and Applications, Marrakech, Morocco, September 17-19, 2018.

Cervi, E., Lorenzi, S., Luzzi, L., Cammi, A., 2019c. Multiphysics analysis of the MSFR helium bubbling system: a comparison between neutron diffusion, SP_3 transport and Monte Carlo approaches, Annals of Nuclear Energy 132, 227-235.

4.1 Introduction

Neutron diffusion is typically selected for the estimation of the neutron flux in available multiphysics models of the MSFR (Fiorina et al., 2013; Aufiero et al., 2014a; 2014b; Fiorina et al., 2014). However, the adoption of more accurate neutronics models, based on transport theory, may constitute an improvement for the analysis of the MSFR, allowing for catching phenomena that cannot be described by means of diffusion approaches. It is well known that diffusion theory has some limits, especially when it comes to predicting the neutron behaviour in heterogeneous systems (Stacey, 2007). Hence, the neutronics analysis of the MSFR can benefit from the adoption of a neutron transport model, especially when non-homogeneous bubble distributions are involved. In this regard, the SP_3 approximation of the neutron transport equation (Brantley and Larsen, 2000) represents an improvement, as compared to diffusion theory, in the analysis of the MSFR helium bubbling system. At the same time, this approach is characterized by lower computational requirements as compared to more accurate neutronics models (e.g., S_N or integral approaches), being therefore suitable for complex multiphysics analyses, such as the 3D simulation of the MSFR. On the other hand, the continuous energy Monte Carlo approach is not affected by the modelling assumptions typical of neutron diffusion and SP_N theories and by the group-discretization of neutron energy. At the same time, as compared to fully deterministic, multiphysics approaches, standard Monte Carlo codes do not have the capability of simulating the precursor dragging in the liquid fuel mixture.

The neutron diffusion and the SP_3 neutron transport models developed in this thesis have been tested against Monte Carlo simulations in Chapter 3. However, simplifying hypotheses (i.e., the adoption of uniform temperature, density and void fraction fields and the assumption of static fuel) were made to allow a direct comparison between the multiphysics model and the Monte Carlo results. Aiming at relaxing these simplifications, a coupling scheme is adopted between OpenFOAM and the Monte Carlo code Serpent 2. In more detail, the non-uniform temperature, density and bubble distributions calculated with a 3D OpenFOAM model of the MSFR are exported to a 3D Monte Carlo model of the same geometry, using a built-in multiphysics interface featured by the Serpent 2 code (Tuominen et al., 2016).

4.2 Three-dimensional analysis of the MSFR helium bubbling system

As shown in Chapter 3, the presence of the bubbly flow causes a negative reactivity insertion into the system due to the negative void coefficient of the bubbles. A preliminary evaluation of this contribution can be made considering a uniform void fraction (Brovchenko et al., 2013). On the other hand, the real distribution of the bubbly flow inside the reactor is not uniform since the bubbles are dragged by the fluid flow. Consequently, the void reactivity coefficient, expressed by Eq. (3.2), needs to be calculated accounting for the spatial and importance dependence of the bubble void feedback.

The deterministic (diffusion and SP_3) simulations are carried out with the multiphysics OpenFOAM model proposed in this thesis. Thanks to the coupling between neutronics and two-phase thermal-hydraulics, this model is suitable to study the mentioned aspect of the void reactivity feedback. On the other hand, the Monte Carlo simulations are carried out using the continuous energy Monte Carlo code Serpent 2 (Leppänen et al., 2015), importing the bubble spatial distribution from the multiphysics OpenFOAM model.

4.2.1 Deterministic approach

The present analysis is carried out on a quarter of the MSFR full core (Figure 4.1). In this work, 650°C and 750°C are taken as inlet and outlet temperature of the fuel salt, respectively, and a full-core thermal power of 3000 MW_{th} is assumed to normalize the neutron flux. Different helium flow rates are injected at the bottom of the reactor and all the gas is removed in the external circuit. The design specifications of the gas injection and extraction systems are still to be defined and their optimization is out of the scope of the present work. Therefore, helium injection and extraction are simply modelled by means of mass source/sink terms in the continuity equation. Similarly, the primary pumps are simulated by means of momentum sources, uniformly distributed in the heat exchanger regions. Albedo boundary conditions are adopted at the reactor walls, while symmetry is imposed at the cutting planes (i.e., it is assumed that neutronics and thermal-hydraulics conditions are identical in any reactor quarter). The mesh, shown in Figure 4.1, has 1,954,024 cells, ensuring that results are not modified by further refinements. The maximum and average non-orthogonality are 65.03 and 11.11 degrees, respectively.

As in Chapter 3, no-slip boundary conditions are imposed at the reactor walls, while the pumps and the heat exchangers are modelled as momentum sources and heat sinks, respectively. The bubble diameter is evaluated with Eq. (3.5), with $d_0 = 3$ mm and $p_0 = 1$ atm. In addition, drag is modelled with the Schiller-Naumann correlation, virtual mass forces with a constant coefficient correlation with $C_{vm} = 0.5$ (Rusche, 2002), lift and turbulent dispersion are neglected while the heat transfer between the fuel and the bubbles is evaluated with the Ranz-Marshall correlation (Ranz and Marshall, 1952). The Lahey k-ε turbulence model (Lahey, 2005) is adopted to account for the effect of the dispersed phase on eddy viscosity.

The multiplication factor is estimated at different core average void fractions with the power iteration routine implemented into the solver, assuming both a uniform bubble distribution as well as the bubble distribution calculated by the multiphysics solver. Six-group constants are generated with Serpent 2, selecting the JEFF-3.1.1 library (Santamarina et al., 2009) for cross section data and using 100 million neutron histories (10^5 neutrons for 1000 cycles), obtaining a 5 pcm uncertainty on the multiplication factor. The energy group subdivision is the same adopted in Chapter 3 and is reported in Table 3.1. Albedo boundary conditions are adopted at the solid blanket and reflectors. The albedo coefficients are calculated with Serpent and are listed in Table 4.1 as $\gamma_i = -0.5 \cdot (1 - \alpha_i)/(1 + \alpha_i)$ (see Eq. 2.20). Note that the minus signs in the lower-energy group indicate that the incoming neutron current is higher than the outgoing one, due to the thermalization of faster neutrons. The Serpent model of the MSFR used for cross section generation is presented in Section 4.2.2. For details on precursor properties, the reader is referred to Appendix C.

Table 4.1. Albedo coefficients γ_i adopted at the reflectors and fertile blanket.

Energy group	Reflectors	Blanket
1	0.372982	0.388957
2	0.147661	0.222056
3	0.062728	0.097192
4	0.081202	0.068321
5	0.010140	0.041276
6	-0.071469	-0.022696

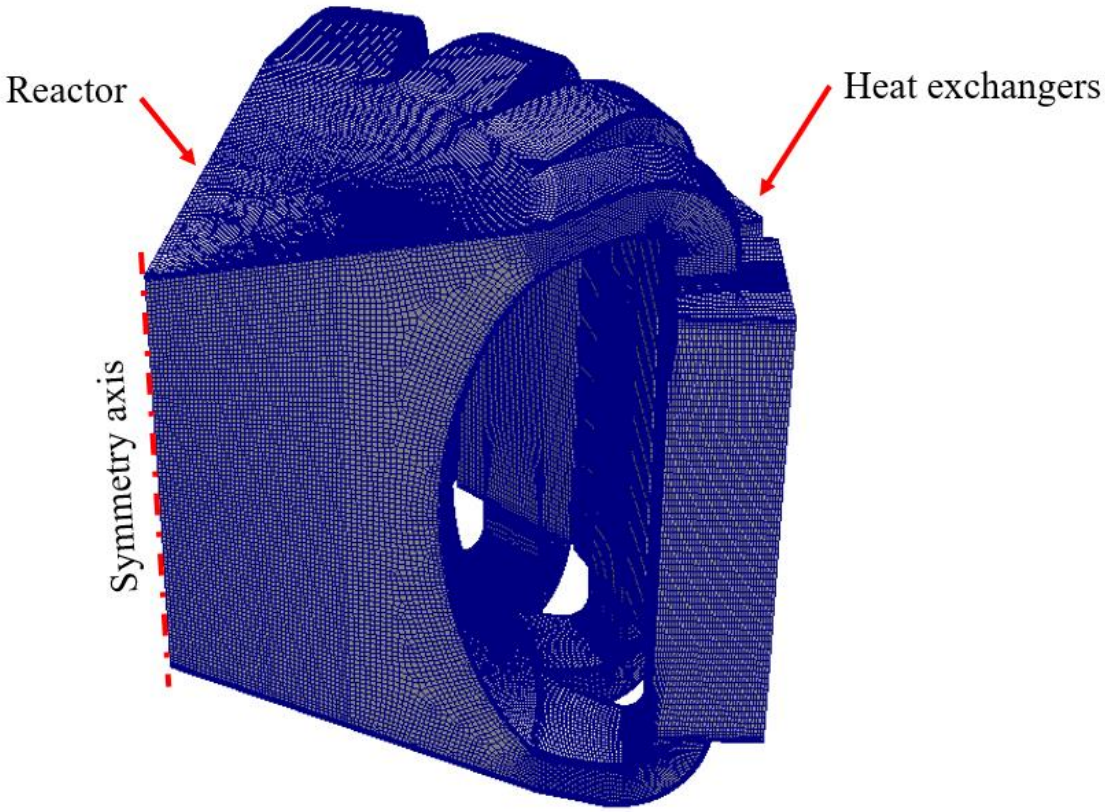

Figure 4.1. 3D OpenFOAM mesh of a quarter of the MSFR full core.

The values of the multiplication factor and of the void reactivity feedback coefficient obtained with the diffusion and the SP_3 approaches are listed in Tables 4.2 and 4.3, respectively. The core average void fractions listed in the first column are evaluated at steady state for different bubble injection rates, i.e., 0, 3.6, 7.2 and 10.8 g/s, respectively. Simulations are carried out in about 20 hours with 36 MPI parallel threads, using an Intel Xeon 8160 CPU with 2 x 18 cores and a clock speed of 2.10 MHz.

Table 4.2. Diffusion approach: multiplication factor and void reactivity coefficient with calculated and uniform bubble distribution.

Core-average void fraction (%)	Multiplication factor		Void coefficient (pcm/%)	
	Calculated bubble distribution	*Uniform bubble distribution*	*Calculated bubble distribution*	*Uniform bubble distribution*
0	0.96503	0.96503	-	-
0.437	0.96364	0.96429	-342.0	-182.0
0.876	0.96227	0.96354	-339.3	-182.9
1.308	0.96097	0.96279	-334.7	-184.3

Table 4.3. SP_3 approach: multiplication factor and void reactivity coefficient with calculated and uniform bubble distribution.

Core-average void fraction (%)	Multiplication factor		Void coefficient (pcm/%)	
	Calculated bubble distribution	*Uniform bubble distribution*	*Calculated bubble distribution*	*Uniform bubble distribution*
0	0.96581	0.96581	-	-
0.437	0.96444	0.96511	-336.6	-171.8
0.876	0.96308	0.96434	-335.0	-180.2
1.308	0.96179	0.96360	-330.9	-181.5

Figures 4.2 and 4.3 represent the temperature and the sixth group flux distributions in the three-dimensional geometry, obtained using the SP_3 solver for neutronics. In addition, Figures 4.4 and 4.5 show the bubble and the power density distributions at 1.308% core-average void fraction. It can be observed that, in correspondence of the bubbly flow paths, the power density decreases, due the void feedback on the fission rate.

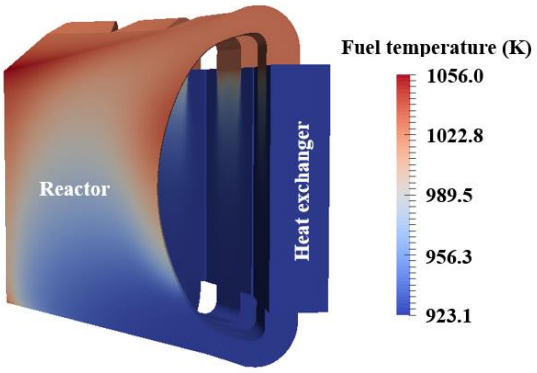

Figure 4.2. Fuel temperature distribution.

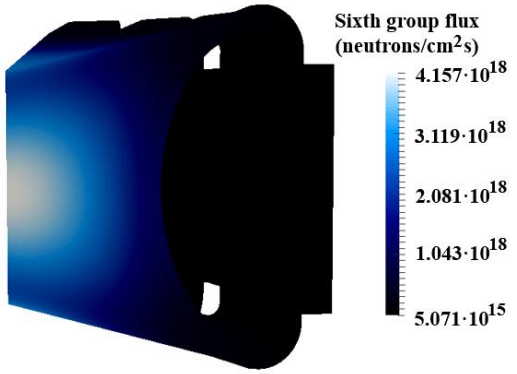

Figure 4.3. Sixth group flux distribution.

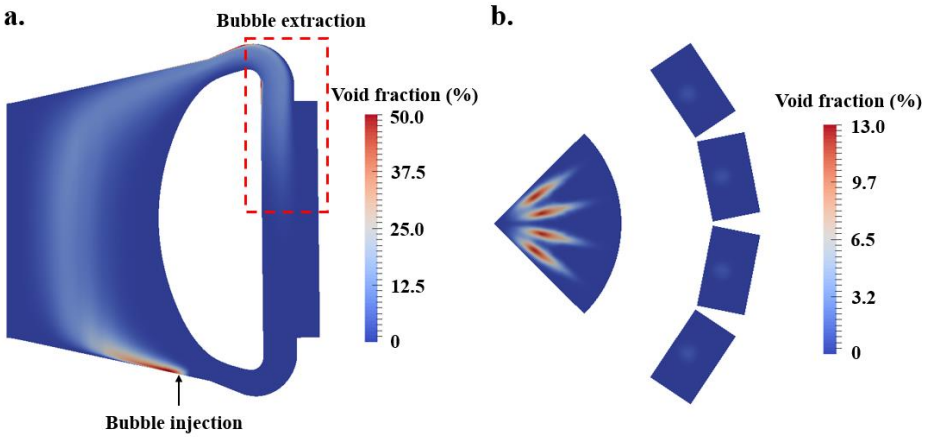

Figure 4.4. Void fraction distribution at 1.308% core average void fraction. Vertical (a) and horizontal (b) sections.

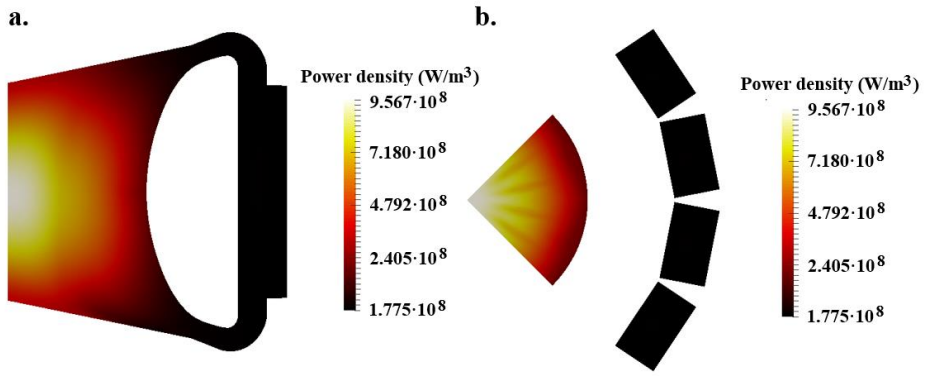

Figure 4.5. Power density distribution at 1.308% core average void fraction, obtained with the SP_3 approach. Vertical (a) and horizontal (b) sections.

4.2.2 Monte Carlo approach

The void coefficient due to the bubbles is usually calculated through Monte Carlo approach considering a uniform bubble distribution, i.e., calculating a density-based effect (Brovchenko et al., 2013). On the other hand, as shown in the previous section (as well as in Chapter 3 using a 2D geometry), the spatial distribution of the bubbles can be very different from the uniform case. To this aim, for assessing the void reactivity coefficient in the MSFR, the bubble spatial distribution calculated with the two-phase Euler-Euler solver is exported into a Serpent model of the MSFR (Figure 4.6) through a built-in multiphysics interface with OpenFOAM (Tuominen et al., 2016). Unlike the deterministic model, in which albedo boundary conditions are used at the reactor walls, the radial fertile blanket and the top and bottom reflectors are considered here. As discussed above, the present calculations are carried out using 100 million neutron histories, obtaining a 5 pcm 1-σ uncertainty on the multiplication factor. As in the previous section, simulations are carried out (i) assuming a uniform bubble distribution and (ii) importing the non-homogeneous bubble distribution calculated by the OpenFOAM solver. The values of the multiplication factor and of the void reactivity feedback coefficient obtained with the Monte Carlo approach are listed in Table 4.4. In addition, Figure 4.7 shows the normalized fission rate distribution in the MSFR evaluated by Serpent.

Table 4.4. Monte Carlo approach: multiplication factor and void reactivity coefficient (± 1-σ uncertainty) with uniform and calculated bubble distribution.

Average void fraction (%)	Multiplication factor		Void coefficient (pcm/%)	
	Calculated bubble distr.	*Uniform bubble distr.*	*Calculated bubble distr.*	*Uniform bubble distr.*
0	0.97110 ± 0.00005	0.97110 ± 0.00005	-	-
0.437	0.96980 ± 0.00005	0.97042 ± 0.00005	-315.9 ± 17.2	-165.1 ± 17.2
0.876	0.96855 ± 0.00005	0.96970 ± 0.00005	-309.5 ± 8.6	-169.7 ± 8.6
1.308	0.96731 ± 0.00005	0.96904 ± 0.00005	-308.5 ± 5.8	-167.4 ± 5.8

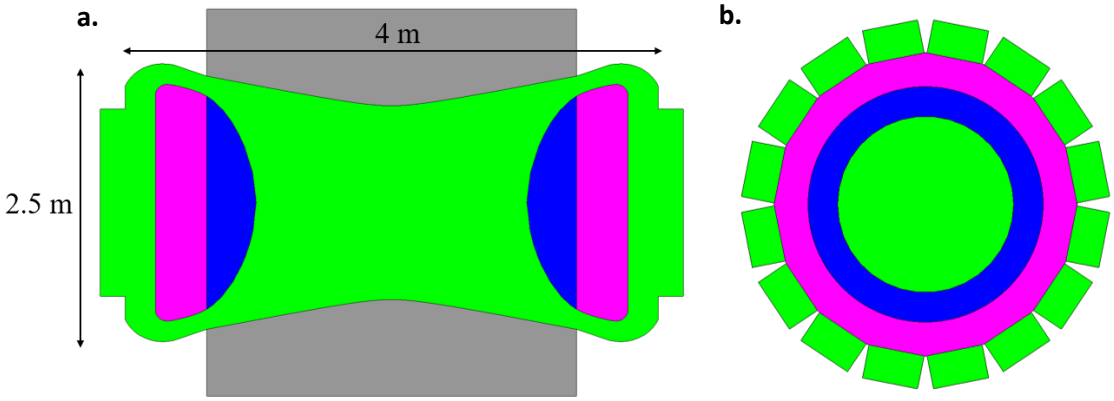

Figure 4.6. Vertical (a) and horizontal (b) sections of the Serpent model. In green, the liquid fuel (reactor and external circuits), in blue the fertile blanket, in grey the reflectors and in purple the boron carbide shield.

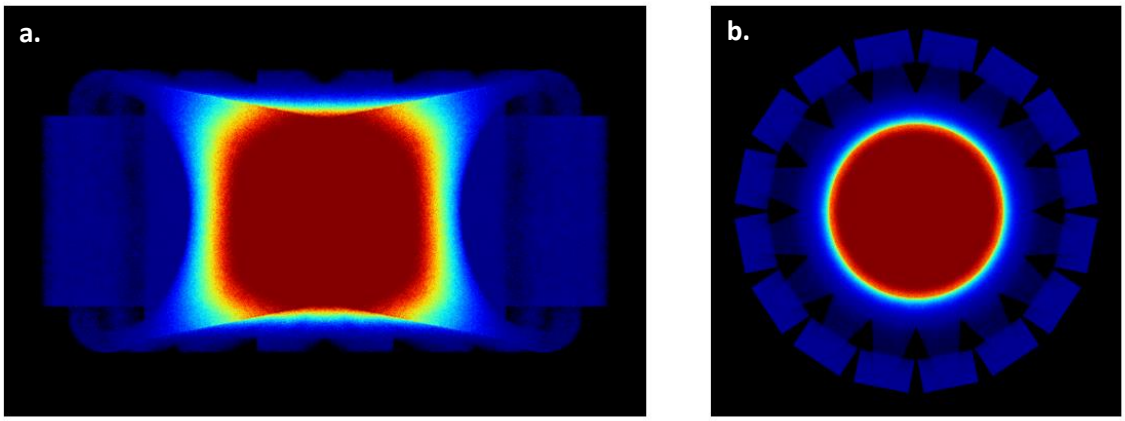

Figure 4.7. Normalized fission rate distribution in arbitrary units (black=0, red=1) at 1.308% core average void fraction (real bubble distribution). Vertical (a) and horizontal (b) sections.

4.2.3. Discussion of results

As in Chapter 3, significant differences are pointed out between the calculated and uniform distribution approaches, pointing out that the void reactivity feedback of the bubbles is strongly dominated by spatial and neutron importance effects. This physical effect can only be described by means of an accurate thermal-hydraulics solver, suitable to handle the presence of bubbles inside the reactor and to reproduce their spatial distribution. In general, good agreement is shown among the diffusion, the SP_3 and the Monte Carlo results. The multiplication factor difference among the three approaches is shown in Tables 4.5 and 4.6.

The agreement among the three approaches is fairly good, also considering the large scale of the system and the complex multiphysics coupling between neutronics and two-phase thermal-hydraulics. In general, as compared to Monte Carlo, the SP_3 and the diffusion solvers underestimate the multiplication factor. This result can be explained by considering that in the deterministic model: (i) the domain is limited to the fuel circuit without considering reflectors and fertile blanket zones (which are accounted for by means of albedo boundary conditions), and (ii) the precursor motion through the reactor is considered leading to a reduction of reactivity. Indeed, in the deterministic model, part of the precursors decay outside the active zone without contributing to fissions (as a guideline, multiphysics simulations carried out with and without precursor dragging pointed out a reactivity increase of about 190 pcm in the latter case).

Table 4.5. Multiplication factor difference between the diffusion and the Monte Carlo approaches.

Core average void fraction (%)	$k_{eff,diff} - k_{eff,MC}$ (pcm)	
	Uniform bubble distribution	*Real bubble distribution*
0	-607	-607
0.437	-613	-616
0.876	-616	-628
1.308	-625	-634

Table 4.6. Multiplication factor difference between the SP_3 and the Monte Carlo approaches.

Core average void fraction (%)	$k_{eff,SP3} - k_{eff,MC}$ (pcm)	
	Uniform bubble distribution	*Real bubble distribution*
0	-529	-529
0.437	-531	-536
0.876	-536	-547
1.308	-544	-552

Good agreement is also obtained in the prediction of the void reactivity coefficient, as shown by Tables 4.7 and 4.8. Beside the differences among the deterministic and the Monte Carlo approaches, a possible source of error may be represented by the albedo boundary conditions adopted in the deterministic model. In fact, the treatment of neutron leakages may have a relevant impact on the evaluation of the void reactivity feedback. As expected, the SP_3 solver is in better agreement with the Monte Carlo results, as compared to the diffusion approach. Visible improvement is observed in the prediction of the multiplication factor, and of the void coefficient as well. Considering that the bottleneck in runtime is due to thermal-hydraulics, and not to neutronics, the use of the SP_3 solver only leads to an increase of about 17% of computational times, as compared to the diffusion solver. In this regard, the adoption of an SP_3 approach represents a valuable addition to the multiphysics analysis of the MSFR, since (i) it is more accurate than neutron diffusion, without significantly increasing computational requirements, and (ii) it can be coupled with the moving precursor balance equations, as opposed to Monte Carlo methods which consider static fuel.

Table 4.7. Void coefficient relative difference between the diffusion and the Monte Carlo approaches.

Core average void fraction (%)	α_v relative difference (%)	
	Uniform bubble distribution	*Real bubble distribution*
0	-	-
0.437	10.24	8.26
0.876	7.78	9.63
1.308	10.10	8.49

Table 4.8. Void coefficient relative difference between the SP_3 and the Monte Carlo approaches.

Core average void fraction (%)	α_v relative difference (%)	
	Uniform bubble distribution	*Real bubble distribution*
0	-	-
0.437	4.07	6.55
0.876	6.16	8.26
1.308	8.48	7.26

4.3 Conclusive remarks

In Chapter 3, a simplified 2D analysis of the helium bubbling system has shown that the void coefficient is strongly dependent on the void fraction distribution. In this chapter, the same analysis is extended by considering the real three-dimensional geometry of the MSFR. The results of this study lead to analogous conclusions, pointing out that spatial as well as importance effects have a strong impact on the void reactivity feedback of the bubbles. Consequently, an accurate calculation of the bubble spatial distribution is required to evaluate the system reactivity and the void coefficient in turn, which is necessary for future developments of appropriate control strategies.

The outcomes of this work constitute the starting point for further research on the MSFR dynamics, with a particular focus on the analysis and the development of the reactivity control systems as well as of the optimization of the most relevant design features of the reactor (notably, the fuel composition, the operating temperatures, and the fuel flow rate). In particular, this study can be useful for the design of the bubble injection and extraction systems, providing guidelines for the optimization of their position in the reactor. Thanks to the capability of the multiphysics model of handling large 3D and unstructured meshes, the real geometry of the system can be kept into account.

Finally, the present study is also aimed at highlighting the difference between a deterministic description of neutronics and a Monte Carlo approach. On one side, the six-group approximation and the albedo boundary conditions adopted in the SP_3 and in the diffusion models may be a source of error, as compared to the continuous-energy Monte Carlo approach. On the other hand, standard Monte Carlo codes do not have the capability to model the precursor motion through the circulating fuel (except from a preliminary development presented by Aufiero et al., 2017), which is also fundamental for a correct estimation of reactivity in liquid fuel nuclear reactors. However, a general good agreement is obtained among the deterministic and the Monte Carlo approaches, both in the prediction of the multiplication factor and of the void reactivity coefficient. This result constitutes an important verification of the ability of the multiphysics solver to correctly catch the coupling between neutronics and the bubbly flow.

Chapter 5

Analysis of fuel compressibility effects

Abstract

Compressible fluid dynamics is of great practical interest in many industrial applications, ranging from chemistry to aeronautical industry, and to the nuclear field as well. At the same time, modelling and simulation of compressible flows is a very complex task, requiring the development of specific approaches, in order to describe the effect of pressure on the fluid velocity field. Compressibility effects become even more important in the study of two-phase flows, due to the presence of a gaseous phase. In addition, compressibility is also expected to have a significant impact on other physics, such as nuclear reactions occurring in the mixture. In this perspective, multiphysics represents a useful approach to address this complex problem, providing a way to catch all the different physics that come into play as well as the coupling among them. In this chapter, the multiphysics model proposed in the thesis is employed to study the compressibility effects of the fluid that acts as fuel in the MSFR. The fuel mixture compressibility is expected to have an important effect on the system dynamics, especially in very rapid super-prompt-critical transients. In addition, the presence of a helium bubbling system used for online fission product removal could modify the fuel mixture compressibility, further affecting the system transient behaviour. Therefore, the MSFR represents an application of concrete interest, inherent to the analysis of compressibility effects and to the development of suitable modelling approaches. Thanks to the coupling between neutronics and two-phase, compressible fluid-dynamics, the multiphysics OpenFOAM model developed in this thesis is suitable to describe the interplay between compressibility and the bubbly flow, as well as its impact on reactivity. The outcomes of this analysis point out that the fuel compressibility plays a crucial role in the evolution of fast transients, introducing delays in the expansion feedbacks that strongly affect the system dynamics. Moreover, it is found that the gas bubbles significantly alter the fuel compressibility, yielding even larger differences as compared to the incompressible approximation usually adopted in the current MSFR solvers.

The content of this chapter is based on:

Cervi, E., Lorenzi, S., Cammi, A., Luzzi, L., 2018a. Analysis of the effect of fuel compressibility on super-prompt-critical dynamics of the Molten Salt Fast Reactor, PHYSOR 2018: Reactor Physics Paving The Way Towards More Efficient Systems, Cancun, Mexico, April 22-26, 2018.

Cervi, E., Lorenzi, S., Cammi, A., Luzzi, L., 2019a. Development of a multiphysics model for the study of fuel compressibility effects in the Molten Salt Fast Reactor, Chemical Engineering Science 193, 379-393.

5.1 Introduction

Compressibility plays a crucial role in the propagation of waves within a fluid, since pressure and density perturbations travel at a finite velocity through the medium. The relative propagation velocity of the waves with respect to the fluid represents the local speed of sound. Although all the real fluids are compressible, this property can be often neglected, introducing the incompressibility approximation and assuming an infinite speed of sound (Thompson, 1972). However, there are many industrial applications, ranging from high-pressure chemistry to supersonic aerodynamics, in which the incompressible approximation is not suitable, since the fluid density is strongly affected by pressure. As compared to incompressible fluid dynamics, the study of compressible flows requires a specific treatment both from a theoretical and numerical point of view, calling for the coupled solution of the continuity, momentum and energy equations (Moukalled, 2016). In addition, the density variation may have important feedbacks on other physics involved in the problem, further complicating the analysis of many complex systems of industrial interest (e.g., chemical and nuclear reactors).

Compressibility effects become of particular interest in the analysis of two-phase liquid-gas flows. In this situation, the presence of gas bubbles may have a relevant impact on the average mixture compressibility. In addition, local effects may also arise in case of strongly heterogeneous spatial distributions of the gaseous phase, leading to phenomena that cannot be caught with single-phase or homogeneous-mixture approaches.

In this sense, the multiphysics approach constitutes a valuable tool to address the problem, providing an efficient way to describe all the different physical phenomena occurring in an industrial process (Cammi et al., 2011b; 2012; Aufiero et al., 2014a; 2014b; Fiorina et al., 2014). In this chapter, the multiphysics modelling approach presented in the thesis is employed for the analysis of the impact of fuel compressibility during super-prompt-critical transients in the MSFR.

Due to the negative temperature feedback coefficient of the MSFR (Gerardin et al., 2017), temperature increases during power excursions lead to a reduction of the system reactivity. This feedback is partly due to the Doppler effect, related to the neutron captures by the fertile nuclides, and partly to the thermal expansion of the fuel, which increases neutron leakages. While the Doppler effect acts promptly to reduce the system reactivity, the expansion feedback is delayed, since a density perturbation takes a finite time to propagate through the reactor.

In the MSFR, the speed of sound in the fuel mixture is about 1200 m/s, hence sufficiently high to consider the pressure wave propagation connected to the fluid compressibility as “instantaneous” in most transient scenarios (Aufiero et al., 2017). On the other hand, this may not be the case for very rapid super-prompt-critical transients, which could be a reason of concern during the reactor start-up, due to unwanted fuel injections. In fact, the characteristic times of these transients are in the order of a few milliseconds, comparable to the propagation time of pressure waves in the reactor. This

could lead to a delay of the expansion mechanism, resulting in an overall weaker feedback. For this reason, the adoption of incompressible approximation (Aufiero et al., 2014a; 2014b; Fiorina et al., 2014) may result in significant underestimations of the energy released in super-prompt-critical transients.

In addition, the adoption of the helium bubbling system is expected to further complicate the analysis of this complex problem. The presence of bubbles in the fuel mixture, as well as their spatial distribution, may have a significant impact on the fuel compressibility and on the pressure wave propagation, possibly leading to additional effects that cannot be described with the incompressible approximation. In particular, the bubbles may increase (both locally and globally) the fuel compressibility, further delaying the thermal expansion feedback. In the light of this, the MSFR constitutes an application of industrial interest, inherent at the same time to the modelling of two-phase, compressible fluid dynamics and its coupling with other physics.

The purpose of the present work is to model the compressibility phenomena in the pure liquid salt, and in the bubbly mixture as well, highlighting the coupling among these phenomena and the system neutronics. Thanks to its two-phase compressible thermal-hydraulics model, the multiphysics solver developed in this thesis is suitable to the purpose, being able to model the bubble motion in the liquid fuel and to account for the compressibility of both the phases.

The analyses carried out in Chapters 3 and 4 pointed out that an accurate description of the bubble distribution in the reactor is fundamental for the correct evaluation of the reactor multiplication factor and of the void reactivity coefficient. However, the impact of the helium bubbling system and of compressibility effects on the MSFR transient behaviour is still to be investigated. This chapter aims at filling this gap, highlighting the effect of the fuel compressibility on super-prompt-critical transients, in the pure liquid salt as well as in presence of the helium bubbles. Compressibility effects in super-prompt-critical transients are pointed out by Aufiero et al. (2017), assuming a uniformly distributed gas phase (i.e., modelling the bubbles as a uniform density effect and introducing an average speed of sound, using a single-phase fluid-dynamics solver). As compared to the available literature, the novelty of the present analysis is that the local effect of the bubble spatial distribution on the fuel mixture compressibility is highlighted. To this aim, pressure wave propagation through the reactor is studied i) considering the bubble distribution calculated by the multiphysics solver, and ii) assuming a uniform distribution with the same average void fraction. In addition, the impact of the pure liquid salt compressibility, without helium bubbles, is also investigated.

5.2 The investigated system

The multiphysics model described in Chapter 2 is used to simulate a transient in the MSFR, highlighting the impact of the fuel compressibility on the system dynamics. In particular, a super-prompt-critical transient at the reactor start-up is chosen as case study in the present work. The power ramp procedure from low initial power is a

possible initiator of a reactivity accident, due to an unwanted, fuel injection. This situation can be particularly concerning if the helium bubbling system is active during start-up. In the light of the high void coefficient (see Chapters 3 and 4), an accidental fuel injection may suddenly decrease the void fraction leading to a super-prompt-critical reactivity insertion.

A simplified axial-symmetric 2D geometry (Brovchenko et al., 2013) is adopted for the present study (Figure 5.1a). At $t = 0$, the system is in zero-power condition, the fuel temperature is 923 K (equal to the design inlet temperature) and the initial reactivity, evaluated with the power iteration routine, is equal to 500 pcm. The power iteration routine is employed on the initial configuration, i.e., at $t = 0$, before starting the transient simulation. Therefore, the criticality and the time-dependent calculations are carried out independently each from the other. Also note that a 500 pcm reactivity is super-prompt-critical in the MSFR, whose effective delayed neutron fraction is around 120-150 pcm (Aufiero et al., 2014a).

5.2.1 Modelling assumptions

As in Chapters 3 and 4, the following models are selected to describe the bubbly flow in the MSFR:

- *Bubble diameter:* isothermal model Eq. (3.5), with $d_0 = 3$ mm at $p_0 = 1$ atm;
- *Drag force:* Schiller-Naumann correlation (Schiller and Naumann, 1933);
- *Virtual mass forces:* constant coefficient correlation with $C_{vm} = 0.5$;
- *Interphase heat transfer:* Ranz-Marshall correlation (Ranz and Marshall, 1952).

It's worth noting that, in the light of the strong pressure waves observed in this chapter (see Section 5.3), the isothermal model should be particularly suitable to evaluate the bubble diameter. In fact, assuming helium as a perfect gas, the pressure impact on the bubble volume is more important as compared to temperature, since $p \gg RT$. In addition, the heat transfer model should have a negligible impact on the transients, due to their small characteristic time scales. In the light of this, bubbles are more heated by adiabatic compression (due to the strong pressure waves arising during the transients), rather than by heat-exchange with the liquid fuel. In addition, the effect of lift and turbulent dispersion on the interphase momentum transfer is neglected while the Lahey k-ε turbulence model (Lahey, 2005) has been adopted to account for the contribution of the dispersed gaseous phase on eddy viscosity. A sensitivity analysis on these models and correlations has been carried out in Chapter 3, while the impact of the main parameters driving the pressure wave propagation, (i.e, the fuel thermal expansion and the compressibility coefficients) will be presented in Section 5.3.4.

The neutron flux is estimated using multi-group diffusion with six energy groups. Six-group cross sections (with the same energy cutoff values as Chapters 3 and 4) and albedo coefficients are generated using a Serpent model of the same simplified geometry, considering also the reflectors and the blanket (see Figure 5.2b). Simulations run with the SP_3 model showed negligible differences as compared to the diffusion one.

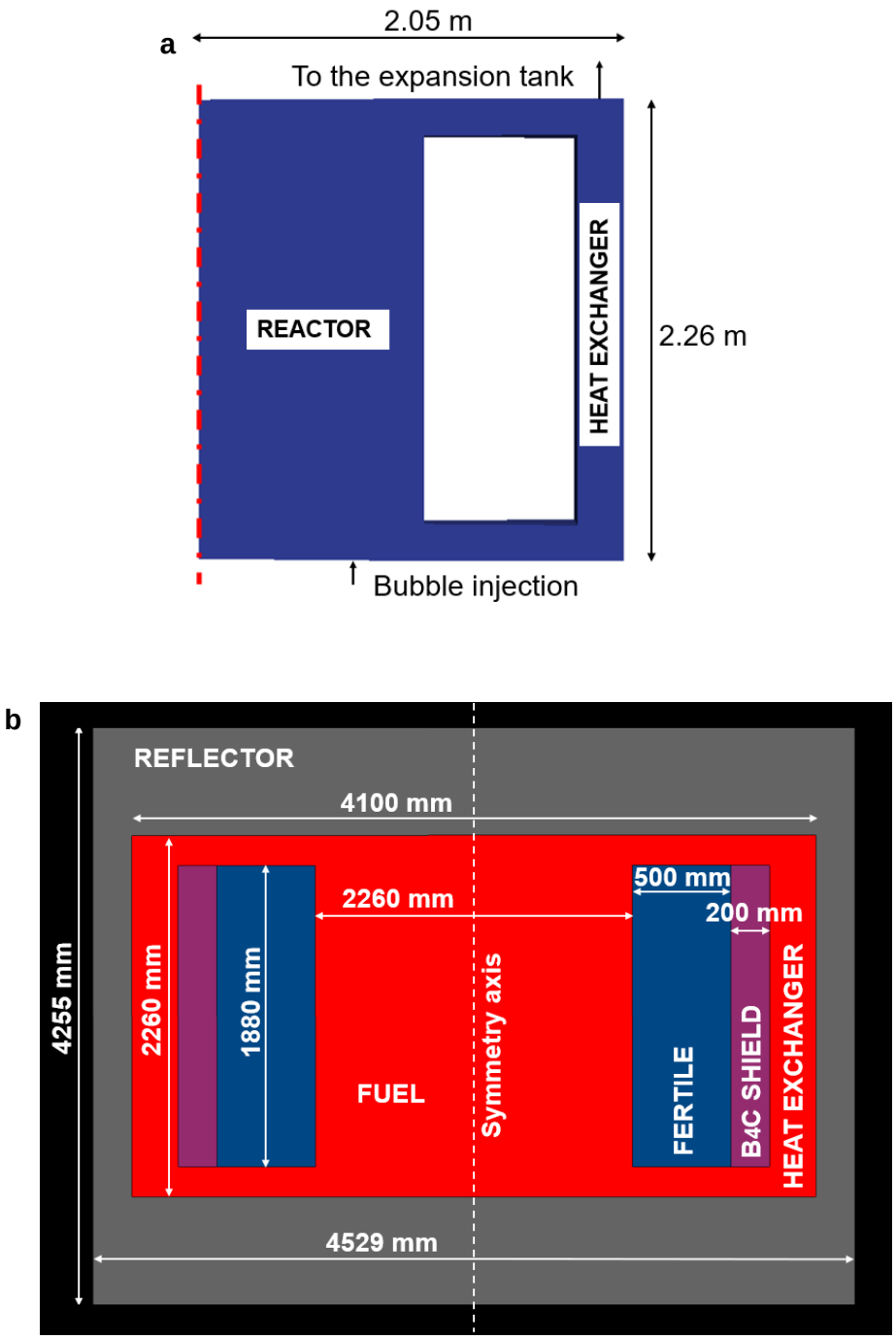

Figure 5.1. Simplified geometry of the MSFR adopted in this analysis. OpenFOAM (a) and Serpent (b) models.

Finally, concerning the boundary conditions, the solid structure around the liquid domain is considered as ideally rigid, since a detailed thermo-mechanical analysis of the vessel and of the external circuit is out of the scope of the present work. Following this assumption, pressure waves reaching the boundary are totally reflected by the rigid walls (Thompson, 1972).

5.3 Results

5.3.1 Effect of the pure salt compressibility on the MSFR dynamics

In this Section, the presence of bubbles in the fuel mixture is not taken into account, in order to highlight only the effects due to the pure salt compressibility. The transient is simulated in two different cases:

- *Compressible fuel (Case I-a):* the fuel density depends on temperature and pressure according to the following linear law:

$$\rho_{fuel} = \rho_0 - \beta_{th}\left(T - T_{ref}\right) + \psi\left(p - p_{ref}\right) \tag{5.1}$$

  where ρ_0 = 4125 kg/m^3, β_{th} = 0.882 kg/m^{3}K and T_{ref} = 973 K (Ignatiev et al., 2012). The isothermal compressibility ψ is evaluated as:

$$\psi = \frac{\rho_{fuel}}{K_{fuel}} \tag{5.2}$$

  where K_{fuel} is the bulk modulus of the pure salt, for which a value of 6.3 GPa can be adopted (Aufiero et al., 2017), while at 923 K ρ_{fuel} = 4169 kg/m^3. In addition, it is assumed that $p_{ref} = 2$ bar in Eq. (5.1). A discussion on the result sensitivity to the values of β_{th} and ψ is presented in Section 5.3.4.

- *Incompressible fuel (Case I-b):* the fuel density is evaluated by means of Eq. (5.1), assuming $\psi = 0$. In this way, thermal expansion, as well as its effects on neutronics and thermal hydraulics, is taken into account. On the other hand, the dependence of density on pressure is neglected, meaning that pressure waves cannot propagate through the fuel.

It is worth noting that the momentum equation Eq. (2.9) is solved in its complete form in every case study considered in this chapter, even if some terms (e.g., the stress tensor) are usually neglected in pressure wave problems (Thompson, 1972). Eq. (2.22) is solved as well, even if decay heat should not have a strong impact due to the small characteristic times of the super-prompt-critical transients studied in this chapter.

Time evolution of core power and pressure field in Cases I-a and I-b is presented in Figures 5.2 and 5.3, respectively. For the sake of completeness, the temperature fields of the different cases are presented in Section 5.3.5. The power peak value predicted in the compressible case (Case I-a) is 28% higher, as compared to the incompressible case (Case I-b). The time evolution of the pressure field is also completely different in the two cases. While in the compressible case (Case I-a) a pressure wave propagates from the centre to the reactor walls, in the incompressible case (Case I-b) no wave is observed. Since in Case I-a the pressure wave takes a finite time to propagate through the reactor, the fuel expansion feedback is delayed, and only the Doppler effect acts promptly to counterbalance the reactivity insertion. For this reason, the power release is higher in Case I-a, as compared to Case I-b.

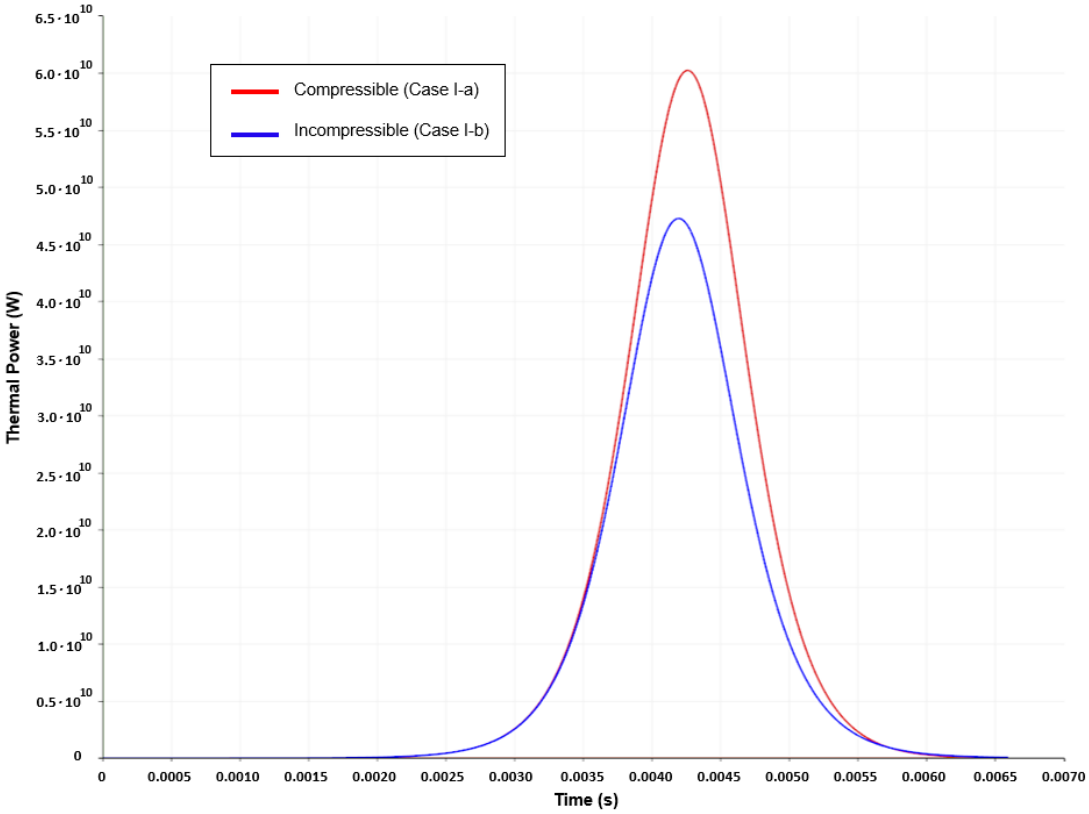

Figure 5.2. Effect of the pure salt fuel compressibility on the power transient. Two cases are considered: compressible fluid (red curve) and incompressible fluid (blue curve).

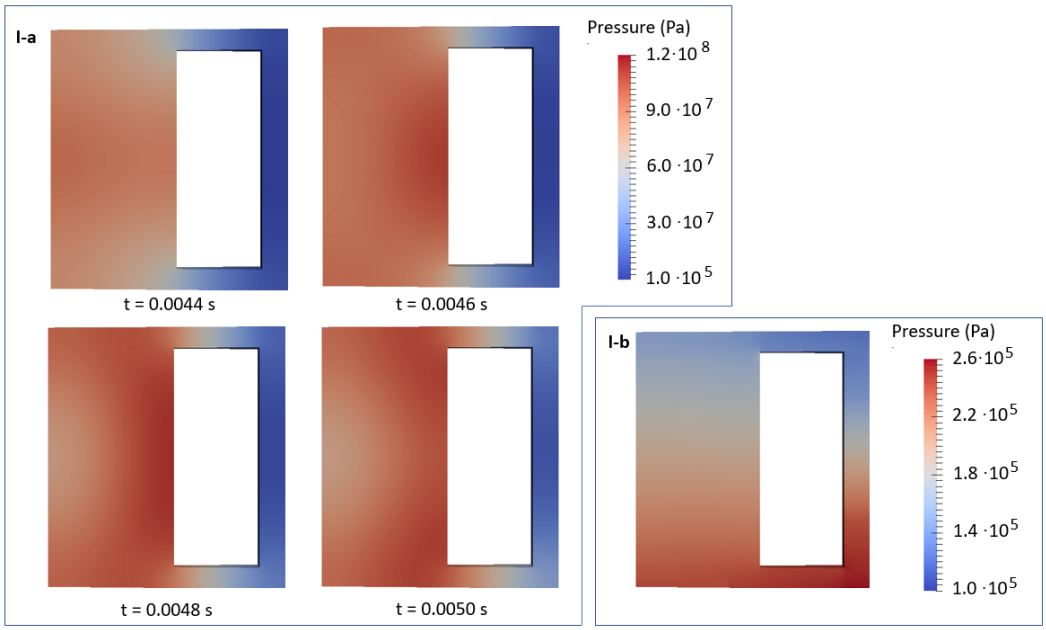

Figure 5.3. Pressure field in the compressible (Case I-a) and incompressible (Case I-b) pure salt. Pressure waves are eliminated by assumption in the incompressible case. Therefore, the pressure field does not change during the transient in Case I-b.

5.3.2 Effect of the fuel mixture compressibility on the MSFR dynamics with bubbles

The same transient is now simulated also considering the presence of the bubbles and the helium bubbling system. The injection point as well as the bubble spatial distribution (evaluated with the multiphysics solver) are represented in Figure 5.4. The bubbles are injected at the bottom of the reactor and are removed in the heat exchanger region, by considering suitable source terms in the continuity equation Eq. (2.8). The core-averaged value of the gas fraction is 0.67%. The following three cases are considered:

- *Compressible fuel (Case II-a):* the fuel density depends on temperature and pressure according to Eq. (5.1), while the helium density is evaluated using the equation of state for ideal gases, depending in turn on pressure and temperature. The spatial bubble distribution is calculated by the multiphysics solver in steady-state conditions (Figure 5.4) is and used as initial condition for the transient simulation.

- *Compressible fuel with uniform bubble distribution (Case II-b):* as in Case II-a, both the fuel and the helium are treated as compressible fluids. However, a uniform bubble distribution is assumed instead of the one calculated with the solver and presented in Figure 5.4. The uniform gas fraction is 0.67%, equal to the core-averaged value of Case II-a.

- *Incompressible fuel (Case II-c):* again, the fuel density is evaluated by means of Eq. (5.1), assuming $\psi = 0$, while a density of 0.1 kg/m^3 is assumed for helium, corresponding to a temperature of 923 K and a pressure of 2 bar. The bubble distribution calculated by the solver is assumed in this case (see Figure 5.4).

Due to the void reactivity feedback introduced by the bubbles, the system multiplication factor (evaluated with the power iteration routine implemented into the solver) decreases, as compared to Section 5.3.1, in which the bubbles are not considered. Moreover, the reactivity of Case II-b is different from Cases II-a and II-c, due to the different distribution of the void fraction (see Chapters 3 and 4). For this reason, the value of $\bar{\nu}$ in the diffusion equation Eq. (2.16) is suitably rescaled so that the initial reactivity is equal to 500 pcm in all the cases. This is to ensure that the differences observed in the various cases are only due to the fuel compressibility, and not to a different initial reactivity insertion. Time evolution of core power and pressure field in Cases II-a, II-b and II-c is presented in Figures 5.5 and 5.6, respectively.

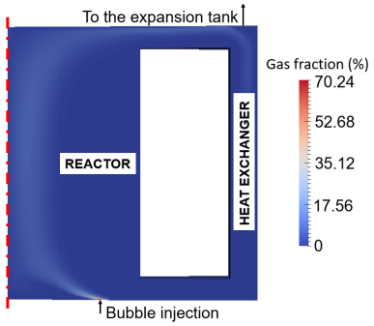

Figure 5.4. Reactor geometry and bubble distribution adopted in Cases II-a and II-c.

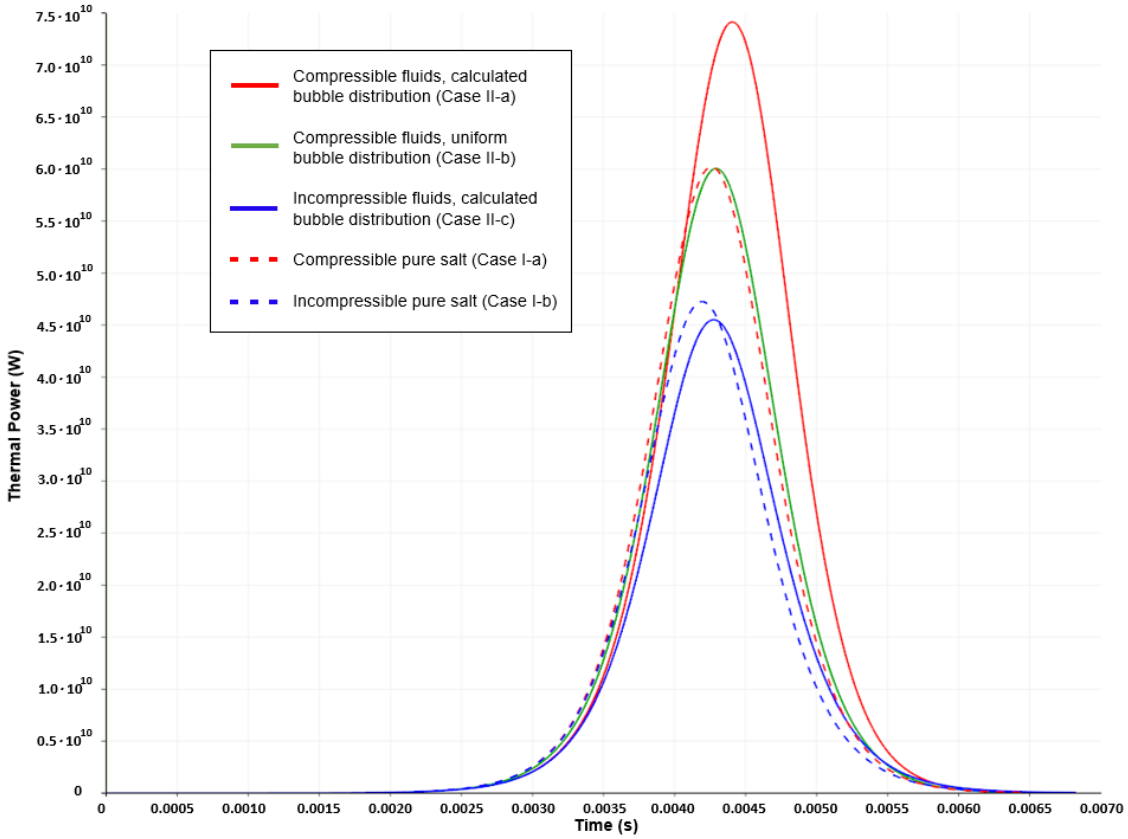

Figure 5.5. Effect of the fuel mixture compressibility (in presence of helium bubbles) on the power transient. Three cases are considered: compressible fluids with calculated bubble distribution (red curve), compressible fluids with uniform bubble distribution (green curve) and incompressible fluids (blue curve). The pure liquid salt cases of Figure 5.2 are also reported for comparison (dashed lines).

The power peak value predicted in the compressible cases (Cases II-a and II-b) is 64% and 33% higher, respectively, as compared to the incompressible one (Case II-c). This indicates that, as compared to the pure salt, the helium bubbles increase (both locally and globally) the fuel mixture compressibility, further delaying the expansion feedback and leading to a larger energy release. This effect is stronger in Case II-a, as compared to Case II-b, suggesting that the bubble spatial distribution also plays a fundamental role in determining the system dynamics, locally affecting the fuel mixture compressibility. In addition, microscopic effects such as a strongly localized bubble compression in the center of the reactor, as in Case II-a, can lead to a sudden decrease of the void fraction, further increasing reactivity and the energy release in turn.

The effect of the bubble distribution is also evident from Figure 5.6. When a uniform bubble distribution is assumed (Case II-b) the pressure wave has a spherical shape, similarly to the compressible case with pure salt only (Case I-a). However, when the spatial bubble distribution calculated by the solver is considered (Case II-a), the wave-front shape is completely modified by the presence of the bubbly flow. In more detail, pressure waves become steeper when they encounter high-bubble-concentration regions, due to the sudden decrease of the speed of sound. It is also interesting to note that, in Case II-a, wave reflections occur at the reactor wall. This suggests that the

wave-front path is also dependent on the reactor geometry, which may have an important role on the system behaviour in super-prompt-critical scenarios. As a further note, the elasticity of the reactor walls (here considered as completely rigid) could also have an important effect on wave reflections (this issue is out of the scope of the present work and will be investigated in the future).

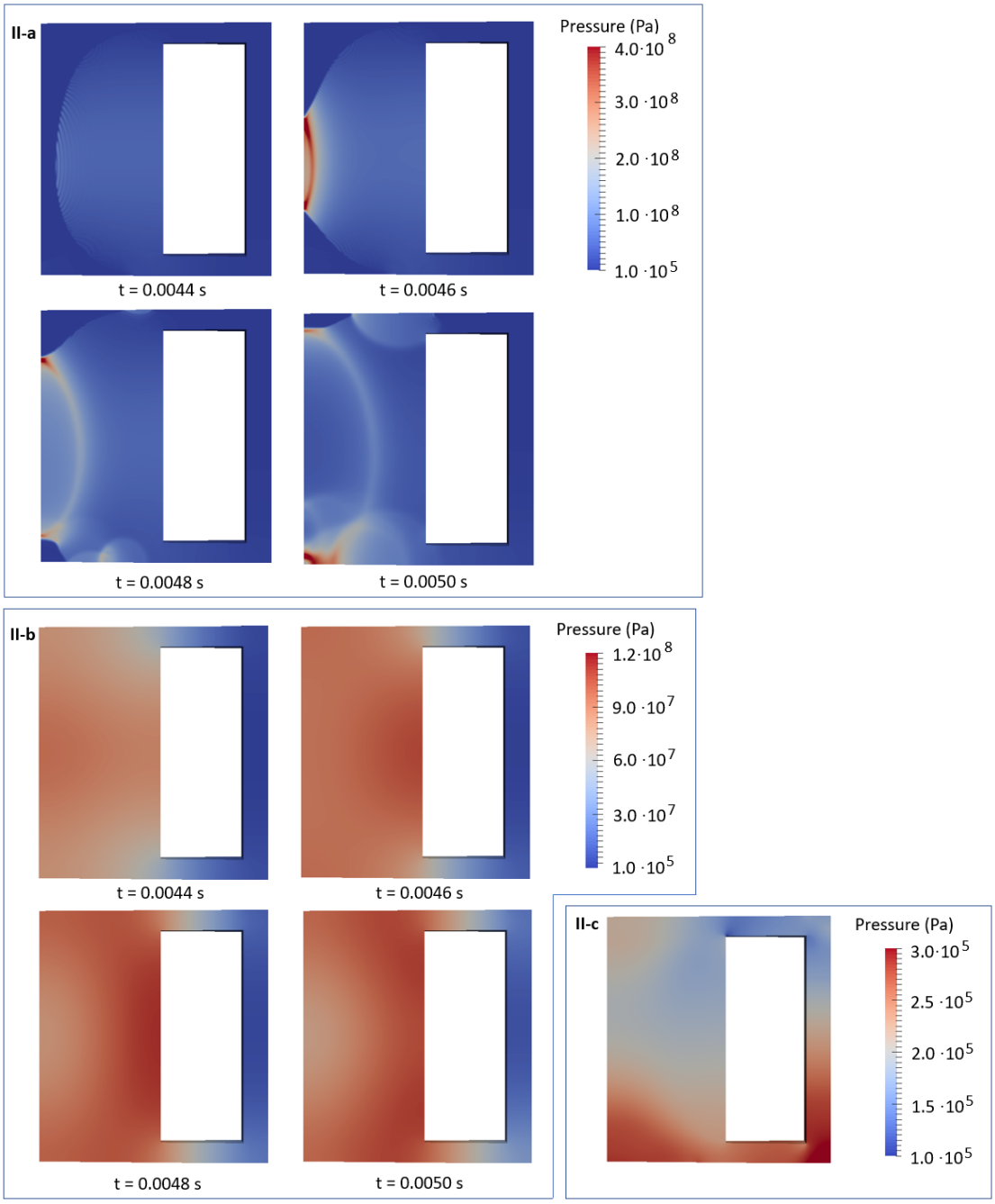

Figure 5.6. Pressure field in the compressible fuel mixture with non-uniform (Case II-a) and uniform (Case II-b) bubble distributions and in the incompressible fuel mixture (Case II-c). Again, pressure waves are eliminated by assumption in this last case. Note that Case II-b is very similar to Case I-a, since in both cases the speed of sound is uniform over the whole medium. However, when the calculated bubble distribution is considered (Case II-a), the wave propagation changes completely.

5.3.3 Comparison and discussion of results

In all the cases, the power increases of 10 decades, going from zero to about 40-70 GW. Then, the reactor is shut down by the reactivity feedback related to the Doppler effect and to the salt expansion introduced during the power excursion. However, the peak value of the power evaluated in the compressible cases strongly differs, as compared to the incompressible ones, both in Sections 5.3.1 and 5.3.2. In fact, in the incompressible cases, the thermally-expanded fuel rigidly translates to the expansion tank. On the other hand, in the compressible cases, the pressure wave due to the thermal expansion travels at the speed of sound, requiring a finite time to propagate through the reactor. Thus, while in the incompressible cases both the Doppler and the expansion feedbacks act promptly to counterbalance the reactivity insertion, in the compressible cases the expansion feedback is delayed, leading to a higher reactivity and, as a consequence, to a larger power excursion. The results of Sections 5.3.1 and 5.3.2 are summarized in Table 5.1.

Table 5.1. Relative power increase in the considered case study.

Cases	**Power increase**
Without bubbles (Case I-a vs. Case I-b)	+28%
With bubbles – calculated distribution (Case II-a vs. Case II-c)	+64%
With bubbles – uniform distribution (Case II-b vs. Case II-c)	+33%

Even in the pure salt, without considering the helium bubbling system (Case I-a vs. Case I-b), compressibility has a sensible effect on the energy release. Therefore, in the case of super-prompt-critical reactivity insertion, the incompressible approximation is not acceptable not only for the gas phase, but also for the liquid salt. Nevertheless, the bubbles play an important role, since they increase the fuel mixture compressibility both locally and globally, further delaying the expansion feedback and leading to a stronger power excursion.

In addition, results are strongly dependent on the bubble spatial distribution. When a uniform bubble distribution is considered, the power increase in the compressible case (Case II-b) with respect to the incompressible case (Case II-c) is 33%. This increase is only slightly larger as compared to the pure liquid salt, in which the power peak in the compressible case (Case I-a) is 28% higher with respect to the incompressible case (Case I-b). In fact, both in Case I-a and II-b, the speed of sound through the medium is uniform and, as a consequence, the shape of the wave-front is similar. In addition, the speed of sound in helium is about 1000 m/s, not much smaller than speed of sound in the salt (about 1200 m/s). For this reason, the presence of gas bubbles only yields an additional power increase of 5%, as compared to the pure liquid salt. Therefore, even if the bubbles have a visible effect, the most important contribution is due to the liquid compressibility. Again, this confirms that the liquid compressibility should be properly modelled, for an accurate simulation of fast transients.

On the other hand, in Case II-a (compressible fuel mixture with calculated bubble distribution), most of the bubbles are concentrated in the centre of the reactor, as calculated by the multiphysics solver. As a consequence, the mixture compressibility becomes non-uniform, and increases in the central region of the core, where the neutron

importance is higher. For this reason, the effect of compressibility on the system reactivity is stronger, leading to a significantly higher power increase (64%). In this case, the presence of bubbles inside the reactor yields an additional power increase of 36%, as compared to the pure liquid. Therefore, accurate models are required to predict the bubble spatial distribution. In fact, simply assuming a uniform distribution would result in a strong underestimation of the energy release.

As expected, higher pressure values are observed in Case II-a, where a non-uniform bubble distribution is considered. It is well known that when a pressure wave encounters a region of lower acoustic impedance (given by the product between the medium density and speed of sound), the transmitted and reflected waves are stronger than the incident one (Davison, 2008). In the light of this, the lack of heterogeneous regions is a further explanation of the similar behavior observed between Case I-a (pure compressible salt) and Case II-b (compressible fuel mixture with uniform bubble distribution).

5.3.4 Sensitivity to thermal expansion and compressibility coefficients

The purpose of this section is to discuss the sensitivity of the power transients to the main salt properties driving the generation and the propagation of pressure waves through the reactor, i.e., the thermal expansion and the compressibility coefficients. In more details, the thermal expansion coefficient triggers the formation of pressure waves, as temperature increases, while the compressibility coefficient makes the waves propagate with a finite velocity through the reactor. Therefore, both these properties must be considered to study the compressibility effects presented in the manuscript.

Ignatiev et al. (2012) found the following experimental correlation between fuel density and temperature, without considering the effect of pressure:

$$\rho_{fuel} = \rho_0 - \beta_{th}\left(T - T_{ref}\right) \tag{5.3}$$

where ρ_0 = 4125 kg/m^3, β_{th} = 0.882 kg/m^{3}K and T_{ref} = 973 K. The measurement error is estimated as 0.9% (Ignatiev et al., 2012), even if no specific information is given on the uncertainty of β_{th}. On the other hand, to the best of the authors' knowledge, no information is available on the uncertainty of the compressibility coefficient.

Therefore, a variation of ±10% is considered for both the parameters, in order to assess their weight independently from their different experimental uncertainties. Case II-a (compressible fuel mixture with calculated bubble distribution) is selected for this analysis. In fact, this case is the most interesting and complete, involving both compressibility and two-phase flow, as well as their coupling with neutronics. The power transients obtained by variation of one parameter at a time are shown in Figure 5.7, while the corresponding power peak values are listed in Table 5.2.

Table 5.2. Power peak sensitivity to thermal expansion and compressibility coefficients.

	Peak power (GW)	**Relative difference with respect to reference case (%)**
Reference (Case II-a)	74.1	-
+10% ψ	74.3	0.3
-10% ψ	73.9	-0.3
+10% β_{th}	73.1	-1.3
-10% β_{th}	74.4	0.4

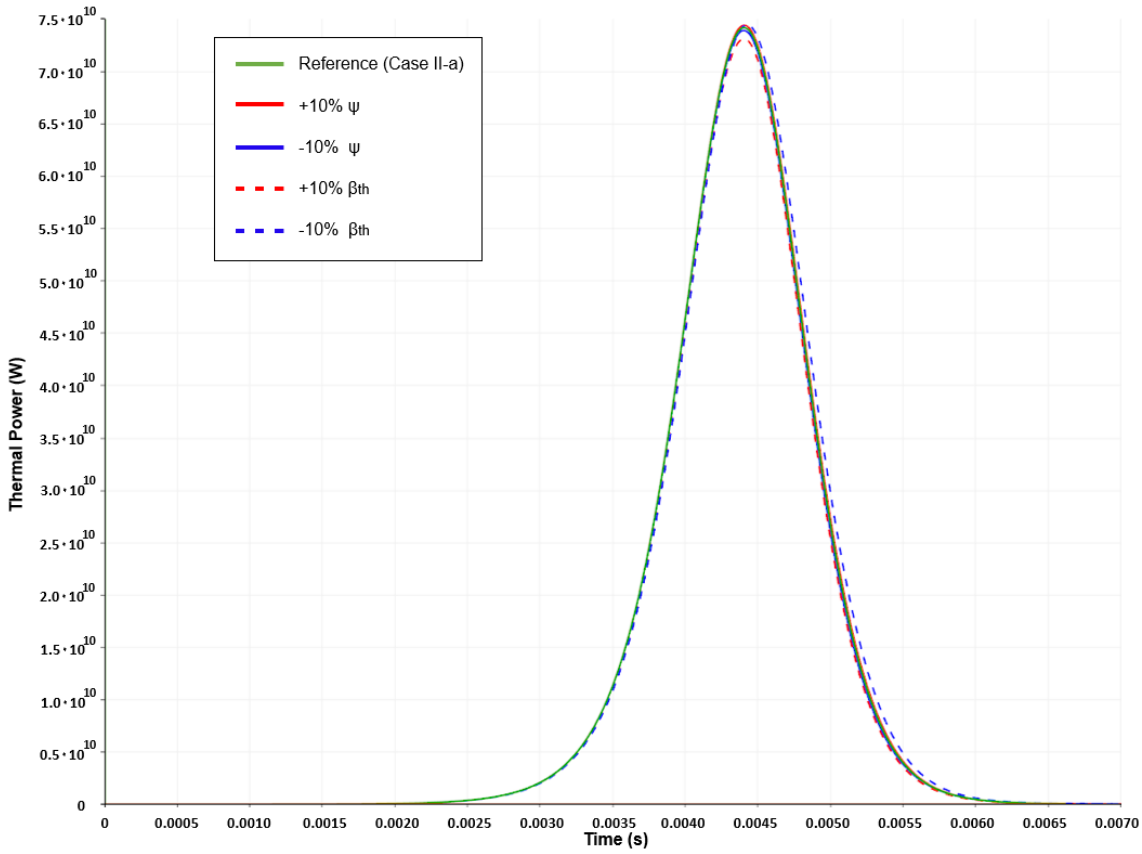

Figure 5.7. Power transient sensitivity to thermal expansion and compressibility coefficients.

Results point out that the peak power increases with the compressibility coefficient. In fact, if compressibility increases, the speed of sound decreases, leading to a larger delay of the thermal expansion feedback and, as a consequence, to a higher energy release. On the other hand, concerning the thermal expansion coefficient, two opposite effects come into play:

1. A higher β_{th} causes a stronger expansion feedback on neutronics, leading to a lower energy release;

2. A higher β_{th} triggers stronger pressure waves and, as a consequence, larger fuel compressions, leading to a higher energy release.

Results point out that the first effect prevails on the second, since the power peak decreases with β_{th}. More in general, it can be observed that transients are slightly more sensitive to β_{th} then ψ, even if sensitivity to both parameters is quite small (±10% perturbations of the coefficients lead to variations of the peak power values that are always smaller than 1.3%). The low sensitivity to the thermal expansion and compressibility coefficients may be due to the higher relative importance of the Doppler feedback as compared to compressibility effects. This is supported by the fact that the maximum fuel temperature is around 1100 K in all the case studies (see Section 5.3.5), suggesting that the Doppler effect neutralizes the reactivity insertion nearly at the same temperature, regardless of the modelling of compressibility effects and of the bubble distribution. Still, a correct description of fuel compressibility and of the two-phase flow is of importance to determine the energy release and the pressure increase in turn, which is fundamental in evaluating the consequences of an accidental reactivity insertion.

5.3.5 Temperature fields

For completeness, the temperature fields of all the considered case studies are presented in this section (Figures 5.8 to 5.12).

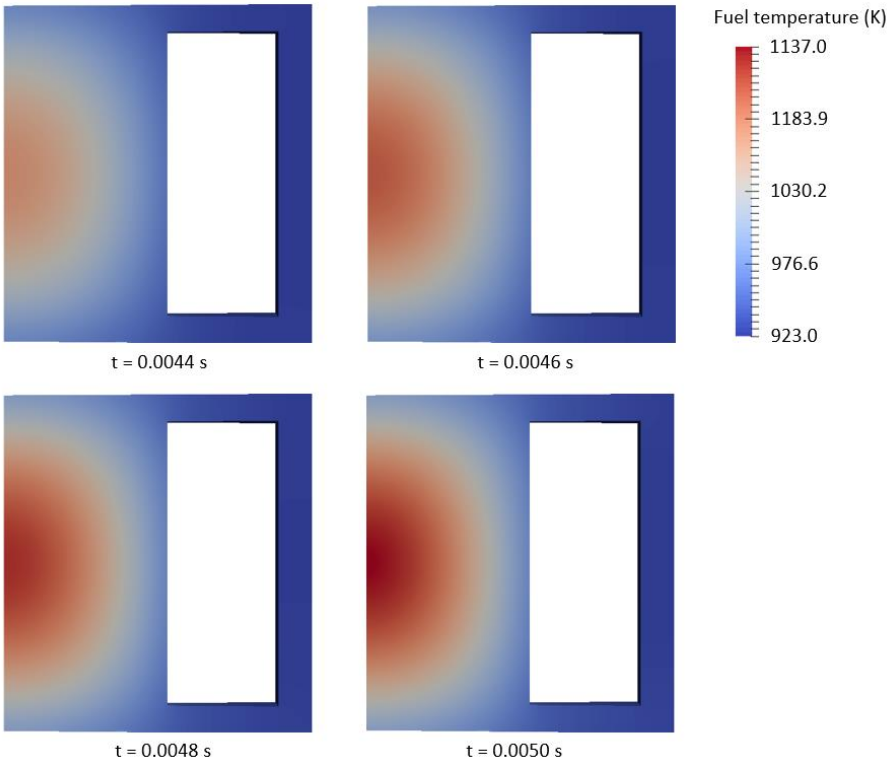

Figure 5.8. Fuel temperature field in Case I-a (Liquid only, compressible fuel).

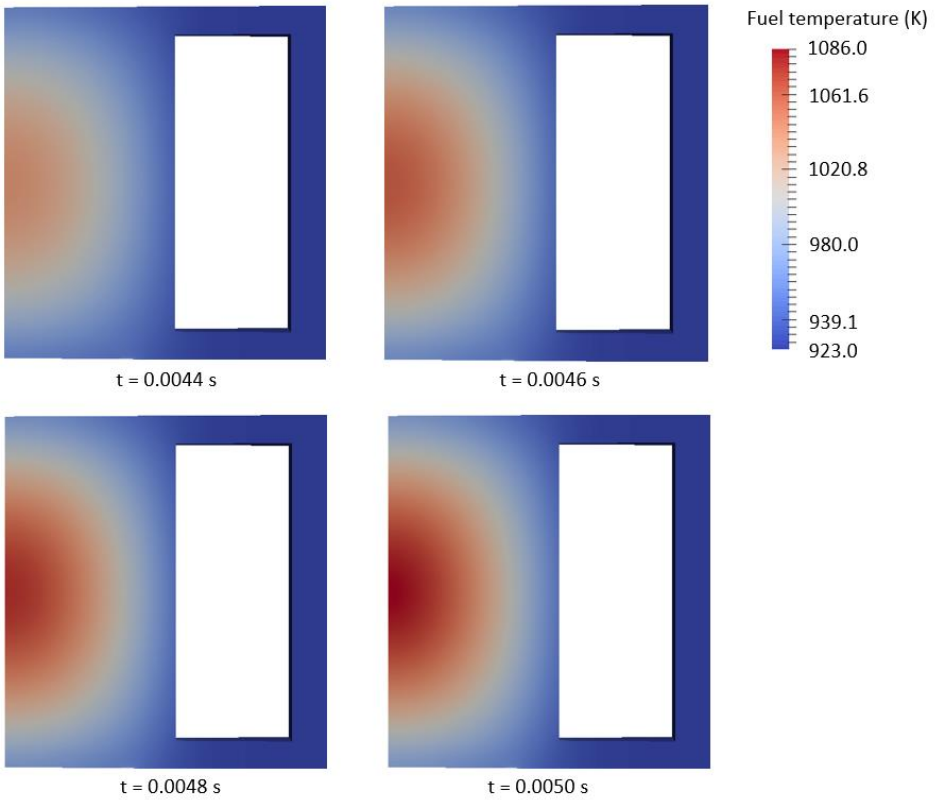

Figure 5.9. Fuel temperature field in Case I-b (Liquid only, incompressible fuel).

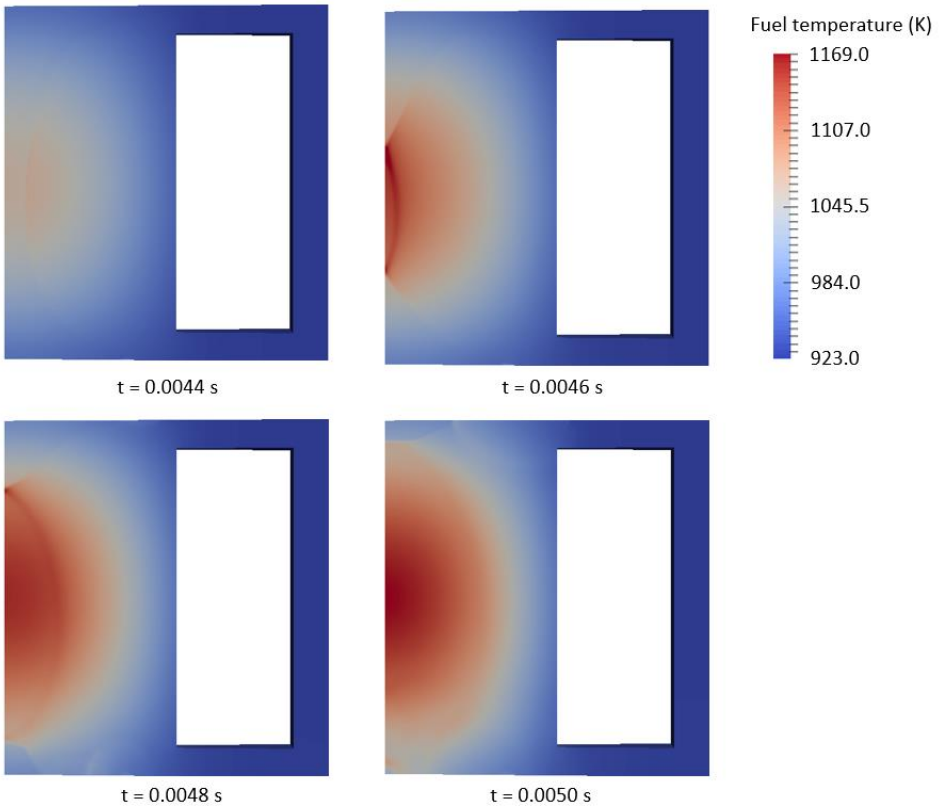

Figure 5.10. Fuel temperature field in Case II-a (Liquid and bubbles, compressible fuel, calculated bubble distribution).

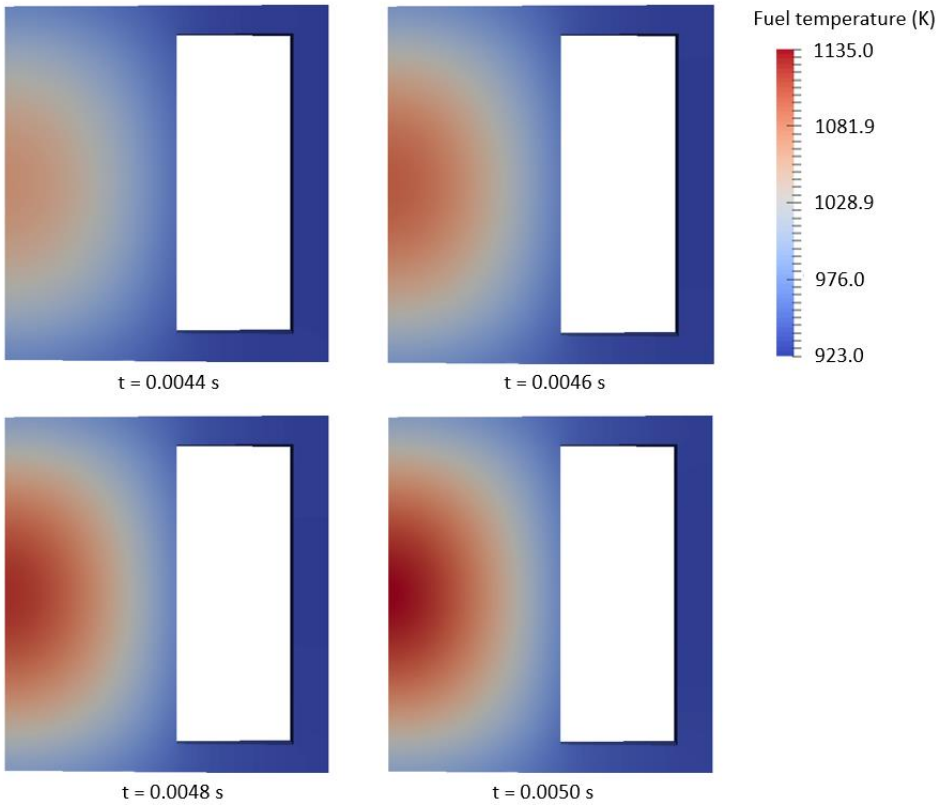

Figure 5.11. Fuel temperature field in Case II-b (Liquid and bubbles, compressible fuel, uniform bubble distribution).

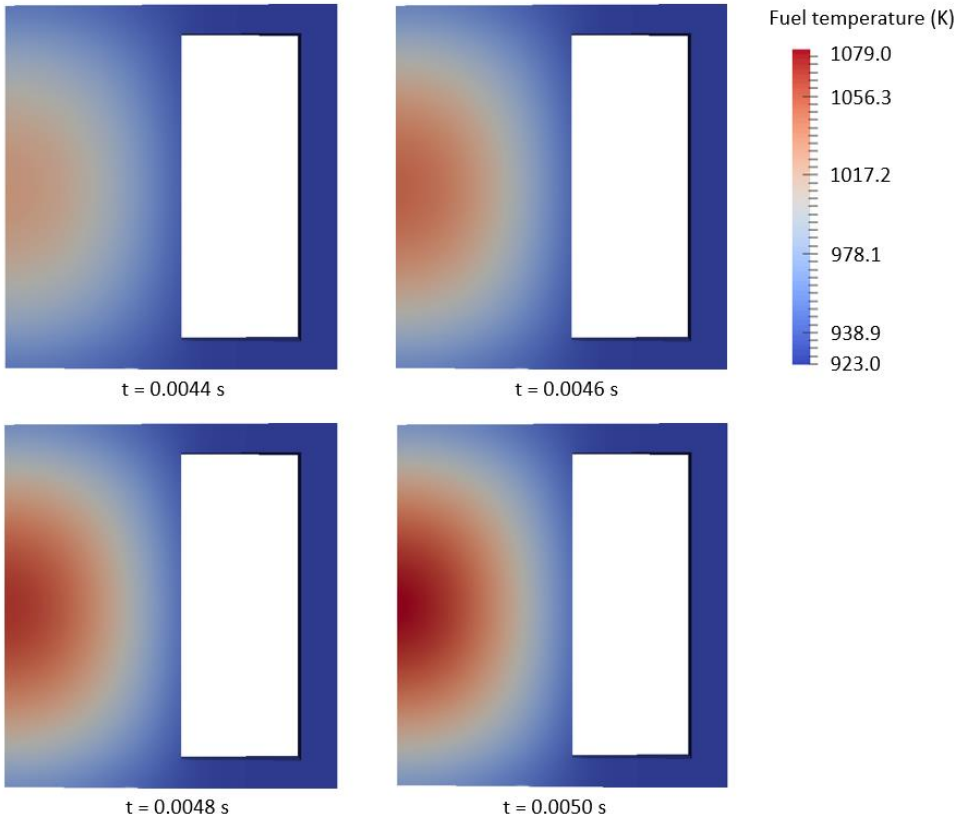

Figure 5.12. Fuel temperature field in Case II-c (Liquid and bubbles, incompressible fuel).

5.4 Conclusive remarks

The Molten Salt Fast Reactor represents an inherent case study for the analysis of two-phase, compressible fluid dynamics and its coupling with other physics, being at the same time an application of scientific and industrial interest. As pointed out in the present work, the helium bubble motion, the propagation of pressure waves in a compressible medium, such as the fuel mixture of the MSFR, and neutronics are strongly coupled each with the other. This is particularly true for fast transients, whose characteristic times are similar to the pressure wave propagation times, at the speed of sound.

In this chapter, particular focus is dedicated to the investigation of the impact of the fuel mixture compressibility during accidental super-prompt-critical scenarios. A power excursion resulting from a 500 pcm reactivity insertion is evaluated i) considering the fuel mixture compressibility, and ii) approximating the fuel mixture as incompressible. The analysis is carried out for the pure salt, and considering the presence of helium bubbles in the reactor as well. Results of this case study point out that approaches neglecting the fuel compressibility may significantly underestimate the power excursions in super-prompt-critical reactivity insertions. Therefore, the incompressible approximation turns out to be unsuitable to simulate fast transients in the MSFR (and other liquid-fuelled Molten Salt Reactors as well), not only for the gas phase, but also for the liquid one. In particular, even when the helium bubbling system is not taken into account, the pure salt compressibility has a significant effect on the transient evolution. The system dynamics is also influenced by the bubble spatial distribution, which affects the fuel mixture compressibility as well as the propagation of pressure waves in the medium.

As a future development, the influence of the wall elasticity and deformability on the wave reflection and transmission could be considered, as well as the wave propagation through the solid reflectors and blanket, which may have an effect on neutron leakages. In addition, a detailed analysis of the fluid-structure interaction between the liquid fuel and the solid walls is required to assess whether the pressure waves could challenge the structural integrity of the walls. Even though these analyses are not in the scope of the present thesis, the preliminary development and verification of a thermal-mechanics model is under investigation (Cervi et al., 2018d; Cervi and Cammi, 2019a; 2020).

As a further note, the fission gas production during the fuel irradiation is also expected to increase the compressibility effects pointed out in this work, as it would represent an additional contribution to the void fraction. Moreover, as compared to helium, these gases typically have a larger molecular mass and, as a consequence, a lower speed of sound and a higher compressibility (Thompson, 1972). Therefore, considering the fission gas production could be an interesting extension of the present analysis.

Conclusions

Molten Salt Reactors represent one of the most promising options in the Generation IV panorama, due to their intrinsic safety and sustainability characteristics (e.g., the possibility of operation at atmospheric pressure and an actinide inventory with lower radiotoxicity) and to the plant simplification allowed by the adoption of a liquid fuel. At the same time, the presence of a molten salt mixture constitutes one of the main challenges in their analysis and simulation, due to the motion of delayed neutron precursors (unlike in traditional solid-fuelled reactors, in which precursors are fixed). Furthermore, the adoption of a helium bubbling system constitutes a further complication for the numerical simulation of the Molten Salt Fast Reactor, as the impact of the gas bubbles on reactivity needs to be carefully investigated. Another specific issue of molten salt reactors is represented by the fuel mixture compressibility which, introducing delays in the thermal expansion feedbacks, has a strong impact on the system dynamics (especially in fast, reactivity-driven transients). Since these issues are specific of circulating fuel reactors only, they were never taken into account in the analysis of traditional solid-fuelled systems. Consequently, simulation codes developed for light water and liquid metal reactors cannot be retrieved for the analysis of the MSFR, and the development of new computational tools, tailored to the specificities of this innovative system, is required. In addition, state-of-the-art models of MSRs are also unsuitable to study the helium bubbling system and fuel compressibility effects, as they rely on single-phase, incompressible fluid-dynamics solvers.

In this context, a new multiphysics OpenFOAM model for the analysis and simulation of the MSFR is developed in the present thesis. A two-phase, compressible thermal-hydraulics model is adopted in order to handle the presence of bubbles in the reactor and to account for the fuel mixture compressibility. The thermal-hydraulics model is coupled with two different neutronics models (multi-group neutron diffusion and SP_3 neutron transport) and with transport equations for the delayed neutron and decay heat precursors. The set-up of this tool constitutes a challenging task, requiring:

- the development of specific models (both from a theoretical and numerical point of view) for each physics that comes into play;

- the development of a coupling strategy to catch the interplay among all the different physics and to properly solve the coupling non-linearities.

Thanks to the new multiphysics simulation tool, the helium bubbling system and fuel compressibility effects have been studied, highlighting phenomena that have never been observed with state-of-the-art tools.

Concerning the analysis of the helium bubbling system and of its effect on reactivity, the main conclusions can be summarized as follows:

- The void reactivity feedback of the bubbles is strongly influenced by spatial and neutron importance effects. Consequently, an accurate evaluation of the bubble spatial distribution inside the reactor is fundamental for a correct evaluation of reactivity and of the void coefficient.

- Simply assuming a uniform bubble distribution (i.e., modelling the void fraction as a uniform density effect) as done by state-of-the-art, single-phase models leads to a significant underestimation of the void coefficient. In case of a sudden decrease of the void fraction (e.g., following a failure of the bubble injection systems), the resulting positive reactivity injection would be underestimated as well. Consequently, the "uniform bubble distribution" approach is strongly non-conservative for the analysis of accidents involving rapid reductions of the bubble concentration.

- Due to the high value of the void coefficient, the adoption of the helium bubbling system for reactivity control purposes may raise safety concerns, at least in its preliminary design consisting in only one injector per cold leg. In addition, the strongly non-uniform bubble distribution may be inefficient for the removal of gaseous fission products. In this regard, a more uniform bubble distribution is desirable (also to obtain a lower void coefficient). This can be achieved by increasing the number of injection systems, at the expense of having more perforation in the reactor vessel.

- The good agreement obtained among different neutronics approaches constitutes an important verification for the developed neutronics models and for the coupling strategy with the thermal-hydraulics herein adopted.

- A sensitivity analysis to bubbly flow closure relations for the evaluation of the bubble diameter and of the interphase momentum and heat transfer points out that results are not significantly affected by the choice of these correlations. Consequently, the conclusions presented in this thesis are solid and reliable, as far as bubbly flow closure relations are concerned.

On the other hand, concerning the analysis of fuel compressibility effects, the following main conclusions can be drawn:

- The fuel mixture compressibility has a strong impact on the system dynamics, introducing delays in the thermal expansion reactivity feedbacks. This is particularly relevant in rapid, super-prompt-critical transients, in which the characteristic times of neutronics and of pressure wave propagation through the reactor are comparable.

- Due to the delay introduced by compressibility, the energy released during fast transients is higher, as compared to the predictions of incompressible models. Consequently, state-of-the-art approaches not accounting for the fuel compressibility are not suitable for a conservative analysis of super-prompt-critical accidental scenarios.

- The presence of gas bubbles inside the reactor modifies the fuel compressibility both locally and globally, leading to further effects that cannot be caught with standard single-phase models. In more details, the bubble distribution needs to be known with accuracy to correctly predict the propagation of the wave-front and of the transient evolution in turn. Therefore, the problems of the helium bubbling system and of fuel compressibility must be studied together.

In the light of these conclusions, the present work constitutes a substantial step forward as compared to state-of-the-art modelling approaches for the MSFR, both from a methodological point of view as well as in terms of results. The outcome of this analysis opens the way to many different research directions:

- A first, interesting development could be a detailed analysis of the fluid-structure interaction between the fuel mixture and the reactor walls. This investigation would serve two different purposes. On one hand, it is necessary to assess if the structural integrity of the walls can be challenged by the strong pressure waves arising in super-prompt-critical transients. On the other hand, wall deformation effects may have an impact on the reflection and transmission of the waves, leading to further effects on the system dynamics.

- In this thesis, the positions of the bubble injectors were selected arbitrarily, since no detailed design information is available at present. However, a sensitivity analysis should be carried out to quantify the impact of the position and of the number of injection systems on the results.

- Even though multi-group neutron diffusion and SP_3 neutron transport perform well in the considered case studies, more accurate neutronics models may be required for some multiphysics applications (e.g., the analysis of smaller and less homogeneous systems, envisaged as potential demonstrators for the MSFR, or to correctly evaluate the irradiation conditions of structural

materials). To this aim, the development and preliminary verification of a discrete ordinate neutron transport model is briefly reported in Appendix A.

- Thanks to the availability of a two-phase fluid-dynamics model, fission gas generation and extraction, as well as the formation of metal precipitates and their transport through the system, can be a further topic to be investigated in the future. This activity is planned in the SAMOFAR follow-up project, SAMOSAFER.

- The development of reduced order models can also be of interest to reduce runtimes, facilitating the optimization of the reactor design (thanks to the possibility to run multiple and faster simulations) and paving the way to real-time control applications.

Appendix A

A discrete ordinate neutron transport model

IN this thesis, multi-group neutron diffusion and SP_3 neutron transport are selected for the development of the multiphysics solver. These models show a good behaviour when applied to large and homogeneous reactors such as the MSFR. However, more advanced neutronics models can be a valuable addition for many multiphysics applications. The analysis of smaller and less homogeneous systems, envisaged as potential demonstrators for the MSFR, and the detailed analysis of the wall irradiation conditions represent two examples of these applications. Even though the SP_3 approximation of the neutron transport equation constitutes an improvement, as compared to the diffusion equation, it still represents a compromise between diffusion and transport theory, not only in terms of runtimes but also of accuracy. In this context, the development of a multi-group, discrete ordinate (S_N) neutron transport model has been investigated. In this appendix, this activity is briefly described.

A.1 The S_N neutron transport model

For a given neutron energy group ei and a free-flight direction di, the neutron transport equation can be formulated as follows (Lewis and Miller, 1984):

$$\frac{1}{v_{ei}}\frac{\partial \varphi_{ei,di}}{\partial t} + \nabla \cdot \left[(v_{ei}\boldsymbol{\Omega}_{di}) \cdot n_{ei,di}\right] + \Sigma_{t,ei}\varphi_{ei,di} = \\ = S_{f,ei,di} + S_{s,ei,di} + S_{d,ei,di} + Q_{ei,di} \tag{A.1}$$

Both the number of energy groups and of flight directions can be arbitrarily selected by the user. The terms $S_{f,ei,di}$, $S_{s,ei,di}$ and $S_{d,ei,di}$ represent the fission source, the scattering neutrons and the delayed neutron source, respectively, and they are defined as follows:

$$S_{f,ei,di} = \sum_{ej,dj} \varphi_{ej,dj} w_{dj} \left[\nu_{ej}\Sigma_{f,ej}\chi_{p,ej}(1-\beta_{tot})\right] \tag{A.2}$$

$$S_{s,ei,di} = \sum_{ej,dj,l} P_l(\boldsymbol{\Omega}_{di} \cdot \boldsymbol{\Omega}_{dj})(2l+1)\, \Sigma_{sl,ej \to ei} \varphi_{ej,dj} w_{dj} \tag{A.3}$$

$$S_{d,ei,di} = \sum\nolimits_k \lambda_k c_k w_{di} \tag{A.4}$$

where w_{di} is the weight of the direction di. As for the diffusion and the SP_3 models, precursor densities are evaluated with Eq. (2.21).

A source $Q_{ei,di}$ can also be considered for each energy group and direction combination. Its intensity and position can be defined by the user. If the neutron source is placed outside the computational domain, it can be accounted for as a boundary condition.

A.2 Preliminary verification

To verify the new model, 95% enriched uranium cubes of different dimensions are adopted as case studies. The multiplication factor of these cubes is evaluated using both the SP_3 and the S_N models and the results are compared to continuous energy Monte Carlo simulation. An S_6 angular discretization (i.e., 48 free-flight directions) and four energy groups (with cutoff values at 1, 2 and 3 MeV) are adopted, considering anisotropic scattering up to the seventh order. The directions and weights adopted in this work are based on the level symmetric quadrature sets given in (Lewis and Miller, 1984). Four energy groups are also selected for the SP_3 solver. On the other hand, Monte Carlo simulations are carried out using 100 million active neutron histories (10,000 cycles of 10,000 particles, plus 1000 inactive cycles to ensure fission source convergence).

The aim of this verification is to assess the capability of the two neutronics models to correctly predict reactivity in small systems, where neutron leakages are dominant and simpler models such as the SP_3 one may have significant limitations. Results are listed in Tables A.1 and A.2. No comparison is carried out using the diffusion model, as the errors with respect to Monte Carlo are in the other of thousands of pcm, for the considered case studies (Cervi and Cammi, 2019b).

Table A.1. S_N vs. Monte Carlo results.

Cube edge (cm)	k_{eff} S_N	k_{eff} MC	Error (pcm)
16	1.07376	1.07424 ± 0.00009	-48
8	0.58075	0.57992 ± 0.00007	+83
4	0.29227	0.29193 ± 0.00004	+34
2	0.14519	0.14519 ± 0.00003	0
1	0.07222	0.07226 ± 0.00002	-4

Table A.2. SP_3 vs. Monte Carlo results.

Cube edge (cm)	k_{eff} SP_3	k_{eff} MC	Error (pcm)
16	1.06767	1.07424 ± 0.00009	-657
8	0.58567	0.57992 ± 0.00007	+575
4	0.29362	0.29193 ± 0.00004	+169
2	0.14352	0.14519 ± 0.00003	-167
1	0.07004	0.07226 ± 0.00002	-222

A.3 Conclusive remarks

Even using a relatively low number of flight directions, the S_N model performs significantly better than the SP_3 one, always reducing the error with respect to Monte Carlo simulation well below 100 pcm. This improvement can be useful for a more accurate simulation of smaller and less heterogeneous systems, envisaged as possible demonstrators of the MSFR, or to estimate the neutron irradiation conditions at the reactor walls. The higher accuracy of the S_N model comes at the expense of higher computational times. In particular, the four-group S_6 runtimes are about 30 times larger as compared to four-group, SP_3 simulations.

The application of the present model to the MSFR transient analysis may constitute an interesting direction for future research, even though the development of effective acceleration techniques or reduced order methods is required to reduce computational times.

NOMENCLATURE (APPENDIX A)

Latin symbols

c	Precursor density, m^{-3}
n	Neutron density, m^{-3}
P_l	Legendre polynomial (l^{th} order)
Q	Neutron source, m^{-3} s^{-1}
$\dot{q}$	Power source, J s^{-1} m^{-1}
t	Time, s
v_{ei}	Neutron velocity, m s^{-1}
$\boldsymbol{w}$	Arbitrary mesh velocity, m s^{-1}
w_{di}	Flight direction weight (S_N), -

Greek symbols

β	Delayed neutron fraction, -
λ	Precursor decay constant, s^{-1}
$\bar{\nu}$	Average neutrons per fission, -
φ	Neutron flux (SP_3), m^{-2} s^{-1}
Σ	Macroscopic cross section m^{-1}
χ	Neutron yield, -
$\boldsymbol{\Omega}$	Flight direction, -

Subscripts

d	Delayed
ei	Neutron energy group index (S_N)
di	Flight direction index (S_N)
f	Fission
p	Prompt
s	Scattering
sl	Inelastic scattering (l^{th} order)
t	Total

Appendix B

Bubbly flow models

IN Chapter 3, a sensitivity analysis is carried out to compare the main models and correlations available in literature for the evaluation of the bubble diameter and of the interphase momentum and heat transfer. All the correlations selected in this analysis are discussed in the present appendix.

B.1 Bubble diameter models

B.1.1 Isothermal model

According to the isothermal model, the bubble diameter d_b can be evaluated as:

$$d_b = d_0 \left(\frac{p_0}{p}\right)^{1/3} \tag{B.1}$$

where the reference diameter d_0 and pressure p_0 are required as input parameters.

B.1.2 Interface area transport equation

An interface area transport equation (IATE) has been proposed by Ishii et al. (2005) to evaluate the interface area between the liquid and the gaseous phase and its advection through the computational domain:

$$\frac{\partial a_i}{\partial t} + \nabla \cdot (a_i \boldsymbol{u}_l) = \tag{B.2}$$

$$= \frac{2}{3}\frac{a_i}{\alpha_g}\left[\frac{\partial \alpha_g}{\partial t} + \nabla \cdot \left(\alpha_g \boldsymbol{u}_g\right)\right] + \frac{1}{3\psi}\left(\frac{\alpha_g}{a_i}\right)^2 (R_{TI} - R_{RC} - R_{WE})$$

where a_i is the interfacial area per unit volume, while the indices l and g, refer to the liquid and gas phases, respectively (this indexing choice will be maintained though the appendix, even though some of the presented models can also be applied to dispersed solid particles). For a dispersed gaseous phase in a continuous liquid medium, assuming that the bubbles are spherical, $\psi \approx 1/36\pi$ (Ishii and Kim, 2004). The terms R_{TI}, R_{RC} and R_{WE} represent the three main mechanisms that govern the change in a_i:

- Break-up due to the impact of turbulent eddies (*TI*):

$$R_{TI} = C_{TI}\frac{nu_t}{d_b} exp\left(-\frac{We_{cr}}{We}\right)\sqrt{1-\frac{We_{cr}}{We}} \quad where\ We > We_{cr} \tag{B.3}$$

  where $n = \psi a_i^3/\alpha_g^2$, u_t is the turbulent velocity and $d_b = 6\alpha_g/a_i$.

- Coalescence through random collision driven by turbulent eddies (*RC*):

$$R_{RC} = C_{RC}\left[\frac{n^2 u_t d_b^2}{\alpha_{max}^{1/3}\left(\alpha_{max}^{1/3}-\alpha^{1/3}\right)}\right]\left[1 - exp\left(-C\frac{\alpha_{max}^{1/3}\,\alpha^{1/3}}{\alpha_{max}^{1/3}-\alpha^{1/3}}\right)\right] \tag{B.4}$$

- Coalescence due to the acceleration of the following bubble in the wake of the preceding one (*WE*):

$$R_{WE} = C_{WE} C_D^{1/3} n^2 d_b^2 u_r \tag{B.5}$$

where C_D is the drag coefficient (see Section A.2.1) and u_r is the relative velocity.

In this work, it is assumed that $C_{TI} = 0.085$, $We_{cr} = 6.0$, $C_{RC} = 0.004$, $C = 3$, $\alpha_{max} = 0.75$ and $C_{WE} = 0.002$ (Ishii et al, 2005). As already mentioned above, the bubble diameter can be estimated from the phase fraction α_g and from the interface area density a_i as follows:

$$d_b = \frac{6\alpha_g}{a_i} \tag{B.6}$$

B.2 Drag models

The drag force acting on the dispersed bubbles per unit volume can be expressed as the product between a drag function K and the relative velocity between the continuous liquid medium and the dispersed particles, $\boldsymbol{u}_l - \boldsymbol{u}_g$:

$$M_{g,drag} = K(\boldsymbol{u}_l - \boldsymbol{u}_g) \tag{B.7}$$

Different models are available in literature to determine K and $M_{g,drag}$ in turn.

B.2.1 Schiller-Naumann correlation

Assuming a dispersed phase made of spherical bubbles, the drag function K can be expressed as:

$$K = \frac{3}{4} C_d \alpha_g \frac{\rho_g}{d_b} |\boldsymbol{u}_l - \boldsymbol{u}_g| \tag{B.8}$$

According to the Schiller-Naumann correlation (Schiller and Naumann, 1933; Rusche, 2002) the drag coefficient C_d can be evaluated as:

$$C_d = \begin{cases} \dfrac{24(1 + 0.15 Re_b^{0.687})}{Re_b} & for\ Re_b < 1000 \\ 0.44 & for\ Re_b \geq 1000 \end{cases} \tag{B.9}$$

B.2.2 Gidaspow-Schiller-Naumann correlation

According to this model, the drag function can be expressed as (Enwald et al., 1996):

$$K = \frac{3}{4} C_d \alpha_g \frac{\rho_l}{d_b} |\boldsymbol{u}_l - \boldsymbol{u}_g| \alpha_l^{-1.65} \tag{B.10}$$

where the drag coefficient C_d is still evaluated with Eq. (B.9).

B.2.3 Gidaspow-Ergun-Wen-Yu Correlation

Gidaspow (1994) proposed a blend between the Ergun and the Wen and Yu drag correlations (Enwald et al., 1996). According to this model, the Ergun correlation is used if the continuous phase fraction is lower than 0.8:

$$K = \frac{1.75\ \alpha_g \rho_l |\boldsymbol{u}_l - \boldsymbol{u}_g|}{d_b} + \frac{150 \alpha_g^2 \mu_l}{\alpha_l d_b^2} \quad if\ \alpha_g < 0.8 \tag{B.11}$$

while the Wen and Yu correlation is used if the continuous phase fraction is greater than 0.8:

$$K = \frac{3}{4} C_d \alpha_g \frac{\rho_l}{d_b} \left| \boldsymbol{u}_l - \boldsymbol{u}_g \right| \alpha_l^{-1.65} \tag{B.12}$$

where C_d is evaluated with Eq. (B.9).

B.2.4 Ishii-Zuber correlation

Ishii and Zuber (1979) derived the following expression for the drag function:

$$K = \alpha_g C_d \frac{3}{4} \frac{\rho_l}{d_b} \left| \boldsymbol{u}_g - \boldsymbol{u}_l \right| \tag{B.13}$$

where the drag coefficient C_d is defined as:

$$C_d = \frac{24\left(1 + 0.1 Re_b^{0.75}\right)}{Re_b} \tag{B.14}$$

The bubble Reynolds number is here defined as $Re_b = \rho_l \left| \boldsymbol{u}_g - \boldsymbol{u}_l \right| d_b / \mu_{mix}$, where the mixture viscosity is evaluated as follows:

$$\mu_{mix} = \mu_l \left(1 - \frac{\alpha_g}{\alpha_{g,max}} \right)^{-2.5 \alpha_{g,max} (\mu_g + 0.4 \mu_l)/(\mu_g + \mu_l)} \tag{B.15}$$

B.3 Virtual mass models

The virtual mass force acting on the dispersed phase per unit volume can be evaluated as follows:

$$M_{g,virtual\ mass} = C_{vm} \alpha_g \rho_l \left(\frac{D_l \boldsymbol{u}_l}{Dt} - \frac{D_g \boldsymbol{u}_g}{Dt} \right) \tag{B.16}$$

where the virtual mass coefficient C_{vm} needs to be determined from closure relations.

B.3.1 Constant coefficient correlation

For spherical bubbles and for $Re_b > 500 - 1000$ (Kendoush et al., 2007) the virtual mass coefficient C_{vm} approaches a constant value of 0.5. Note that in the MSFR, assuming a bubble diameter of 3 mm, $Re_b \approx 1200$.

B.3.2 Lamb correlation

Lamb (1895) proposed the following correlation to evaluate C_{vm}:

$$C_{vm} = \frac{(1 - E^2)^{0.5} - E\ cos^{-1}E}{E\ cos^{-1}E - E^2(1 - E^2)^{0.5}} \tag{B.17}$$

where E is the bubble aspect ratio (i.e., ratio of the bubble sizes in different directions). The aspect ratio is equal to 1 for a spherical bubble and lower than 1 for an oblate bubble. If E tends to unity, C_{vm} tends to 0.5, reducing to the constant coefficient correlation presented in the previous section. However, models are available to determine the aspect ratio E as a function of the mixture properties. In the sensitivity analysis carried out in Chapter 3, the Wellek model (Wellek et al., 1966) has been selected:

$$E = \frac{1}{1 + 0.163\ Eo^{0.757}} \tag{B.18}$$

$Eo = \frac{g_{eff}|\Delta\rho|d_b^2}{\sigma}$ is the Eötvös number, where the effective acceleration $g_{eff} = \left|\boldsymbol{g} - \frac{D_l \boldsymbol{u}_l}{Dt}\right|$, $\Delta\rho$ is the density difference between the two phases and σ is the surface tension.

B.4 Lift models

The lift force acting on the dispersed phase per unit volume can be evaluated as follows:

$$M_{g,lift} = C_l \alpha_g \rho_l \left(\boldsymbol{u}_l - \boldsymbol{u}_g\right) \times (\nabla \times \boldsymbol{u}_l) \tag{B.19}$$

where the lift coefficient C_l is determined by means of correlations.

B.4.1 Constant coefficient correlation

For spherical bubbles and for $Re_b \gg 1$, a constant lift coefficient of 0.5 can be assumed (VDI-Gesellschaft Verfahrenstechnik und Chemieingenieurwesen, 2010).

B.4.2 Tomiyama correlation

Tomiyama et al. (2002) proposed the following correlation to evaluate C_l:

$$C_l = \begin{cases} min[0.288\ tanh(0.121Re_b), f(Eo_H)] & for\ Eo_H < 4 \\ f(Eo_H) & for\ Eo_H \geq 4\ and\ Eo_H < 10.7 \\ -0.288 & for\ Eo_H \geq 10.7 \end{cases} \quad \text{(B.20)}$$

where:

$$f(Eo_H) = 0.0010422Eo_H^3 - 0.0159Eo_H^2 - 0.0204Eo_H + 0.474 \quad \text{(B.21)}$$

The horizontal Eötvös number is defined as $Eo_H = \frac{g_{eff}|\Delta\rho|d_{b,H}^2}{\sigma}$, where $d_{b,H}$ is the maximum horizontal dimension of the bubble, calculated with a correlation by Wellek et al. (1966):

$$d_{b,H} = d_b(1 + 0.163Eo^{0.757})^{1/3} \quad \text{(B.22)}$$

B.4.3 Legendre-Magnaudet correlation

According to the following correlation due to Legendre and Magnaudet (1998), the lift coefficient can be evaluated as:

$$C_l = \left(C_{l,low}^2 + C_{l,high}^2\right)^{1/2} \quad \text{(B.23)}$$

where:

$$C_{l,low} = \frac{3.68\ Sr}{\pi^2 Re_b^{1/2}(Sr + 0.2Re_b)^{3/2}} \quad \text{(B.24)}$$

with:

$$Sr = \frac{d_b^2}{Re_b \nu_l}[grad(\boldsymbol{u}_l) : grad(\boldsymbol{u}_l)]^{0.5} \quad \text{(B.25)}$$

and:

$$C_{l,high} = \left(\frac{0.5(Re_b + 16)}{Re_b + 29}\right)^{1/2} \quad \text{(B.26)}$$

B.5 Turbulent dispersion models

The turbulent dispersion force acting on the dispersed phase per unit volume can be expressed as the product between a function D and the gradient of the dispersed phase fraction:

$$M_{g,turbulent\ dispersion} = D\ grad(\alpha_g) \tag{B.27}$$

The turbulent dispersion function D can be evaluated with various closure relations. In the sensitivity analysis carried out in Chapter 3, the Burns and the Gosman correlations are considered.

B.5.1 Burns model

According to the Burns model (Burns et al., 2004), the function D can be evaluated as follows:

$$D = \frac{3}{4} C_d Re_b \frac{\nu_l \nu_{t,l} \rho_l \alpha_g}{Sc_t\ d_b^2} \left(\frac{1}{\alpha_g} + \frac{1}{\alpha_l} \right) \tag{B.28}$$

where C_d is the drag coefficient and Sc_t is the turbulent Schmidt number.

B.5.2 Gosman model

According to the Gosman model (Gosman et al., 1992), the function D can be expressed as:

$$D = \frac{3}{4} C_d Re_b \frac{\nu_l \nu_{t,l} \rho_l \alpha_g}{Sc_t\ d_b^2} \tag{B.29}$$

B.6 Interphase heat transfer models

The heat transfer rate per unit volume between the continuous and the dispersed phases can be evaluated as the product between a global exchange coefficient L and the temperature difference ΔT between the phases. In this section, two different models for the evaluation of L, which have are compared in the sensitivity analysis of Chapter 3, are presented.

B.6.1 Ranz-Marshall correlation

Ranz and Marshall (1952) proposed the following correlation to evaluate the heat transfer coefficient:

$$L = \frac{6\alpha_g \kappa_l Nu}{d_b^2} \tag{B.30}$$

where the Nusselt number is estimated as follows:

$$Nu = 2 + 0.6 Re_b^{1/2} Pr^{1/3} \tag{B.31}$$

B.6.2 Analytical correlation for a spherical bubble

This correlation can be derived analytically for a spherical bubble:

$$L = \frac{60\alpha_g \kappa_l}{d_b^2} \tag{B.32}$$

Appendix C

Precursor properties

THE analyses presented in this thesis are carried out assuming the ^{233}U-enriched fuel composition reported in Table C.1. For this fuel composition, eight delayed neutron precursor groups and three decay heat precursor groups are adopted. Their fractions and decay constants are reported in Tables C.2 and C.3 (Aufiero, 2014). Note that for decay heat precursors, fractions represent the portion of the total power density in the form of decay power, for each precursor group.

Table C.1. The fuel composition adopted in this thesis.

Chemical specie	Molar fraction (mol%)
LiF	77.5
ThF_4	20.0
$^{233}UF_4$	2.5

Table C.2. Delayed neutron precursor properties.

Group	Fraction	Decay constant (s^{-1})
1	$22.2 \cdot 10^{-5}$	$1.24667 \cdot 10^{-2}$
2	$48.1 \cdot 10^{-5}$	$2.82917 \cdot 10^{-2}$
3	$40.5 \cdot 10^{-5}$	$4.25244 \cdot 10^{-2}$
4	$64.5 \cdot 10^{-5}$	$1.33042 \cdot 10^{-1}$
5	$102.1 \cdot 10^{-5}$	$2.92467 \cdot 10^{-1}$
6	$17.7 \cdot 10^{-5}$	$6.66488 \cdot 10^{-1}$
7	$22.3 \cdot 10^{-5}$	1.63478
8	$5.1 \cdot 10^{-5}$	3.55460

Table C.3. Decay heat precursor properties.

Group	Fraction	Decay constant (s^{-1})
1	$1.86 \cdot 10^{-2}$	$3.580 \cdot 10^{-4}$
2	$1.29 \cdot 10^{-2}$	$1.680 \cdot 10^{-2}$
3	$1.17 \cdot 10^{-2}$	$1.973 \cdot 10^{-1}$

The Schmidt and the turbulent Schmidt numbers Sc and Sc_t, required in the precursor equations Eqs (2.21) and (2.22), are set to 20 and 0.85, respectively, even if no data are specifically available for the diffusion of species in the MSFR salt (Aufiero et al., 2014b).

List of figures

List of tables

References

Allibert M., Gérardin G., Heuer D., Huffer E., Laureau A., Merle E., Beils S., Cammi A., Carluec B., Delpech S., Gerber A., Girardi E., Krepel J., Lathouwers D., Lecarpentier D., Lorenzi S., Luzzi L., Poumerouly S., Ricotti M.E., Tiberi V., 2016a. D1.1 Description of initial reference design and identification of safety aspects, SAMOFAR Safety Assessment of the Molten Salt Fast Reactor – MSFR.

Allibert, M., Aufiero, M., Brovchenko, M., Delpech, S., Ghetta, V., Heuer, D., Laureau, A., Merle. E., 2016b. 7 – Molten salt fast reactors, Handbook of Generation IV Nuclear Reactors, Woodhead Publishing Series in Energy, Elsevier Ltd., Cambridge MA, USA.

Aufiero, M., 2014. Development of advanced simulation tools for circulating-fuel nuclear reactors, PhD thesis.

Aufiero, M., Brovchenko, M., Cammi, A., Clifford, I., Geoffroy, O., Heuer, D., Laureau, A., Losa, M., Luzzi, L., Merle, E., Ricotti, M.E., 2014a. Calculating the effective delayed neutron fraction in the Molten Salt Fast Reactor: Analytical, deterministic and Monte Carlo approaches, Annals of Nuclear Energy 65, 390-401.

Aufiero, M., Cammi, A., Geoffroy, O., Losa, M., Luzzi, L., Ricotti, M.E., Rouch, H., 2014b. Development of an OpenFOAM model for the Molten Salt Fast Reactor transient analysis, Chemical Engineering Science 111, 78-90.

Aufiero, M., Fiorina, C., Laureau, A., Rubiolo, P., 2015. Serpent-OpenFOAM coupling in transient mode: simulation of a Godiva prompt critical burst, ANS MC2015 Joint International Conference on Mathematics and Computation (M&C), Supercomputing in Nuclear Applications (SNA) and Monte Carlo (MC) Method, Nashville, TN, USA, April 19-23, 2015.

Aufiero, M., Rubiolo, P., Fratoni, M., 2017. Monte Carlo/CFD coupling for accurate modelling of the delayed neutron precursors and compressibility effect in Molten Salt Reactors, Transaction of the American Nuclear Society, vol. 116, San Francisco, California, June 11-15, 2017.

Avramova, M.N., Ivanov, K.N., 1997. Verification, validation and uncertainty quantification in multi-physics modeling for nuclear reactor design and safety analysis, International Journal of Heat and Mass Transfer 40, 4191-4196.

Bannari, R., Bannari, A., Selma, B., Proulx, P., 2011. Mass transfer and shear in an airlift bioreactor: Using a mathematical model to improve reactor design and performance, Chemical Engineering Science 66, 2057-2067.

Baraldi, A., Dodd, M.S., Ferrante, A., 2014. A mass-conserving volume-of-fluid method: Volume tracking and droplet surface-tension in incompressible isotropic turbulence, Computers & Fluids 96, 322-337.

Bauman, H., Cunningham I.G., Lucius, J., Kerr, H., Craven Jr, C., 1971. Rod: A nuclear and fuel-cycle analysis code for circulating-fuel reactors. Technical Report, Oak Ridge National Laboratory, Oak Ridge, TN, USA.

Bell, G.I., Glasstone, S., 1970. Nuclear Reactor Theory, Van Nostrand Reinhold Company, New York.

Bhusare, V.H., Dhiman, M.K., Kalaga, D.V., Roy, S., Joshi, J.B., 2017. CFD simulations of a bubble column with and without internals using OpenFOAM, Chemical Engineering Journal 317, 157-174.

Brandtley, P.S., Larsen, E.W., 2000. The simplified P_3 approximation, Nuclear Science and Engineering 134, 1-21.

Brovchenko, M., Merle, E., Rouch, H., Alcaro, F., Allibert, M., Aufiero, M., Cammi, A., Dulla, S., Feynberg, O., Frima, L., Geoffroy, O., Heuer, D., Ignatiev, V., Kloosterman, J.L., Lathouwers, D., Laureau, A., Luzzi, L., Merk, B., Ravetto, P., Rineiski, A., Rubiolo, P., Rui, L., Szieverth, M., Wang, S., Yamaji, B., 2013. Optimization of the preconceptual design of the MSFR, EVOL Evaluation and Viability of Liquid Fuel Fast Reactor System.

Burns, A.D., Frank, T., Hamill, I., Shi, J.M., 2004. 5th International Conference on Multiphase Flow Vol. 4.

Cammi, A., Di Marcello, V., Guerrieri, C., Luzzi, L., 2011a. Transfer Function Modelling of Zero-Power Dynamics of Circulating Fuel Reactors, Journal of Engineering for Gas Turbines and Power 133, 052916-1 - 052916-8.

Cammi, A., Di Marcello, V., Luzzi, L., Memoli, V., Ricotti, M.E., 2011b. A Multi-Physics Modelling Approach to the Dynamics of Molten Salt Reactors, Annals of Nuclear Energy 38, 1356-1372.

Cammi, A., Fiorina, C., Guerrieri, C., Luzzi, L., 2012. Dimensional Effects in the Modelling of MSR Dynamics: Moving on from Simplified Schemes of Analysis to a Multi-Physics Modelling Approach. Nuclear Engineering and Design 246, 12-26.

Cervi, E., Lorenzi, S., Cammi, A., Luzzi, L., 2017. An Euler-Euler multi-physics solver for the analysis of the helium bubbling system in the MSFR, NENE 2017 26th International Conference Nuclear Energy for New Europe, Bled, Slovenia, September 11-14, 2017.

Cervi, E., Cammi, A., Di Ronco, A., 2018a. Stability analysis of the Generation-IV nuclear reactors by means of the root locus criterion. Progress in Nuclear Energy 106, 316-334.

Cervi, E., Lorenzi, S., Cammi, A., Luzzi, L., 2018b. Analysis of the effect of fuel compressibility on super-prompt-critical dynamics of the Molten Salt Fast Reactor, PHYSOR 2018: Reactor Physics Paving The Way Towards More Efficient Systems, Cancun, Mexico, April 22-26, 2018.

Cervi, E., Lorenzi, S., Luzzi, L., Cammi, A., 2018c. Analysis of the void reactivity effect in the Molten Salt Fast Reactor: impact of the helium bubbling system, PHYTRA4 Fourth International Conference on Physics and Technology of Reactors and Applications, Marrakech, Morocco, September 17-19, 2018.

Cervi, E., Lorenzi, S., Luzzi, L., Cammi, A., 2018d. An OpenFOAM solver for Criticality Safety Assessment in Dynamic Compression Events, Transactions of the American Nuclear Society 119, 855-858.

Cervi, E., Lorenzi, S., Cammi, A., Luzzi, L., 2019a. Development of a multiphysics model for the study of fuel compressibility effects in the Molten Salt Fast Reactor, Chemical Engineering Science 193, 379-393.

Cervi, E., Lorenzi, S., Cammi, A., Luzzi, L., 2019b. Development of an SP_3 neutron transport solver for the analysis of the Molten Salt Fast Reactor, Nuclear Engineering and Design 346, 209-219.

Cervi, E., Lorenzi, S., Luzzi, L., Cammi, A., 2019c. Multiphysics analysis of the MSFR helium bubbling system: a comparison between neutron diffusion, SP3 neutron transport and Monte Carlo approaches, Annals of Nuclear Energy 132, 227-235.

Cervi, E., Cammi, A., 2019a. An Arbitrary Lagrangian Eulerian solver for shock imploding fissile materials, Transactions of the American Nuclear Society 121, 763-766.

Cervi, E., Cammi, A., 2019b. A coupled neutronics shock physics solver: implementation of an SN neutron transport module, Transactions of the American Nuclear Society 121, 767-770.

Cervi, E., Cammi, A., 2020. An Arbitrary Lagrangian-Eulerian, coupled neutronics-shock physics model for the analysis of shockwave implosion of solid fissile materials, Annals of Nuclear Energy 141, Article 107322.

Davison, L., 2008. Fundamentals of Shock Wave Propagation in Solids, Springer-Verlag, Berlin Heidelberg.

Delpech, S., Merle-Lucotte, E., Heuer, D., Allibert, M., Ghetta, V., Le-Brun, C., Mathieu, L., Picard, G., 2009. Reactor physics and reprocessing scheme for innovative molten salt reactor system. Journal of Fluorine Chemistry 130, 11-17.

Demol, R., Vidal, D., Shu, S., Bertrand, F., Chaouki, J., 2019. Mass transfer in the homogeneous flow regime of a bubble column, Chemical Engineering and Processing – Process Intensification 144, Article 107647.

Dolan T.J. (Ed.), 2017. Molten Salt Reactors and Thorium Energy, Woodhead Publishing Series in Energy, Elsevier Ltd., Cambridge MA, USA.

Duerigen, S., 2013. Neutron transport in hexagonal reactor cores modelled by trigonal-geometry diffusion and simplified P_3 nodal methods, HZDR technical report.

Enwald, H., Peirano, E., Almstedt, A.E., 1996. Eulerian Two-Phase Flow Theory Applied to Fluidization, International Journal of Multiphase Flow 22, 21-66.

Faghri, A., Zhang, Y., 2006. Transport phenomena in Multiphase Systems, Elsevier, Amsterdam, Boston, Heidelberg, London, New York, Oxford, Paris, San Diego, San Francisco, Singapore, Sydney, Tokyo.

Fiorina, C., 2013. The molten salt fast reactor as a fast spectrum candidate for thorium implementation, PhD thesis.

Fiorina, C., Aufiero, M., Cammi, A., Franceschini, F., Krepel, J., Luzzi, L., Mikityuk, K., Ricotti, M.E., 2013. Investigation of the MSFR core physics and fuel cycle characteristics, Progress in Nuclear Energy 68, 153-158.

Fiorina, C., Lathouwers, D., Aufiero, M., Cammi, A., Guerrieri, C., Kloosterman, J.L., Luzzi, L., Ricotti, M.E., 2014. Modelling and analysis of the MSFR transient behaviour, Annals of Nuclear Energy 64, 485-498.

Fiorina, C., Hursin, M., Pautz, A., 2017. Extension of the GeN-Foam neutronic solver to SP_3 analysis and application to the CROCUS experimental reactor, Annals of Nuclear Energy 101, 419-428.

Gelbard, E.M., 1962. Applications in the simplified spherical harmonics equations in spherical geometry, Technical Report WAPD-TM-294, Bettis Atomic Power Laboratory, West Mifflin, PA, USA.

Gerardin, D., Allibert, M., Heuer, D., Laureau, A., Merle-Lucotte, E., Seuvre, C., 2017. Design evolutions of Molten Salt Fast Reactor, International conference on Fast Reactors and Related Fuel Cycles: Next Generation Nuclear Systems for Sustainable Development (FR17), Yekaterinburg, Russia, June 26-29, 2017.

Gidaspow, D., 1994. Multiphase flow and fluidization, Academic Press, New York.

GIF, 2017. Annual Report 2017, Available from: https://www.gen-4.org/gif/jcms/c_102083/gif-annual-report-2017-210918.

Gosavi, S., Kulkarni, N., Mathpati, C.S., Mandal, D., 2018. CFD modeling to determine the minimum fluidization velocity of particles in gas-solid fluidized bed at different temperatures, Powder Technology 327, 109-119.

Gosman, A.D., Lekakou, C., Politis, S., Issa, R.I., Looney, M.K., 1992. Multidimensional modelling of turbulent two-phase flows in stirred vessels, AIChE Journal 38, 1946-1956.

Gropp, W., Lusk, E., Skjellum, A., 2014. Using MPI Portable Parallel Programming with the Message-Passing Interface, third edition, The MIT Press, Cambridge, MA, USA, London, UK.

Guerrieri, C., Aufiero, M., Cammi, A., Fiorina, C., Luzzi, L., 2012. A preliminary study of the MSFR dynamics, Proceedings of the 2012 20th International Conference on Nuclear Engineering collocated with the ASME 2012 Power Conference ICONE20-POWER2012, Anaheim CA, USA, July 30 – August 3, 2012.

Helmi, A., Voncken, R.J.W., Raijmakers, A.J., Roghair, I., Gallucci, F., van Sint Annaland, M., 2018. On concentration polarization in fluidized bed membrane reactors, Chemical Engineering Journal 332, 464-478.

Ignatiev, V.V., Feynberg, O., Merzlyakov, A., Toropov, A., 2012. Progress in development of MOSART concept with Th support, Proceedings of ICAPP ’12, Chicago, USA, June 24-28, 2012.

Ishii, M., Zuber, N., 1979. Drag coefficient and relative velocity in bubbly, droplet and particulate flows, AIChE Journal 5, 843-855.

Ishii, M., Kim, S., 2004. Development of One-Group and Two-Group Interfacial Area Transport Equation, Nuclear Science and Engineering 146, 257-273.

Ishii, M., Kim, S., Kelly, J., 2005. Development of Interfacial Area Transport Equation 37.

Jasak, H., Jemcov, A., Tukovic, Z., 2007. OpenFOAM : a C++ library for complex physics simulations, International Workshop on Coupled Methods in Numerical Dynamics, IUC, Dubrovnik, Croatia, September 19-21, 2007.

Kendoush, A.A., Sulaymon, A.H., Mohammed, S.A.M., 2007. Experimental evaluation of the virtual mass of two solid spheres accelerating in fluids, Experimental Thermal and Fluid Science 31, 813-823.

Kia, S.A., Aminian, J., 2017. Hydrodynamic modeling strategy for dense to dilute gas-solid fluidized beds, Particuology 31, 105-116.

Kopsch, T., Murnane, D., Symons, D., 2018. Computational modelling and experimental validation of drug entrainment in a dry powder inhaler, International Journal of Pharmaceutics 553, 37-46.

Krepel, J., Rohde, U., Grundmann, U., Weiss, F.-P., 2007. DYN3D-MSR spatial dynamics code for molten salt reactors, Annals of Nuclear Energy 34, 449-462.

Lahey, R.T., 2005. The simulation of multidimensional multiphase flows, Nuclear Engineering and Design 235, 1043-1060.

Lamarsh, J.R., 2002. Introduction to nuclear reactor theory, American Nuclear Society, LaGrange Park IL, USA.

Lamb, H., 1895. Hydrodynamics, Cambridge University Press, Cambridge.

Lance, M., Marié, J.L., Moursali, E., Bataille, J., Suzanne, C., Roig, V., Bel'Fdhila, R., Masbernat, L., 1996. Experimental study of turbulent bubbly shear flows, Chemical Engineering Communications 141, 51-70.

Lathouwers, D., 1999. Modelling and simulation of turbulent bubbly flow, PhD thesis.

Laureau, A., 2015. Développement de modèles neutroniques pour le couplage thermohydraulique du MSFR et le calcul de paramètres cinétiques effectifs, PhD thesis.

Legendre, D., Magnaudet, J., 1998. The lift force on a spherical bubble in a viscous linear shear flow, Journal of Fluid Mechanics 368, 81-126.

Leppänen, J., Pusa, M., Viitanen, T., Valtavirta, V., Kaltiaisenaho, T., 2015. The Serpent Monte Carlo code: Status, development and application in 2013, Annals of Nuclear Energy 82, 142-150.

Lewis, E.E., Miller, W.F., 1984. Computational methods of neutron transport, John Wiley & Sons, New York/Chichester/Brisbane/Toronto/Singapore.

Lorenzi S., Cammi A., Luzzi L., Pini A., Allibert M., Gérardin D., Heuer D., Laureau A., Merle E., Lathouwers D., Kloosterman J.L., 2016. TEC1.1 Plant database for the system and safety analysis of the MSFR, SAMOFAR Safety Assessment of the Molten Salt Fast Reactor – MSFR.

Luzzi, L., Di Marcello, V., Cammi, A., 2012. Multi-Physics Approach to the Modeling and Analysis of Molten Salt Reactors, Physics Research and Technology Series, pp. 1-140, Nova Science Publisher, Inc., New York NY, USA.

MacPherson, H., 1985. The molten salt reactor adventure, Nuclear Science and Engineering 90, 374-380.

Mahadevan, V.S., Ragusa, J.C., Mousseau, V.A., 2012. A verification exercise in multiphysics simulations for coupled reactor physics calculations, Progress in Nuclear Energy 55, 12-32.

Marti, J., Haselbacher, A., Steinfeld, A., 2015. A numerical investigation of gas-particle suspensions as heat transfer media for high-temperature concentrated solar power, International Journal of Heat and Mass Transfer 90, 1056-1070.

McHyman, J., 1984. Numerical methods for tracking interfaces, Physica D 12, 396-407.

Moukalled, F., Mangani, L., Darwish, M., 2016. The Finite Volume Method in Computational Fluid Dynamics, Springer, New York.

Nykteri, G., Koukouvinis, P., Gonzales Avila, S.R., Ohl, C.-D., Gavaises, M., 2020. A Σ-γ two-fluid model with dynamic local topology detection: Application to high-speed droplet impact, Journal of Computational Physics 408, Article 109225.

OpenFOAM, 2013. OpenFOAM Documentation, available at http://www.openfoam.org/docs/.

Panda, S.K., Singh, K.K., Shenoy, K.T., Buwa, V.V., 2017. Numerical simulation of a liquid-liquid flow in a continuous gravity settler using OpenFOAM and experimental verification, Chemical Engineering Journal 310, 120-133.

Passalacqua, A., Fox, R.O., 2011. Implementation of an iterative solution procesure for multi-fluid gas-particle flow models on unstructured grids, Powder Technology 213, 174-187.

Patankar, S.V., 1980. Numerical heat transfer and fluid flow, Hemisphere, New York.

Pioro, I.L. (Ed.), 2016. Handbook of Generation IV Nuclear Reactors, Woodhead Publishing Series in Energy, Elsevier Ltd., Cambridge MA, USA.

Pope, S.B., 2000. Turbulent Flows, Cambridge University Press, Cambridge.

Qiu, S., Zhang, D., Liu, L., Liu, M., Xu, R., Gong, C., Su, G.H., 2016. Coupled neutronics/thermal-hydraulics and safety characteristics of liquid-fueled Molten Salt Reactors, Kerntechnik 81, 149-159.

Ragusa, J.C., Mahadevan, V.S., 2009. Consistent and accurate schemes for coupled neutronics thermal-hydraulics reactor analysis, Nuclear Engineering and Design 239, 566-579.

Ranz, W.E., Marshall, W.R., 1952. Evaporation from droplets, Chemical Engineering Progress 48, 173-180.

Reinhardt, Y., Meinen, N., Meyer, D.W., 2013. Modeling anisotropic Reynolds-stress dissipation in particle- or droplet-laden flows, International Journal of Multiphase Flow, 1-3.

Rusche, H., 2002. Computational Fluid Dynamics of Dispersed Two-Phase Flows at High Phase Fractions, PhD thesis.

Santamarina, A., Bernard, D., Blaise, P., Coste, M., Courcelle, A., Huynh, T.D., Jouanne, C., Leconte, P., Litaize, O., Ruggiéri, J-M., Sérot, O., Tommasi, J., Vaglio, C., Vidal, J-F., 2009. The JEFF-3.1.1 Nuclear Data Library, JEFF Report 22, OECD/NEA.

Serp, J., Allibert, M., Beneš, O., Delpech, S., Feynberg, O., Ghetta, V., Heuer, D., Holcomb, D., Ignatiev, V., Kloosterman, J.L., Luzzi, L., Merle, E., Uhlíř, J., Yoshioka, R., Zhimin, D., 2014. The molten salt reactor (MSR) in generation IV: Overview and perspectives, Prog. Nucl. Energy 77, 308-319.

Schiller, L., Naumann, A., 1933. Über die grundlegenden Berechnungen bei der Schwerkraftaufbereitung, Zeitschrift des Vereins Deutscher Ingenieure 77, 318-310 (in German).

Stacey, W. M., 2009. Nuclear Reactor Physics, Wiley-VCH, Weinheim.

Tano, M., Rubiolo, P., Doche, O., 2017. Progress in modelling solidification in molten salt coolants, Modelling and simulation in Material Science and Engineering 25, 1-29.

Tomiyama, A., Tamai, H., Zun, I., Hosokawa, S., 2002. Transverse migration of single bubbles in simple shear flows, Chemical Engineering Science 57, 1849-1858.

Thompson, P.A., 1972. Compressible-fluid dynamics, McGraw-Hill, New York.

Tripathi, R.G., Buwa, V.V., 2015. Numerical Simulation of Gas-Liquid Boiling Flows Using OpenFOAM, Procedia IUTAM 15, 178-185.

Tuominen, R., Valtavirta, V., Peltola, J., Leppänen, J., 2016. Coupling Serpent and OpenFOAM for Neutronics – CFD Multi-physics Calculations, PHYSOR 2016: Unifying Theory and Experiments in the 21st Century, Sun Valley, Idaho, May 1-5, 2016.

VDI-Gesellschaft Verfahrenstechnik und Chemieingenieurwesen (Ed.), 2010. VDI Heat Atlas, Springer-Verlag Berlin Heidelberg.

Wellek, R.M., Agrawal, A.K., Skelland, A.H.P., 1966. Shape of liquid drops moving in liquid media, AIChE Journal 12, 854-862.

Weller, H.G., Tabor, G., Jasak, H., Fureby, C., 1998. A tensorial approach to computational continuum mechanics using object-oriented techniques, Computational Physics 12, 620-631.

Wilcox, D.C., 1998. Turbulencce modeling for CFD, DCW Industries, La Canada, CA, USA.

Zhang, D., Liu, L., Liu, M., Xu, R., Gong, C., Zhang, J., Wang, C., Qiu, S., Su, G.H., 2018. Review of conceptual design and fundamental research of molten salt reactors in China, International Journal of Energy Research 42, 1834-1848.